Fluid-particle interactions in channel flows

Qingsong Liu

[redacted]

A dissertation submitted in partial fulfillment
of the requirements for the degree of
Doctor of Philosophy
of
University College London.

Department of Mathematics
University College London

January 21, 2025

I, Qingsong Liu, confirm that the work presented in this thesis is my own. Where information has been derived from other sources, I confirm that this has been indicated in the thesis.

Abstract

This thesis describes a research study on mathematical modelling of solid particle trajectories in a fluid-filled channel. Inspired by the idea that ice crystal particles can clog sensors on aircraft wings, the original motivation for the research is to avoid collisions between particles and channel walls. Therefore most of the two-dimensional solution testing stops at the moment when the particle collides with the channel wall. The thesis, which combines numerical and analytical work, begins with investigations of the trajectory of a single particle in a fixed shape channel within which the oncoming inviscid fluid flow is uniform; here we find sustained oscillations provide a possible way to keep the particle moving in the channel without collision. Then we move on to the motion trajectories of a particle in an expanding or contracting channel subject to various different channel shapes. In the subsequent chapter we create a multi-particle motion model. Besides the fixed shape model or the regular shape model, the motion trajectories of a particle in a flexible-walled channel whose deformation is caused by the pressure effects are also considered in this thesis. In the final two chapters, the motion trajectories of a particle in a fluid within flow at low Reynolds number are addressed, followed by the overall conclusion.

Impact Statement

The research described in this thesis has been inspired by Professor Frank Smith, who has done abundant research on biomedical and industrial applications. In turn, his interest was motivated by contacts with a consultancy company Aerotex which specialises in icing in aerodynamic settings. In a conversation with Frank, and from a subsequent literature search, I learned that when an airplane passes through clouds, the pilot often needs to rely on sensors on the airplane wings to determine the parameters of the airplane during flight and then adjust the operation. Sometimes, however, ice crystals in the clouds clog the sensors, causing pilots to make wrong judgments, and then make wrong operations, affecting the safety of everyone on board. After reading a series of related literature, I also learned that an important part of the sensor is a long and thin pipe, which is a very important and fragile device. The application to icing within engines is also significant. The crash of Air France Flight 447 in 2009, which killed all 228 people on board, drew particular attention to a type of ice known as ice crystal icing. Therefore, avoiding collision between a solid particle and the walls of the containing vessel is potentially very important research. Many researchers have made a more comprehensive analysis of the two-dimensional or three-dimensional motion trajectory of a single or multiple particle(s) moving in a vessel or tube or interacting with each other. Most studies have focused on round or spherical particles. Since ice crystals are mostly in long, thin shapes as they pass through tubes, relatively thin elliptical particles may better simulate the process. We examine the aspect of particle shape in detail in the present thesis.

A flexible model for walls is also addressed in the thesis. This model could be used in bio-medicine. For example, sometimes under the influence of disease, some blood cells will coagulate into a solid, such as a thrombus, and most of the time the thrombus moving through the blood is dominated by the shape we assume (the length of the solid is much larger than the width of the blood vessel). Background literature is summarised in the present study, together with new modelling.

In addition, a low Reynolds number model is also mentioned at the end of the study. The model can be applied to solve many practical problems. When domestic sewage is discharged into a sewer pipe, due to the influence of factors such as grease in kitchen waste, the liquid at this time can be treated as a liquid flowing at low Reynolds number. Over time, particles suspended in the liquid can become deposited inside the pipe, causing it to become clogged. The trajectory of the deposition process can be simulated by this model.

Acknowledgements

I would first like to thank my supervisor Professor Frank Smith. The email to him was always open for discussions whenever I ran into a trouble spot or had a question about my research or writing; this was particularly important during the pandemic times which affected my first two years of research. He consistently urged me on in my work and steered me in the right direction whenever he thought I needed it. I would also like to thank the experts who provided all the researches in this field. I believe that all these researches may become intellectual treasures for mankind. I am also very grateful to UCL for providing a positive environment for my academic life. Finally, I must express my very profound gratitude to my parents and to my friends for providing me with unfailing support and continuous encouragement throughout my years of study and through the process of researching and writing this thesis. This accomplishment would not have been possible without them. Thank you.

UCL Research Paper Declaration Form: referencing the doctoral candidate's own published work(s)

1. **1. For a research manuscript that has already been published** (if not yet published, please skip to section 2)**:**

    (a) **What is the title of the manuscript?**

    On interaction between freely moving bodies and fluid in a channel flow

    (b) **Please include a link to or doi for the work:**

    https://doi.org/10.1016/j.taml.2022.100413

    (c) **Where was the work published?**

    Theoretical and Applied Mechanics Letters

    (d) **Who published the work?**

    Elsevier

    (e) **When was the work published?**

    17 November 2022

    (f) **List the manuscript's authors in the order they appear on the publication:**

    Qingsong Liu, Samire Yazar, Frank Smith

    (g) **Was the work peer reviewd?**

    Yes

    (h) **Have you retained the copyright?**

    No

    (i) **Was an earlier form of the manuscript uploaded to a preprint server (e.g. medRxiv)? If 'Yes', please give a link or doi**

    No

    If 'No', please seek permission from the relevant publisher and check the box next to the below statement:

    ☒ *I acknowledge permission of the publisher named under 1d to include in this thesis portions of the publication named as included* *in 1c.*

2. **For a research manuscript prepared for publication but that has not yet been published** (if already published, please skip to section 3)**:**

   (a) **What is the current title of the manuscript?**

   (b) **Has the manuscript been uploaded to a preprint server 'e.g. medRxiv'?**
   If 'Yes', please please give a link or doi:

   (c) **Where is the work intended to be published?**

   (d) **List the manuscript's authors in the intended authorship order:**

   (e) **Stage of publication:**

3. **For multi-authored work, please give a statement of contribution covering all authors** (if single-author, please skip to section 4)**:**

   QingSong Liu:Formal analysis, software, investigation, validation, writing, editing, admin

   Samire Yazar:Investigation, validation, writing, editing, admin

   Frank Smith:Supervision, formal analysis, investigation, project administration, writing, editing

4. **In which chapter(s) of your thesis can this material be found?**

   Chapter 4

e-Signatures confirming that the information above is accurate (this form should be co-signed by the supervisor/ senior author unless this is not appropriate, e.g. if the paper was a single-author work)**:**

Candidate:
Qingsong Liu
Date:
18/12/2024

Supervisor/Senior Author signature (where appropriate)**:**

Frank Smith; Samire Yazar

Date:19/12/2024

1. For a research manuscript that has already been published (if not yet published, please skip to section 2)**:**

1. **What is the title of the manuscript?**

   Fluid flow past a freely moving body in a straight or distorted channel

2. **Please include a link to or doi for the work:**

   https://doi.org/10.1007/s00162-023-00684-9

3. **Where was the work published?**

   Theoretical and Computational Fluid Dynamics

4. **Who published the work?**

   Springer Nature

5. **When was the work published?**

   25 January 2024

6. **List the manuscript's authors in the order they appear on the publication:**

   Samire Yazar, Qingsong Liu, Frank T. Smith

7. **Was the work peer reviewd?**

   Yes

8. **Have you retained the copyright?**

   No

9. **Was an earlier form of the manuscript uploaded to a preprint server (e.g. medRxiv)? If 'Yes', please give a link or doi**

   No
   If 'No', please seek permission from the relevant publisher and check the box next to the below statement:

   ☒ *I acknowledge permission of the publisher named under 1d to include in this thesis portions of the publication named as included in 1c.*

For a research manuscript prepared for publication but that has not yet been published (if already published, please skip to section 3)**:**

1. **What is the current title of the manuscript?**
2. **Has the manuscript been uploaded to a preprint server ’e.g. medRxiv’? If ’Yes’, please please give a link or doi:**
3. **Where is the work intended to be published?**
4. **List the manuscript’s authors in the intended authorship order:**
5. **Stage of publication:**

For multi-authored work, please give a statement of contribution covering all authors (if single-author, please skip to section 4)**:**

Samire Yazar:Formal analysis, software, investigation, validation, writing, editing, admin

QingSong Liu:Formal analysis, software, investigation, validation, writing, editing, admin

Frank Smith:Supervision, formal analysis, investigation, project administration, writing, editing

In which chapter(s) of your thesis can this material be found?

Chapter 2

e-Signatures confirming that the information above is accurate (this form should be co-signed by the supervisor/ senior author unless this is not appropriate, e.g. if the paper was a single-author work)**:**

Candidate:

Qingsong Liu

Date:

18/12/2024

Supervisor/Senior Author signature (where appropriate)**:**

Frank Smith; Samire Yazar

Date:19/12/2024

Contents

List of Figures

Chapter 1

Introductory Material

The motivation for the topics addressed in this mathematical modeling thesis on fluid-body interaction is that the models developed and studied in the research might be applied to solve real-world problems of interest. One such problem, or area of problems, concerns the issue of the safety of aircraft in flight, including especially ice formation on the wings or fuselage of an aircraft, or collisions caused by supercooled water or ice crystals entering the engine [1, 2, 3]. Many researchers have made great academic contributions to the study of ice accumulation process [4]. At the same time, many researchers have provided many interesting models for simulation of droplet(s) collisions. Among these models, many researchers have given liquid-air-solid models or liquid-air-liquid models, and have precisely studied the effects of gases on liquid and solid surfaces at the moment before collision [5, 6, 7].

Essentially, the same modeling approach can be used for cars (For instance, if we have a car with a length of $L = 4m$, a velocity of $v = 30m/s$, air density $\rho = 1.225kg/m^3$, dynamic viscosity of air $\mu = 1.81 * 10^{-5} Pa \cdot s$, and gravity $g = 9.81m/s^2$, we can calculate the approximate $Re = 8.1 * 10^6$ and $Fr = 4.78$), ships(For instance, if we have a waterline length of $L = 5m$, a ship velocity of $v = 15m/s$, water density $\rho = 1000kg/m^3$, dynamic viscosity of water $\mu = 1 * 10^{-3} Pa \cdot s$, and gravity $g = 9.81m/s^2$, we can calculate the approximate $Re = 7.5 * 10^7$ and $Fr = 2.14$), or submarines(For instance, if we have a waterline length of $L = 10m$, a ship velocity of $v = 15m/s$, water density $\rho = 1000kg/m^3$, dynamic viscosity of water $\mu = 1 * 10^{-3} Pa \cdot s$, gravity $g = 9.81m/s^2$, We can calculate the approximate $Re = 1.5 * 10^8$ and $Fr = 1.51$). At the same time, these models can also be applied to biomedical fields, such as in the movement of thrombi in blood vessels and the movement of drugs in the esophagus [8, 9, 10]. The range of interest is widened by the field of food classification which can also produce more extensive applications, for example in order to systematically study defects involved in rice particles moving along chutes [11].

There has been much work on the flow of fluid past a fixed body (particle, object) stationed within a vessel (tube, pipe, channel) or in free space. In the latter setting, this is often with the oncoming flow being a uniform stream; in the internal flow setting the oncoming flow may be a uniform stream or a flow with non-zero vorticity, depending on the precise context. The flow past such a rigid body poses a classical problem, which has been addressed by means of modeling, analysis, computation, and experiments [12, 13, 14]. The modeling is usually based on the Navier-Stokes equations of fluid flow or on a system suitably reduced from those equations, such as the Euler equations and the boundary layer equations for relatively high flow rates and the Stokes equations and lubrication equations for relatively low flow rates. The lift and drag exerted on the body by the fluid motion are often of much interest [15, 16]. There is still a vast amount to be discovered in regard to a freely moving body or system of bodies where the surrounding fluid flow and the movements of the body interact in a two-way fashion. Here the body position affects the flow as in the classical setting above but also the fluid flow provokes pressure and other flow forces (the lift and drag mentioned above) which move the body around by virtue of Newton's rigid-body effects, thus feeding back on the fluid flow, and so on.

In many recent articles using mathematical modeling, scholars have studied the interaction between free rigid bodies and the surrounding fluid flow and reached interesting conclusions, for example on particle trajectories and collisions [11, 17, 18, 19, 20, 21, 22, 23, 24, 25, 26, 27, 28, 29, 30, 31, 32, 33, 34, 35, 36]. These articles involve studies of interactions between particles and fluids in various contexts. For channel flows and boundary layers in particular, the body or particle is often imagined to be a thin, straight plate in two spatial dimensions, with or without significant vorticity in the approaching fluid flow. The majority of the researches mentioned earlier consider totally unsteady motion of the body as well as the fluid, which is consistent with a situation where there is not an excessively high-density ratio between the body and the fluid. In this thesis, however, our main focus will be on the problem of how a reasonably dense particle, say with an elliptical body shape, moves in a tube, i.e. in a pipe or channel. Our focus will be on the case of a channel. The fact that the density ratio between ice and air is quite large, between 900 and 1000, is important here and will be investigated in more depth below. Many other dynamic fluid-body or fluid-particle interactions have been researched in the last few years [33, 34, 35]. The consequences of a collision between two solid bodies or between one solid body and an enclosing wall have been examined in papers [5, 11, 17, 19, 23, 5]. Moreover, although some researchers have examined how different particles remain in a calcination zone [37], which is a gas counterflow, others have concentrated on how a particle moves in a Newtonian fluid [36]. These investigations have all focused on the movement of particles inside a fluid flow.

We plan to account in a rational manner for the motion of individual particle in a channel, in our study. Initially we assume that this is a two-dimensional flow, with an elliptically shaped particle moving between parallel walls. We also assume in the majority of the current work that the fluid surrounding the particle, such as air or fluid depending on the specific context, is in quasi-steady flow and can be treated as an inviscid, incompressible, Newtonian fluid with uniform density. For clarification, in chapter 2-5, we assume the whole process occurs in quasi-steady, inviscid flow. In chapter 6, we assume the whole process occurs in quasi-steady but viscous flow, which means we consider the influence of viscosity. Thus, in our study, the core equations present quasi-steady fluid flow, but accompanied by unsteady object motion. This setting of quasi-steady fluid flow corresponds to the density of the object (for example, ice particles) being substantially greater than the density of the fluid (for example, air), see[20]. This setting works very well in principle for ice particles surrounded by air. We assume that the oncoming flow in the channel is a steady uniform flow (although the addition of uniform shear flow is also mentioned in some configurations) and that our particles move freely in the flow. In our study, which for the most part supposes the flow rate to be large (and hence the Reynolds number is large), the target particle is actually small enough to ignore any gravitational effect; further details can be found in appendix B. Based on the previous hypothesis, we can build below on the information and understanding that other researchers have found [11, 17, 18, 19, 20, 21]. In addition, this work contains increased variations: in recent studies, articles mainly take the channel width to be fixed in their model (e.g. [38]). Based on these, we make further adjustments, such as widening or narrowing the channel, or setting part of the channel to be flexible. Such a type of model may be used in simulating the process of a stone (as a particle) passing from the renal tubule (a narrower tube) to the urethra (a wider tube), see [39].

Besides the above points, most of the recent papers are focusing on a single particle motion in the channel. Thus in this thesis, we also develop analytically a model for two particles. Moreover, and in contrast with most of the studies performed in the present thesis, the low Reynolds number flow for a single particle motion within a channel still represents a gap in the subject [40, 41]; so we aim to fill that gap as well. In addition, many researchers have performed valuable studies on solid-solid collision or liquid-solid collision, e.g. [5]. In the current work the behavior of a particle approaching a collision point is also an interesting topic. Finally here, the rebound of a single particle after such a collision represents a further study conducted in this thesis.

In the following description, in chapter 2, we start with a very basic model of single particle movement in a fixed channel shape. Then we deduce the governing equations or boundary conditions for the model. With the conditions and equations established, we create our mathematical model and test different parameters' influence on our model results, and then draw conclusions. A very interesting part to emphasize here is that for the first time we find that when the center of mass location is at less than 1/3 of the distance between the leading and trailing edge of the particle there will be an oscillation happening to our particle. This could be a useful way to keep the particle moving between the channel walls for a long time without collision.

In chapter 3 more particle motion models are given. The numerical and analytical methodology introduced in the early chapters of the thesis is used throughout most of the subsequent chapters, and the accuracy of the approach is tested by examination of the effects of grid refinement. As well as the single particle motion, the multi-particles problem is also an interesting matter. Thus, in chapter 4, we create a two-particles model and study certain properties of this model, including collisions.

In chapter 5, inspired by chapter 3, we research how a channel which is partly flexible influences our particle motion. During the model building in chapter 5, the flexibility of the channel is governed by a fourth-order differential equation [42, 43, 44, 45, 46, 47, 48, 49, 50].

All of the above models assume motion at high Reynolds numbers. Thus in Chapter 6, we set the precondition at low Reynolds numbers and give a detailed study of the particle motion and its interaction with lubricating flow. Many researches have been done on the motion of droplets or bubbles at low Reynolds numbers [51, 52, 53]. At the same time, particle transport in low Reynolds number fluids has a wide range of applications in science and engineering. The behaviour and features of particle suspensions may be used in chemical and mining engineering to determine how paint-related substances flow and how minerals are separated[54]. The biological functions and human health of cells and microstructures in bodily fluids are tightly linked in biological transport [55, 56]. Based on the fact that this topic may have very common universal applications in real life, we are going to present our research on this topic in this thesis.

In Appendix A we study a very simple single particle bouncing model, i.e. the rebound of the particle after a collision is discussed.

Chapter 7 presents the conclusions for the thesis.

Chapter 2

Fluid flow past a freely moving body in a straight or distorted channel

This chapter is based on the paper ”Fluid flow past a freely moving body in a straight or distorted channel” written by Samire Yazar, the present author and Frank T Smith, in the journal ”Theoretical and Computational Fluid Dynamics”(2023). We present the paper as it is, in full. The majority of the paper is from contributions by the present author, the main exception being the subsection on wake effects.

This work addresses the interactive effects associated with a thin body that is free to move in the flow of the surrounding fluid within a channel. The background for the present work mainly concerns industrial and biomedical applications such as in problems on firing of bullet-like bodies in a defense context and the entry of objects into engine intakes in an aerodynamic safety context [1, 3, 57], the travel of solids within vessels of major networks in the human body, the transport of blood clots, embolization procedures in stroke treatment in a biomedical context [10, 9, 8]. Another possible practical use of the current research is in development of a body-transport approach to trace any weaknesses in an arterial wall or other containing wall. The internal transient movement of the body through an artery makes a weak part of an artery wall change shape (due to the weak part being more elastic) and hence show up in a clinical scan. Practical interests also exist in industry, biomedical, environmental and engineering problems with constrictions and branchings especially in respect to the medical aspect in terms of flow blockage and disease initiation. An example is in predicting where a thrombus becomes stuck in an artery, or where a loose shard entering an aircraft engine intake eventually hits the engine walls and can cause damage there.

A number of studies have addressed fluid-body interaction by means of direct simulations and, in a few cases, experiments [58, 59, 60, 61, 62, 63, 64, 65, 66]. Our concern is more on the analytical side. The present study of the body- and fluid-flow inside a channel is based on [11, 17]. The body considered here is relatively thin and free to move along a channel in which fluid is travelling. The channel has an indentation (constriction or dilation) which is either of prescribed shape or is due to wall flexibility. In [11] interactions between a finite number of infinitesimally thin moving bodies or grains and the surrounding fluid within a straight-walled channel are analysed in detail together with the instability about the uniform state. The grains there are straight and free to move in a nearly parallel configuration in quasi-inviscid fluid, the combined motion being assumed to be planar. [17] considers a single body having thickness or camber (or both) interacting with the flow in a straight-walled channel. Another aspect of theoretical investigation on collisions, bouncing and skimming, e.g. shallow-water skipping in fluid-body or fluid-fluid impacts, is given in [27, 18, 67]. Moreover, most of the research in this area has been for two spatial dimensions (x, y, say) and time (t) but a recent work [68] has included three spatial dimensions (thus x, y, z as well as time t). The current contribution has almost the same interaction structure as in [17] with the new piece here being on the unsteady interactions between a body and the fluid flow past it, inside an indented (constricted or dilated) channel. The indentation is either a given shape or an unknown shape due to flexibility involving the combined effect of the fluid pressure in the respective gap and the external pressure. The present investigation involves numerical and analytical studies as well as comparisons between the two.

Clashes are significant events. The typical clash occurs either near the leading edge of the body as in [11] or near the mid-body region as in [17]. The majority of the cases are found to yield a solid-solid clash within a finite scaled time as in [17]: see also the reviews in [32, 38]. The effects of an indentation in the containing channel and of flexibility in the wall of the channel on this phenomenon are to be investigated. Clashes within a viscous fluid are also examined in recent work [23, 23, 69, 15]. We focus however on a basic nonlinear problem assuming in effect oncoming plug flow in the undisturbed part of the channel; strictly this corresponds to the local fluid being already in motion prior to the body travelling through it. See figure 2.1. Our aim is to understand and provide predictions for configurations such as that in the figure, as well as tackling major analytical issues and the possibility of some continued oscillations arising between the freely moving body and the surrounding fluid flow. Again, recent analytical work [21, 70, 71] implies that significant body oscillations may occur within a fluid-body interaction under certain conditions such as for a front-heavy body; we intend to study this possibility here.

The layout of the paper is as follows. Section 2.1 describes the motion of a thin heavy body with or without camber passing through, and interacting with, the fluid in a straight channel. This is followed by section 2.2 which describes an analysis-based reduced system obtained for increased mass and moment of inertia and gives comparisons with the full solutions of the previous section. Oscillations are also discussed. Detailed wake effects are examined in section 2.3. The influences of distortions in the channel walls are addressed in section 2.4, while section 2.5 presents final discussion points and conclusions.

2.1 The straight configuration: numerical solutions

The concern in this section is with a single body which is thin but with, in general, non-zero thickness or camber (or both) and moving through fluid in a straight-walled channel as drawn in figure 2.2. With a subscript $\mathscr{D}$ denoting a dimensional quantity, the nondimensionalisation applied is based on the channel width $L_{\mathscr{D}}$, oncoming fluid flow velocity $U_{\mathscr{D}}$, pressure $p_{\mathscr{D}}$ and fluid density $\rho_{\mathscr{D}\mathscr{F}}$, while the body length is $L_{\mathscr{D}}/\mathscr{E}$ say with $\mathscr{E}$ being small. The interactions between body and fluid assume that the fluid is in effect inviscid and incompressible and the entire motion with unknown velocity components $U_{\mathscr{D}}(u, \mathscr{E}v)$ takes place in a two-dimensional $L_{\mathscr{D}}(x/\mathscr{E}, y)$ plane. The body is taken to have its angles of inclination during motion

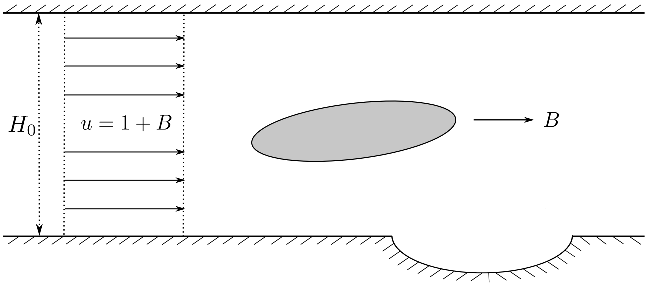

(a) Fixed channel

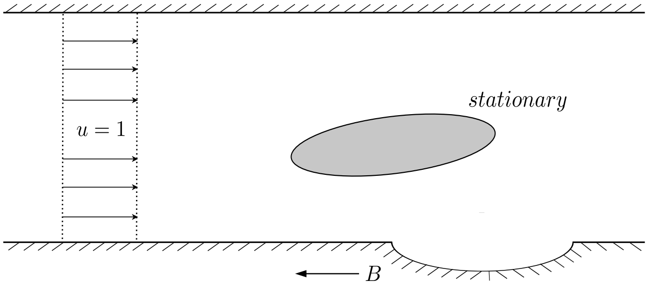

(b) Fixed body

Figure 2.1: (a) Sketch in non-dimensional form of a body moving with axial velocity B through a fixed channel (with an indentation shown); the overtaking fluid has uniform velocity $1+B$. Here undisturbed channel width $H_0 = 1$. (b) As in (a) but in the reference frame wherein the body is fixed: so the indentation moves upstream in relative terms if $B > 0$ but downstream if $B < 0$. (The case $B = -1$ corresponds to the body travelling into fluid at rest.)

being of the same small order, $\mathscr{E}$, as those of the containing channel. The angle θ shown in figure 2 is scaled such that the real angle is $\mathscr{E}\theta$, yielding typical slopes $\tan(\mathscr{E}\theta) \sim \sin(\mathscr{E}\theta) \sim \mathscr{E}\theta$, a property which is used in the formulation below.

The main objective is to examine a model for nonlinear interactions with a single body (occupying $0 \leq x \leq 1$) of uniform density $\rho_{\mathscr{D}\mathscr{B}}$ contained within side walls. Two-way nonlinear interaction takes place simply because the fluid dynamical forces lead to body movement which in turn affects the fluid motion. The background governing equations for the fluid are the continuity and Navier- Stokes equations and for the body are those of rigid body motion. The flow equations, given the above assumptions on thinness and the absence of incident vorticity, become the thin-layer system

$$H_{nt} + (H_n u_n)_x = 0 \quad \text{and} \quad u_{nt} + u_n u_{nx} = -p_{nx}, \tag{2.1}$$

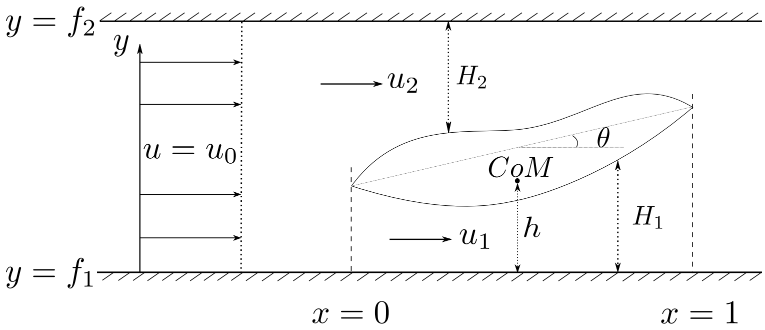

Figure 2.2: The body having both thickness and camber at a general position and orientation in the flow, with fluid-filled gaps $1,2$. Here, h is y-position of the body centre of mass (COM) measured from the lower wall; also $f_1 = 0$, $f_2 = 1$. The chord line, being the straight line through the leading and trailing edges, makes a small angle θ with the x-axis. The incident velocity $u_0 = 1$.

for $n = 1, 2$. Here H_n are the unknown thicknesses of the two fluid-filled gaps between the body surface and the walls, whereas u_n and p_n represent the corresponding unknown velocities and pressures in each region. The incident velocity is $u_0 = 1$ and the scaled pressure is zero upstream of the leading edge, without loss of generality. The system here applies for $0 \leq x \leq 1$ as, due to the drag force being relatively small, the axial velocity of the thin body is constant; this constant is zero in the current frame of reference. The body occupies the region

$$f^-(x,t) < y < f^+(x,t), \quad x \in [0,\, 1], \tag{2.2}$$

where $y = f^{\pm}(x,t)$ are the curves of the upper $(+)$ and lower $(-)$ surfaces of the body as it moves. At the leading and trailing edges, for closure,

$$f^-(0,t) = f^+(0,t) \quad \text{and} \quad f^-(1,t) = f^+(1,t). \tag{2.3}$$

The overall mass-conservation balance requires

$$\sum_{i=1}^{2} u_i(1\text{-},t)H_i(1\text{-},t) = 1, \tag{2.4}$$

by virtue of the incident conditions ahead of the body. Here in more explicit form the values

$$H_1 = h(t) + F_1(x) + (x-a)\theta(t), \tag{2.5a}$$

$$H_2 = 1 - h(t) - F_2(x) - (x-a)\theta(t) \tag{2.5b}$$

are the thicknesses of the regions of fluid flow between the lower wall of the channel and the lower surface of the body, and between the upper wall of the channel and upper surface of the body, respectively. Thus $f^+ = F_2(x) + h(t) + (x-a)\theta(t)$ and $f^- = F_1(x) + h(t) + (x-a)\theta(t)$. We allow the body to have arbitrary shape, with underbody and overbody shapes (when not moving) given by $y = F_1(x) = C(x) - T(x)/2$ and $y = F_2(x) = C(x) + T(x)/2$ with $C(x)$ and $T(x)$ being camber and thickness of the body, in turn. Note that $C(x)$ can be negative or positive. The condition at the body's trailing edge is in effect the Kutta condition requiring the flow to be smooth and this imposes on the fluid flow the constraint

$$p_1(1\text{-},t) = p_2(1\text{-},t) = \pi_e(t) \tag{2.6}$$

as another boundary condition, with the pressure value $\pi_e(t)$ being an unknown function of t. In order for the Kutta condition on $p_n(1\text{-},t)$ to be enforced at the trailing edge (TE), the interactive system requires the existence of a short Euler region of quasi-steady flow surrounding the leading edge (LE), in consequence of which we have

$$p_n(0+,t) + \frac{1}{2}u_n^2(0+,t) = \frac{1}{2} \tag{2.7}$$

from the Bernoulli theorem. The Kutta condition applies as each region of fluid flows enter into the common wake, requiring the pressures across the two gap regions to be equal there, whereas the velocities are unequal generally, thus allowing vortex sheets into the common wake. The fluid-dynamical part of the interactive motion has thus been described.

To determine the body motion equations, we neglect gravity and we should also note that the main force driving the body motion is the pressure force due to the fluid flow. Thus

$$Mh_{tt} = \int_0^1 (p_1 - p_2)\,dx, \quad I\theta_{tt} = \int_0^1 (x-a)(p_1 - p_2)\,dx = \tau. \tag{2.8}$$

Here τ is the torque applied on the body by the fluid flow, while θ_{tt} and h_{tt} represent the angular acceleration and linear acceleration in the positive y-direction respectively. Also M and I represent the scaled non-dimensional mass and moment of inertia of the body respectively, with I being at most $M/4$ for physical sense, while $a(= 1/2$ in this section) is the x-position of the centre of mass. Here M, I, u_0 and $F_1(X), F_2(x)$ are treated as given, and we intend to solve for the behaviour of the body, i.e. h and θ as functions of time.

Numerical solutions of the dynamic fluid-body interaction were derived using the method detailed in [11, 17, 72] among others. Figure 2.3 shows numerical evolutions of the system (2.1)-(2.8) for the body's leading and trailing edge positions and θ, $\dot{\theta}$ for increasing M and I values in a straight channel. The body has a sinusoidal nonzero thickness. The initial conditions are $(h, h_t, \theta, \theta_t) = (0.5, 0, 0.1, 0)$. The early motion is dominated by a linear increase in θ. The figure suggests that the resulting lift-induced migration to the wall and angular acceleration affect the flow more slowly for heavier bodies. The impact time was found as 2.3832, 3.0278, 3.4330 for $M = 2$, 6, 10 respectively. We now present an analysis for the effect of the enhanced mass and moment of inertia and of the centre of mass position on the fluid and body motions.

2.2 Analysis for the straight case

The computational results of the previous section point to some relevant new analysis in the present section concerning successively the effects of enhanced mass, reduced ratio of moment of inertia to mass and positional variation of the centre of mass.

First however, given that uniform flow with zero pressure variation constitutes an exact solution of the interaction system for the case of an aligned flat plate in the middle of the channel, small perturbations from the uniform state are of interest.

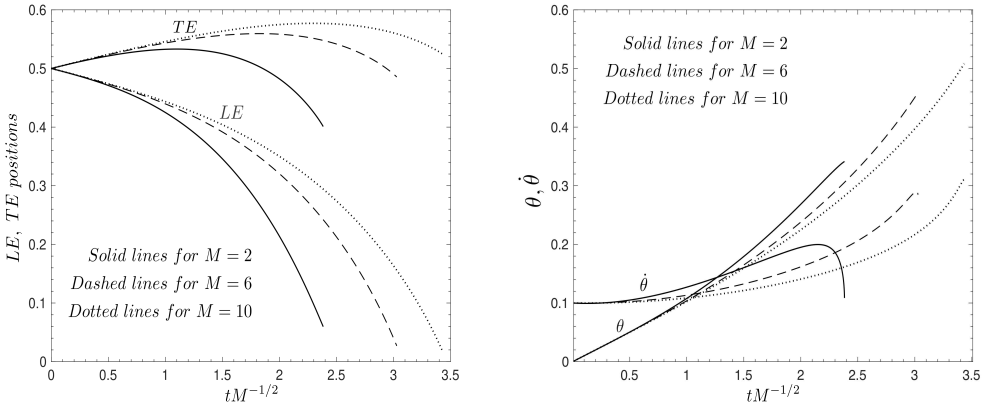

(a) LE, TE positions for $M = 2,\ 6,\ 10$ (b) $\theta,\ \dot{\theta}$ for $M = 2,\ 6,\ 10$

Figure 2.3: (a) Body leading edge (LE) and trailing edge (TE) positions for $M = 2,\ 6,\ 10$, $I = M/5$ and thickness $T(x) = 0.4\sin(\pi x)$, camber $C(x) = 0$, (b) angle θ , angular velocity $\dot{\theta}$.

These take the form

$$(H, u, p) = (\frac{1}{2},\ 1, 0) + O(\delta), \tag{2.9}$$

with $\delta \ll 1$. Substitution [11, 38] into the full system leaves at leading order linearised equations and conditions for the $O(\delta)$ perturbations in (2.9). When the body thickness is negligible the time-dependence becomes exponential, proportional to $exp(Qt)$ say. Thus (2.1) then yields, at order δ, the ordinary differential equation

$$Q\, H_n^+ + \frac{d}{dx}H_n^+ + \frac{d}{dx}u_n^+ = 0,$$

while (2.8) gives the integral constraints

$$Q^2 M\, h^+ = \int_0^1 (p_1^+ - p_2^+)\, dx,$$

$$Q^2 I\, \theta^+ = \int_0^1 (x-a)\, (p_1^+ - p_2^+)\, dx,$$

where $(H_n^+, u_n^+)\exp(Qt)$ are the $O(\delta)$ perturbations in (2.9). Similar working applies for the other quantities with superscripts '$+'$ and for the linearised versions of

(2.4) -(2.7). We are led to an eigenvalue equation for the constant Q, namely

$$Q^2\left\{(3M+1)\left(I+\frac{1}{180}\right)Q^3+\left(3MI+\frac{M}{10}\right.\right.$$
$$\left.\left.+\,4I+\frac{1}{20}\right)Q^2-\left(\frac{M}{2}-6I-\frac{1}{5}\right)Q+\left(\frac{1}{3}-M\right)\right\}=0. \tag{2.10}$$

The main concern here is in the cubic form inside the curly brackets, rather than the presence of two zero-Q roots (from the Q^2 factor outside) which are associated with uniform translation. Plots in [38] of the cubic form in the left-hand side of (2.10) establish that for any $M > 1/3$ there is a single eigenvalue with a positive real part, due to the signs of the terms in (2.10). The fact that this eigenvalue is $O(1)$ indicates the modelled interaction exhibits instability but only over the time scale of the complete interaction, not over shorter or longer time scales. See [11, 38]. In addition there is much current interest in the response for large M, I values with M, I remaining comparable. Here (2.10) shows that the relevant Q root then tends to zero, with

$$Q \sim (3I)^{-1/2} \quad \text{for} \quad M \sim I \gg 1. \tag{2.11}$$

The finding (2.11) suggests three features, specifically that the evolution slows down as M, I are increased, which makes sense physically, that the typical time scale increases like $M^{1/2}$ and that the variation of θ may come to dominate. These analytical features combine with the computations above to guide the following analysis.

2.2.1 Behaviour for large mass.

If the mass M is large and the moment of inertia I is comparable with M then the typical time scale t increases, as implied by Q becoming small in the linear result (2.11). In the nonlinear regime the time scale can be seen to grow like $M^{1/2}$ in view of the mass-acceleration-force balance in (2.8), given that when h is of order unity the velocity and pressure responses are likely to be also of order unity, which requires M/t^2 to be $O(1)$. Similar reasoning applies to the rotation motion balance. Hence $t = M^{1/2}t^*$ say, with t^* of order unity, and taking the initial conditions to involve no substantial velocities $dh/dt, d\theta/dt$ (e.g. for a body starting from rest) we have the expansion

$$(h, \theta,\ u,\ p) = (h^*, \theta^*, u^*, p^*) + \dots \tag{2.12}$$

with the scale of x and the body surface shapes remaining typically of $O(1)$. The velocities $dh/dt,\ d\theta/dt$ just mentioned are of order $M^{-1/2}$ and hence small. It follows that the fluid flow part of the whole interaction becomes quasi-steady; at leading order the governing equations of the flow remain as in (2.1) but with the time derivatives omitted and with asterisks inserted as per (2.12). Therefore the flows in the two gaps for $n = 1, 2$ are described by

$$u_n^* H_n^* = d_n^*(t^*) = \frac{{H_n}^*{}_{TE}}{H_0}, \tag{2.13a}$$

$$p_n^* = \frac{1}{2}\left\{\frac{1}{H_0^2} - \frac{d_n^{*2}}{{H_n}^{*2}}\right\}, \tag{2.13b}$$

from the quasi-steady mass conservation and Bernoulli property. Here the functions $d_n^*(t^*)$ depend only on the scaled time t^* as in (2.13a), the subscript TE denotes evaluation at the trailing edge $x = 1$ and, to clarify, the gap widths are $H_1^*(x,t^*) = f^- - f_1, H_2^*(x,t^*) = f_2 - f^+$ while in the present context $H_0 = 1, f_1 = 0, f_2 = 1$. Thus

$$H_1^*(x,t^*) = F_1(x) + h^*(t^*) + (x-a)\theta^*(t^*), \tag{2.14a}$$

$$H_2^*(x,t^*) = 1 - F_2(x) - h^*(t^*) - (x-a)\theta^*(t^*). \tag{2.14b}$$

The reduced system here then comprises (2.13a-2.14b) combined with the body motion part of the interaction in the form

$$\frac{d^2h^*}{dt^{*2}} = \int_0^1 (p_1^* - p_2^*)\,dx, \tag{2.15a}$$

$$I^*\frac{d^2\theta^*}{dt^{*2}} = \int_0^1 (x-a)(p_1^* - p_2^*)\,dx. \tag{2.15b}$$

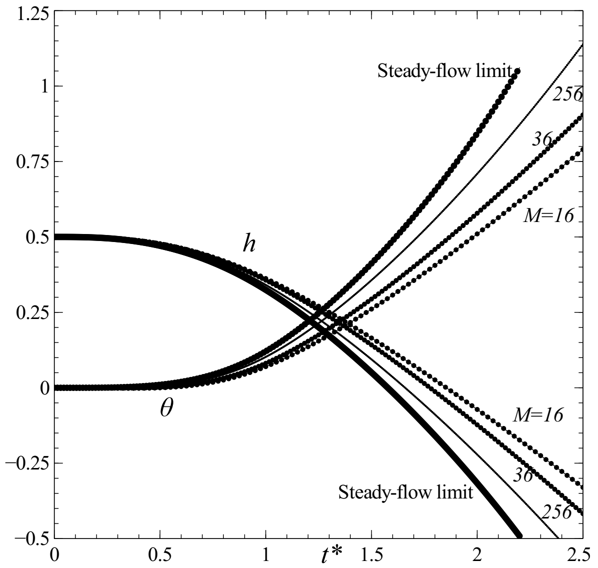

Figure 2.4: Evolutions of $h,\ \theta$ from the full system (with unsteady fluid and body motion) for M of 16, 36, 256 and from the reduced system (steady fluid flow), plotted against scaled time $t^* = M^{-1/2}t$. This is for a flat-plate body in a straight channel, with $I = M/5$ throughout. Dots indicate every 50^{th} data point.

Here I^* denotes the I/M body ratio of the moment of inertia relative to the mass.

Solutions of the reduced system (2.13a-e) are presented in figure 2.4. (Here and in certain other figures below the dots typically indicate every 50^{th} data point, for clarity of presentation.) Comparisons with the full numerical results prove to be useful and are also included in that figure. In figure 2.4 numerical results are shown for the evolutions of $h,\ \theta$ obtained from the full and the reduced systems for a flat plate body. The agreement is evident in terms of the trends of the evolution curves as $M,\ I$ increase.

2.2.2 Small ratio of moment of inertia to mass

Here we suppose additionally that the ratio I^* is small. Then, because of the balances of contributions in (2.15b), the time scale t^* decreases accordingly such that $t^* = {I^*}^{1/2}t^{**}$ say with t^{**} being of $O(1)$. This assumes the two gap pressures remain characteristically of order unity, from reasoning as in subsection 2.2.1. So the controlling equations (2.15a, e) become

$$\frac{d^2h^*}{dt^{**2}} = 0, \tag{2.16a}$$

$$\frac{d^2\theta^*}{dt^{**2}} = \int_0^1 (x-a)(p_1^* - p_2^*)dx, \tag{2.16b}$$

to leading order. The first equation gives simply

$$h^*(t^{**}) = h^*(0) + t^{**}\frac{dh^*}{dt^{**}}(0) \tag{2.17}$$

explicitly and so, on use of (2.13b) for the pressures, we are left with the single equation

$$\frac{d^2\theta^*}{dt^{**2}} = \frac{1}{2}\int_0^1 (x-a)\left\{\frac{H_2^*(1,t^{**})^2}{H_2^*(x,t^{**})^2} - \frac{H_1^*(1,t^{**})^2}{H_1^*(x,t^{**})^2}\right\}dx \tag{2.18}$$

which acts as an integro-differential equation for the scaled angle $\theta^*(t^{**})$. In (2.18) the terms $H_n^*(x,t^{**})$ are given by (2.14a), (2.14b) with t^* replaced by t^{**} but with h^* prescribed by the known form (2.17) as well as the body shapes $F_1(x), F_2(x)$ being known.

In the basic case of a flat-plate body $F_1(x), F_2(x)$ are zero. If in addition the initial velocity $dh^*/dt^{**}(0)$ is zero then, with the constant $h^*(0)$ written as β for convenience, the terms inside the integral on the right-hand side of (2.18) simplify somewhat since

$$H_1^*(x,t^{**}) = \beta + (x-a)\theta^*(t^{**}), \quad H_2^*(x,t^{**}) = 1 - \beta - (x-a)\theta^*(t^{**}). \tag{2.19}$$

The integral, which can be worked out analytically such as appendix C, is somewhat unwieldy, and as an alternative a straightforward numerical treatment can be applied to the reduced form (2.18), (2.19). The solutions of interest which are shown in figure 2.5 highlight that impact with one of the walls can still occur in this regime but also the beginnings of oscillations of θ^* with respect to time t^{**} are seen under certain conditions. The solutions for $h,\ \theta$ in figure 2.5 hint at the possibility of oscillatory solutions, in the sense that when the centre of mass is moved forward on

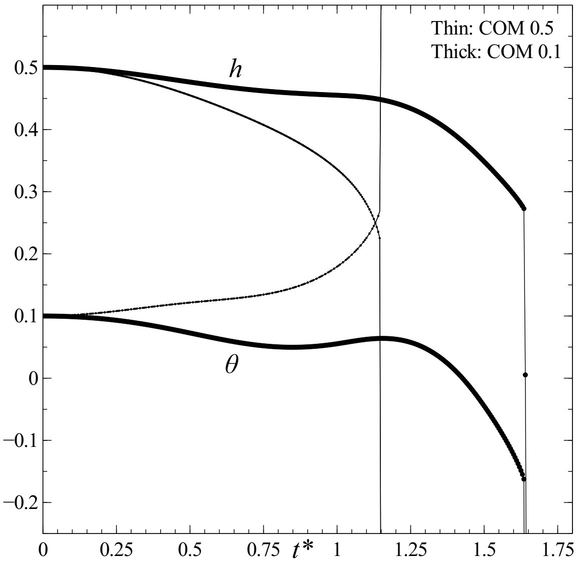

Figure 2.5: Solutions of the reduced form (2.13a-e) for $h,\ \theta$ vs t^* when the centre of mass location $x = a$ is varied from 0.5 to 0.1. Here $I^*(=I/M) = 0.2$. Vertical lines indicate a wall-body clash.

the body an undulation appears in the results and this acts to delay the impact with the channel wall.

2.2.3 Oscillations

The intriguing property of oscillations arising comes to the fore especially when the centre of mass 'a' is varied. A linearised analysis (given below) first shows this and indicates a critical value of $a = a_c = 1/3$ for the switch to oscillatory behaviour, as follows. The linearised analysis corresponds to the scaled angle θ^* in (2.18) being assumed to be small, with the constants $\beta,\ a$ remaining of $O(1)$ in general. Hence in view of (2.19) the following expansions are implied,

$$\theta^*(t^{**}) = \varepsilon\bar{\theta}(t^{**}) + \ldots, \tag{2.20a}$$

$$H_1^*(x,t^{**}) = \beta + \varepsilon(x-a)\bar{\theta}(t^{**}) + \ldots, \tag{2.20b}$$

$$H_2^*(x,t^{**}) = 1 - \beta - \varepsilon(x-a)\bar{\theta}(t^{**}) + \ldots, \tag{2.20c}$$

where $\varepsilon \ll 1$ is a measure of the size of θ^*, leaving $\bar{\theta}(t^{**})$ of order unity. Substitution into (2.18) leads to the linear equation

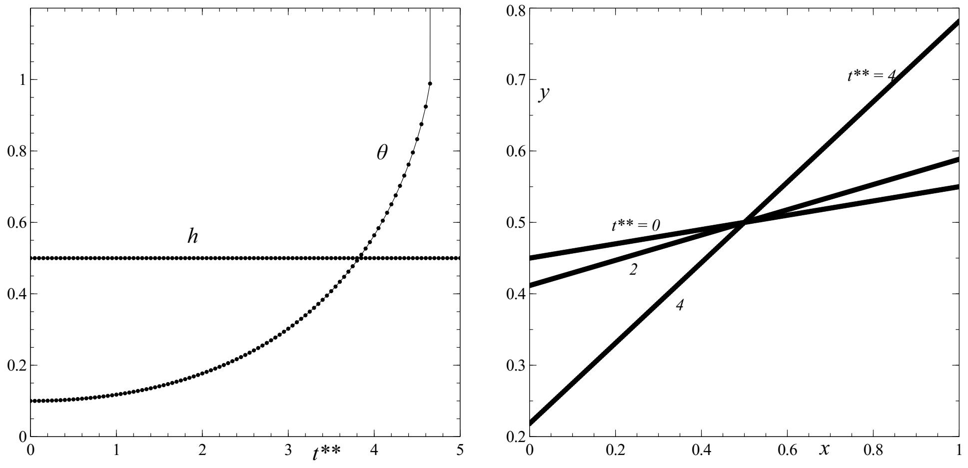

(a) (b)

Figure 2.6: (a) Evolutions $h,\ \theta$ plotted against scaled time t^{**} as discussed in section 2.2. (b) Body positions at times $t^{**} = 0,\ 2,\ 4$.

$$\frac{d^2\bar{\theta}}{dt^{**2}} = \frac{\bar{\theta}}{(\beta(1-\beta))}\int_0^1 (x-a)(x-1)dx, \tag{2.21}$$

from which the form

$$\frac{d^2\bar{\theta}}{dt^{**2}} = \frac{1}{2}\left(a-\frac{1}{3}\right)\frac{\bar{\theta}}{(\beta(1-\beta))} \tag{2.22}$$

is obtained. Here (2.22) confirms the critical value as $a_c = 1/3$. If $a > a_c$ then the small disturbance grows exponentially in t^{**}, whereas if $a < a_c$ then small oscillations are predicted: the frequency of such oscillations increases when the body is placed close to either wall where the value of β is near zero or unity. (This is a matter taken further in section 2.5.) Nonlinear solutions then support the finding. See figures 2.6, 2.7. Figure 2.6 shows the response over the t^{**} time scale with h remaining at its initial value of 0.5 throughout and θ gradually increasing, in 2.6(a), such that the flat-plate body clashes with the upper and lower walls almost simultaneously at a t^{**} value of about 4.5, in 2.6(b); the leading edge impacts on the lower wall and the trailing edge on the upper. The impact is indicated by the vertical line in 2.6(a). In figure 2.7, the centre of mass is at $x = 0.1$ instead of the usual value 0.5 and this is seen, in 2.7(a), to lead to oscillations. The largest oscillation which is for an initial θ equal to 0.55 displays the effects of nonlinearity through a movement of the peak and trough locations in particular, with the body's trailing edge almost but

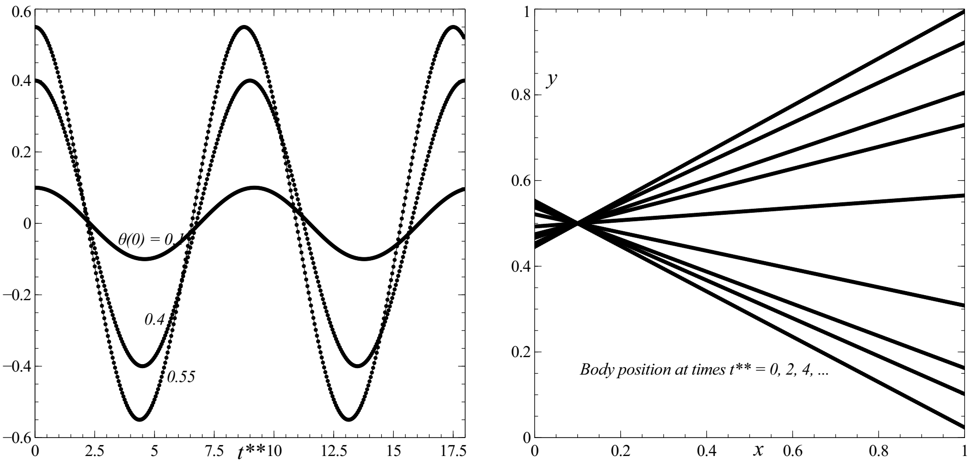

(a) (b)

Figure 2.7: Oscillatory interactions. (a) Angle θ vs t^{**} for initial conditions $\theta(0) = 0.1,\ 0.4,\ 0.55$ in the case $a = 0.1$. (b) Evolution of body positions for the 0.55 initial condition.

not quite hitting the walls as the oscillations continue.

The analysis appears to be in keeping with the numerical solutions of (2.18), (2.19). The analytical oscillatory response is also consistent with the earlier numerical work on the full system, particularly when I is large but significantly less than M.

2.3 Wake behaviour

The wake behind the body arises because the velocity components u_1, u_2 of the body-scale flow studied in section 2.1 are unequal in general at the trailing edge. This is shown by taking the integral of (2.1) with respect to x from the leading edge to the trailing edge, together with the Euler and Kutta conditions on pressure in (2.6), (2.7). Spatial and temporal evolution must therefore take place in the wake to restore uniform flow far downstream. The argument here is similar to that in section 2.1. In the wake, where $x > 1$, the absence of a solid body implies that the pressures p_1, p_2 must be equal but the dividing streamline, which marks the interface between fluid that has come from above the body in $0 < x < 1$ and fluid from below the body, is unknown in advance.

The relevant flow system to be solved in the wake $x > 1$ is thus

$$\frac{\partial H_n}{\partial t} + \frac{\partial (H_n u_n)}{\partial x} = 0, \tag{2.23a}$$
$$\frac{\partial u_n}{\partial t} + u_n \frac{\partial u_n}{\partial x} = -\frac{\partial p_n}{\partial x}, \tag{2.23b}$$

together with the pressure equality

$$p_1 = p_2 \tag{2.24}$$

and

$$H_1 + H_2 = 1. \tag{2.25}$$

Here (2.25) represents the feature that the thicknesses H_1 of the lower fluid flow and H_2 of the upper fluid flow must add up to unity, which is the overall width of the straight channel. The initial conditions are typically that

$$H_1 = H_2 = \frac{1}{2}, \quad p_1 = p_2 = 0, \quad u_1 = u_2 = 1 \quad \text{at time} \quad t = 0, \tag{2.26}$$

while the boundary conditions at the start of the wake, i.e. at $x = 1+$, are

$$(H_1,\, H_2,\, u_1,\, u_2,\, p_1,\, p_2)(1+,\, t) = (H_1,\, H_2,\, u_1,\, u_2,\, p_1,\, p_2)(1-,\, t), \tag{2.27}$$

for all $t > 0$. The form (2.27) matches with the fluid /body interaction properties considered in sections 2.1, 2.2 at the trailing edge of the body, with the Kutta condition assuring that $p_1,\ p_2$ are equal there and so the pressure can be continuous. It is notable that in the limit of large $M,\ I$ there is no wake effect to leading order because the flow contribution is then quasi-steady and so the Kutta condition on pressure leads to $u_1,\ u_2$ being equal in that case.

The system was solved numerically by means of an adjustment of the method described in [11, 17, 72]. In addition a linearised analytical solution appropriate for small perturbations from the state (2.26) is described in [72]: see also the analysis in (2.9-c). Analysis along the lines to be discussed in the following section also

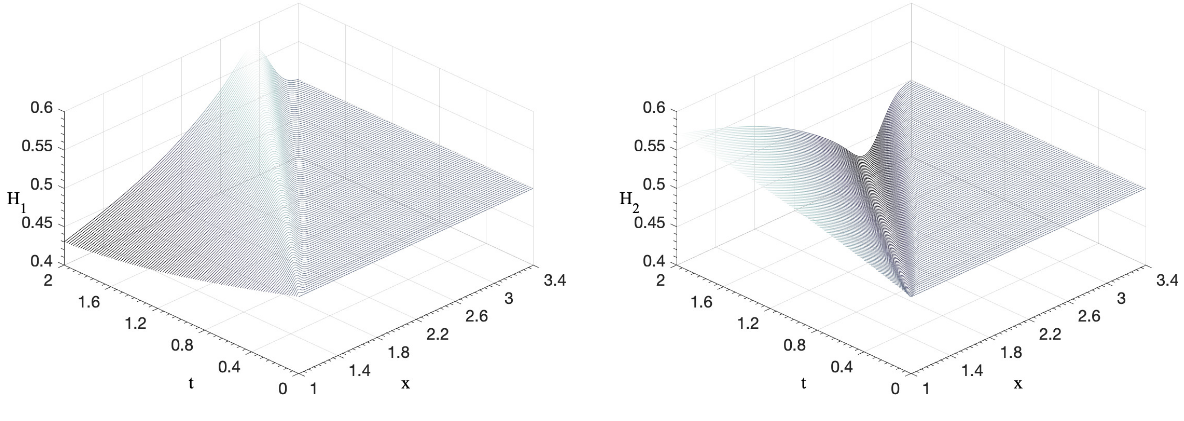

(a) (b)

Figure 2.8: Lower and upper layer widths H_1 and H_2 until time $t = 2$. Here $M = 10,\ I = 2$. (a) The lower layer width H_1 for $x \in [1,\ 3.4]$. (b) The lower layer width H_2.

applies in the wake part of the present interaction. Tests on the accuracy of the numerical work are given in [72].

The results are presented in figures 2.8-2.11. Figures 2.8-2.10 are for a thick body in $0 < x < 1$ with initial conditions $(0.5,\ 0,\ 0,\ 0.1)$ for $(h,\ dh/dt.\ \theta,\ d\theta/dt)$. Here figure 2.8 shows the lower and upper widths $H_1,\ H_2$, while figure 2.9 presents the velocities $u_1,\ u_2$ and figure 2.10 the pressure solution $p_1 = p_2$. The incident conditions (2.27) at $x = 1$ in figure 2.8a, b indicate that H_1 there decreases with time whereas H_2 increases, in line with (2.25). This temporal decay and growth in H_1, H_2 is arrested at larger x values however and replaced by growth and decay respectively, ahead of a travelling front, while downstream of that front the quantities given by the initial conditions in (2.26) remain undisturbed. Similar phenomena appear in figure 2.9a, b and figure 2.10. In all cases the existence of a travelling front is clear in the wake, the front speed being approximately unity as would be expected. Figure 2.11 exhibits the combined body-flow and wake-flow properties in terms of $u_1,\ u_2$ plotted against x between the body leading edge $x = 0$ and the wake position $x = 3.4$, for a range of times t as shown. In this interaction an impact of the body with the lower wall of the channel occurs at a time of about 3.4. Again the travelling front is apparent in the wake.

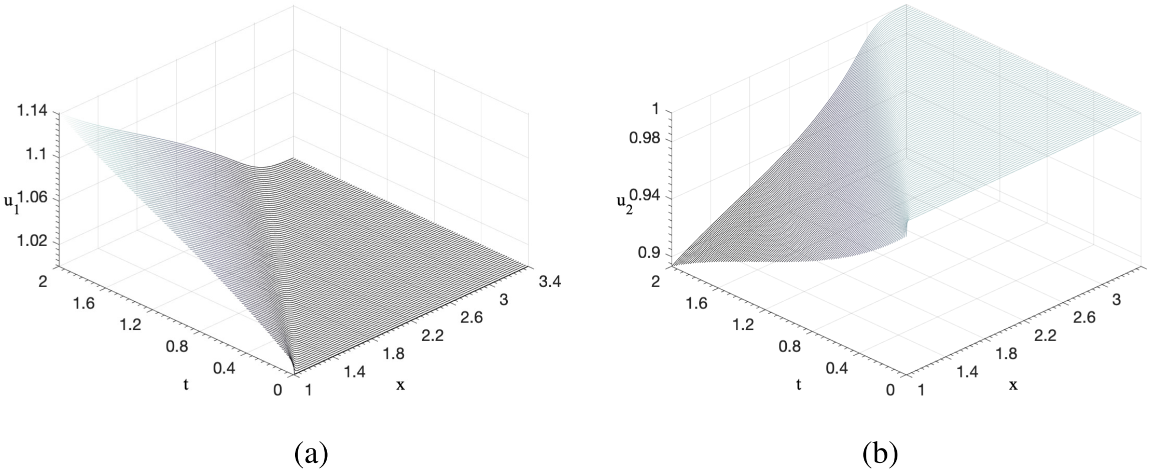

Figure 2.9: Velocities u_1 and u_2 in the wake region until time $t = 2$. Here $M = 10,\ I = 2$. (a) Velocity in the lower wake layer u_1 for $x \in [1,\ 3.4]$. (b) Velocity in the upper wake layer u_2. The initial conditions are as in figure 2.8.

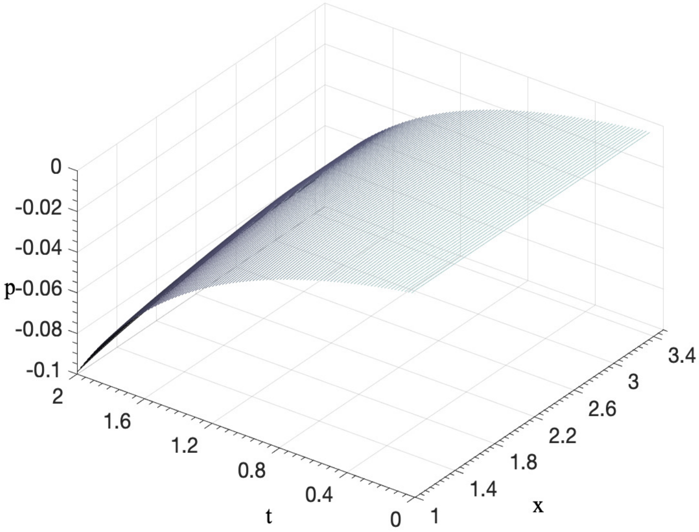

Figure 2.10: Pressure p solutions in the wake region until time $t = 2$.

2.4 Body motion through dilated or constricted channels

We consider here the effects of a continued dilation (expansion) of the channel width, in section 2.4.1, followed by a study of finite dilation or constriction in section 2.4.2.

2.4.1 Channel expansions

In the configuration studied in this section the lower wall is moving upstream, i.e. leftward, from right to left, with constant speed, relative to the body. Certain analytical features are worth describing first since they influence the coupling between the flow ahead of the body and that around the body in the fluid-body interplay.

Upstream of the body the wall eventually becomes distorted from its original straight form after a finite time, $t = t_0$ say. Since no body is present there the relevant governing equations are

$$H_t + (uH)_x = 0, \tag{2.28a}$$

$$u_t + uu_x = -p_x, \tag{2.28b}$$

for $x < 0$ (ahead of the body) but $x > x_0(t)$ (the position where wall distortion begins). Here (2.28a, 2.28b) applies across the whole channel. Let us assume that the incident velocity and channel thickness u_0, H_0 are maintained as constant in the straight channel far upstream. We suppose also that the lower wall is prescribed as $y = f_L(x,\ t)$, which holds for $x > x_0(t)$, when $x_0(t) < 0$. Upstream of $x = x_0(t)$ the channel remains straight. The upper wall is at $y = 1$ say. (In the body frame, we repeat, the body's leading edge remains at $x = 0$ and the trailing edge remains at $x = 1$.) Ahead of the leading edge, for $x_0(t) < x < 0$, we have (2.28a) with the gap width being $H = 1 - f_L(x,t)$. Hence $(uH)_x = \partial f_L/\partial t$ and integration in x then gives

$$uH(x,\ t) = u_0H_0 + \int_{x_0(t)}^{x} \left(\frac{\partial f_L}{\partial t}\right) dx, \tag{2.29}$$

and in particular at the onset of the leading edge

$$uH(0,\ t) = u_0H_0 + \int_{x_0(t)}^{0} \left(\frac{\partial f_L}{\partial t}\right) dx. \tag{2.30}$$

On the other hand, where the body is present, i.e. for $0 < x < 1$, we have the two kinematic balances $H_{1t} + (u_1H_1)_x = 0$ and $H_{2t} + (u_2H_2)_x = 0$ from section 2.1.

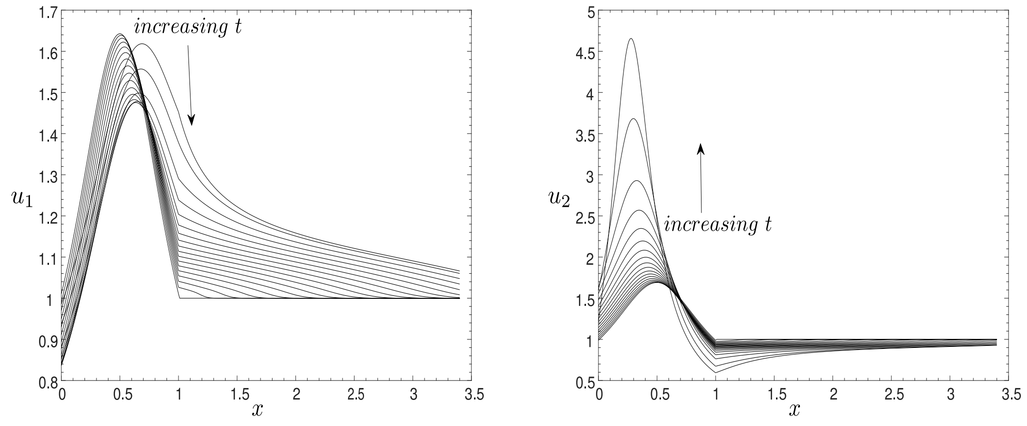

(a) (b)

Figure 2.11: Velocities for a body of profile $T(x) = 0.4\sin(\pi x)$, $C(x) = 0$, with $M = 10$, $I = 2$, approaching impact with the lower wall at the scaled time of t about 3.4. (Solutions are presented from time $t = 0$ to $t = 3.3$). (a) The velocity u_1 in gap 1 for $0 < x < 3.4$ (body and wake regions) and approaching the clash. (b) The upper layer velocity u_2. (The evolution in u_1 is sufficiently small over the whole time interval in the body region where $0 < x < 1$).

Integrating these two equations from $x = 0$ to $x = 1$ and adding the results gives us

$$\left(\frac{d}{dt}\right)\int_0^1 (H_1 + H_2)\,dx + (u_1H_1 + u_2H_2)(1,\,t) = (u_1H_1 + u_2H_2)(0,\,t). \qquad (2.31)$$

Then using the fact that $H_1 = 1 - f_+(x) - h(t) - (x-a)\,\theta(t)$ and H_2 is given by a similar formula, we find from (2.31) that

$$(u_1H_1 + u_2H_2)(0,\,t) = -\int_0^1 \left(\frac{\partial f_L}{\partial t}\right) dx + (u_1H_1 + u_2H_2)(1,\,t). \qquad (2.32)$$

However, the Euler region surrounding the leading edge contains quasi-steady flow and hence mass conservation in that region simply tells us that the left-hand side of (2.30) is equal to the left-hand side of (2.32). Therefore, from the right-hand sides we have

$$(u_1H_1 + u_2H_2)(1,\,t) = u_0H_0 + \int_{x_0(t)}^1 \left(\frac{\partial f_L}{\partial t}\right) dx. \qquad (2.33)$$

This is the main mass-conservation requirement. Using the result

$$u_1 = \left[c_1 - h'\,(x-a) - \frac{1}{2}\,\theta'\,(x-a)^2 + \int_{x_0(t)}^x \left(\frac{\partial f_L}{\partial t}\right) dx\right] / [h + \theta(x-a) - f_L] \quad (2.34)$$

(where $c_1(t)$ is an unknown function of integration, while we recall a is the position of the centre of mass) and a similar result for u_2, we then substitute these into (2.33). We are led to the mass-conservation requirement

$$c_1(t) + c_2(t) = 1, \tag{2.35}$$

which acts as a generalisation of the mass condition (2.4). It is notable that the integral in (2.34) has $x_0(t)$ as its lower limit; this leads to (2.35). In addition the momentum balance (2.28b) gives, on integration, the form

$$p + \frac{1}{2}u^2 = \frac{1}{2} - \int_{x_0(t)}^{x} u_t \, dx \tag{2.36}$$

for the pressure head. Hence in particular we obtain the result

$$(p + \frac{1}{2}u^2)(0-,\, t) = \frac{1}{2} + M^{-\frac{1}{2}}(1 + M^{-\frac{1}{2}})\mu x_0 \;/\; (1 + \mu x_0), \tag{2.37}$$

holding at the leading edge for the specific case addressed in the results shown in figure 2.12. Here $x_0(t) = 1 - M^{-1/2}t = 1 - t^*$, (2.37) holds for $t > M^{1/2}$ and μ is a constant. Figure 2.12 shows $h,\ \theta$ against t^* for the expanding channel, in 2.12(a), where the wall which is moving upstream relative to the body has shape $f_L = \mu(x - 1 + t^*)$ for $x > 1 - t^*$, with $\mu = -1$ in this example. Here 2.12(b) gives the evolving body positions as seen in the laboratory frame. We note that $h,\ \theta$ can be shown to grow in the form $O(t^*) + O(\ln t^*)$ at large t^* values within the expanding channel; the dependence on the centre-of-mass location a is implicit in the $O(t^*)$ term but explicit in the $O(\ln t^*)$ contribution.

Most significant for the fluid-body interaction are the channel width at the leading edge at any time t and the initial conditions at zero time on the velocities $u_1,\ u_2$. Both the channel width and the initial conditions are built in to the solution procedure, as is (2.35) to preserve total mass. By contrast, (2.37) does not affect the body-scale solution significantly. This is due to the property that an arbitrary function of t can be added to each of the pressures $p_1,\ p_2$ without altering the interactive

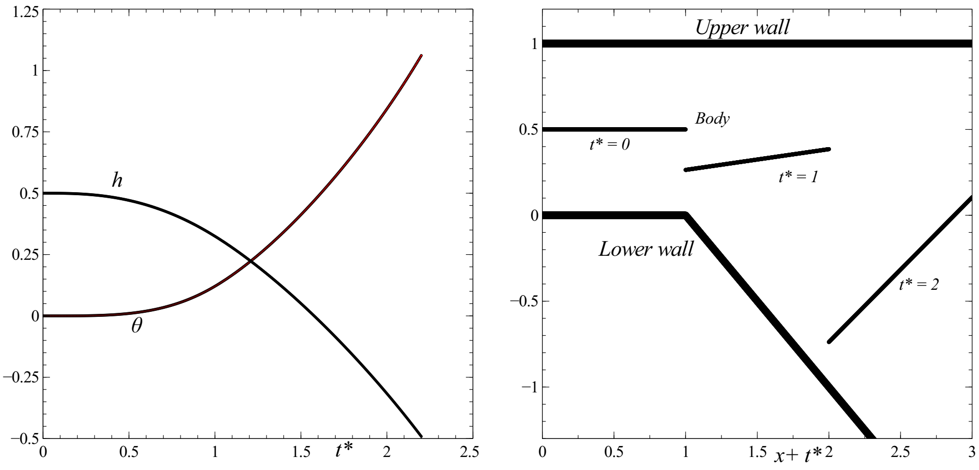

(a) (b)

Figure 2.12: For an expanding channel. Solutions of the reduced system (2.13a-e) with $I = M/5$ ($I^* = 0.2$) for a flat-plate body with centre of mass location $a = 0.5$. (a) $h,\ \theta$ vs time t^*. (b) Body positions in the channel at times $0,\ 1,\ 2$.

flow equations and, additionally, the fluid-body interaction itself involves only the pressure difference $p_1 - p_2$, as seen in (2.8), thereby cancelling out the arbitrary function just described.

Computational solutions for the fluid-body interaction are presented in figure 2.12. These are for the case of large $M,\ I$ as described in section 2.2 but now with channel expansion, such that in the laboratory frame the body is moving into a spatially expanding channel. The lower channel wall is given in the body frame by

$$f_L(x,\, t) = \mu(x + t^* - 1) \quad \text{for} \quad x > x_0(t^*),\ \text{zero otherwise,} \tag{2.38}$$

where $\mu = -1$ and $x_0 = 1 - t^*$. The upstream effect in (2.37) is small since M is large, while the initial conditions here correspond to a symmetric start at time zero (see also (2.9)) and the channel width at the leading edge increases as $1 - \mu(t^* - 1)$, that is, as t^*, for times $t^* > 1$. The figure shows the evolution of $h,\ \theta$ as well as the body and wall positions, with no impacts taking place in this example. It can be shown that for large times t^* the accelerations continue to reduce as the time scale increases and in effect the pressure approaches a stagnation value as the channel continues to expand.

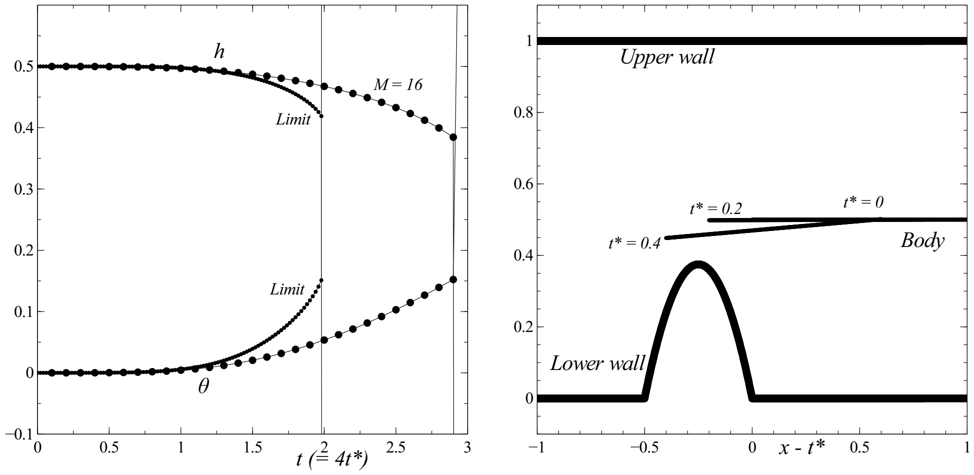

(a) (b)

Figure 2.13: In a constricted channel. Here again the ratio $I/M = 0.2$.
(a) $h,\ \theta$ solutions plotted against time $t = 4t^*(= M^{1/2}t^*)$ from full system at $M = 16$ (dotted curves) and from reduced system (labelled Limit). (b) The positions of the body at times $t^* = 0,\ 0.2,\ 0.4$ prior to impact, according to the reduced system. Comparisons for other M values are described in the text.

2.4.2 Finite dilation or constriction

The channel here is straight-walled except for the occurrence of a finite indentation or bump over which the moving body travels, such that in the present moving frame (the body frame) the indentation appears to enter the region of interest in the rightward direction with constant speed less than unity: in terms of figure 2.1 the constant B is negative in this case.

Considerations and analysis essentially identical with those in (2.28a)-(2.37) again apply ahead of the body here. This is relevant from the initial time because of the rightward motion of the lower wall in the present case. On the other hand the finite distortion, whether a dilation or a constriction, remains fixed in the laboratory frame in which the channel is stationary and we can expect the flow there to be steady at leading order, implying that in our body coordinates the effect upstream of the body depends only on $(x - \lambda t)$. Here λ is a given positive constant. Mass flux uH is conserved then, from the kinematic condition (2.28a), while the momentum balance (2.28b) now becomes

$$(u-\lambda)\, u_x = -p_x, \tag{2.39}$$

which can be integrated readily as in section 2.2 to yield the variation of the pressure head $(p+1/2\, u^2)$. Following this, however, the same comments as in section 2.4.1, on the pressure difference and on the significance of the channel width at the body's leading edge and the initial conditions, still hold in the current scenario.

The results shown in figure 2.13 are for the full problem (of (2.1)-(2.8)) with an M value of 16, for a finite constriction, with $\mu = -6$, together with a comparison with the result from the reduced problem (of (2.13a-e)) where $M,\ I$ are taken as asymptotically large. In the latter regime the wall-velocity factor λ is small and the upstream effect corresponding to (2.37) is negligible at leading order over the current time scales. As previously, the solution of the reduced problem is observed to capture the qualitative trend of the full solution; see also the next paragraph. In more detail, the results in figure 2.13 are specifically for a lower wall which produces a constriction, moving downstream relative to the body, with 2.13(a) showing $h,\ \theta$ and a comparison with the full-system results which suggests qualitative agreement. In contrast, 2.13(b) is presented in the laboratory frame and depicts the body evolution at three successive times. The position of the body at time $t^* = 0.2$ is altered only a little from that at time $t^* = 0$, with the leading edge seen to move upstream of its original position with hardly any body rotation, but by the time $t^* = 0.4$ the rotation has increased. The effective squeezing of fluid locally accompanied by a lowered pressure means that the body thereby approaches the constriction and then impacts upon it soon afterwards, at a t^* value of about 0.5 according to the calculation.

The comparison in figure 2.13 for M of 16 indicates that the approximate impact time predicted by the reduced system is $t = 1.98$, whereas that from the full system is $t = 2.89$. The ratio is thus 0.685. With I kept at the value $M/5$, the corresponding times for M of 64 are found to be 3.96 and 4.95 respectively, giving a ratio of 0.80, while for M of 256 we find 7.92 and 9.10 in turn and hence a ratio of

0.87. The trend, namely $0.685,\ 0.80,\ 0.87$, is encouraging as far as the approach to the limiting value of unity for the ratio at asymptotically large $M,\ I$ is concerned.

2.5 Discussion and conclusions

The study has sought increased understanding of the free movement of a slender body in a surrounding fluid flow within a channel. This is with two-way interaction being considerable between the fluid motion and the body motion and with fully unsteady evolution being active for both motions in general. The work has addressed numerical aspects for a thin or thick object inside a channel with straight walls and the corresponding analytical features for comparatively large values of the scaled mass and moment of inertia. The latter lead to a significantly reduced system. Oscillations coupling the body and the fluid motions have been found, including some particularly interesting ones which occur for relatively small values of the moment of inertia. Wake responses and the influences of non-straight walls associated with finite dilation and constriction or with continued expansion of the channel have also been investigated.

The main findings from the present modelling, analysis and computations, along with comparisons, are felt to be the following. First is the finite-time clashing of the body with the channel walls, which is a quite common phenomenon here, but there are means to avoid such clashing. The impact or clashing of the body when it does occur on a stationary or a moving wall is as in [11] if at the leading edge of the body or [17] in terms of a mid-body clash. However, a continuing expansion of the vessel is found to readily lead to the avoidance of such an impact. The second main finding concerns sustained oscillations. These are found to be possible as mentioned earlier and their occurrence can be supported clearly in analytical form. They arise especially for a front-loaded body. Third, wake properties behind the body show a distinct traveling front downstream. The fourth finding is concerned with the body flow through a dilated or constricted channel, which generates substantial nonlinear effects upstream of the body, whether the body travels leftwards towards the oncoming fluid flow or rightwards with the oncoming flow. Fifth is the broad agreement seen in the solution trends between full-system and reduced-system responses as the body mass and moment of inertia increase.

An interesting issue arises if the body lies near one of the walls. Suppose that the whole body is close to the lower wall (see figure 2.2), whether the wall is straight or otherwise; this is the the case of a thin flat plate if the wall is straight. To leading order the flow in the thin gap, of small thickness of order δ say, dominates the fluid-body interaction and gives a boundary-layer type of response as in [15] within region 1 of figure 2.2, the pressure p_1 being of order unity and satisfying the Kutta condition. Here region 1 refers to the gap where the fluid velocity has subscript unity and region 2 to the other gap above the body. This boundary layer implies that the height h and angle θ are known to leading order, with $O(\delta)$ relative corrections. (As a significant point here, the present argument supports the boundary layer analyses of [38, 15, 70, 73] in the sense that only the underbody pressure affects the body motion to leading order in the boundary layer case and also the fluid flow is quasi-steady if the scaled mass is relatively large.) At issue next is the question of how the solution in region 2 is determined. This appears to be by means of a linearized system in that region, which involves an $O(\delta)$ perturbation from the uniform incident stream and a corresponding pressure p_2 of order δ. The boundary condition on the top surface of the body now acts at zero y in effect. Combined with the no-penetration condition at the top wall, it indicates a behaviour similar to that studied in a single channel (section 2.4). The pressure p_2 can be found thereby and has a nonzero value generally at the trailing edge: this value provides a small corrective feedback to the pressure in the region 1. A similar reasoning applies to the wake of the near-wall body, a wake which is concentrated near the lower wall to leading order and is governed by the inviscid Burgers' equation, that is, by (2.23b) for $u_1(x,\ t)$ in $x > 1$ but with zero pressure p_1 in order to match with the majority of the flow at every wake station.

Potential future work has much of interest. It would be valuable to add in the influence of viscosity, for example as in [23, 23, 69], to admit three-dimensional interactions [68], and to include more than one body [74]. Similarly, the modelling of a flexible elastic wall or flexible body in the channel could be of great concern, not least because of the possible application to the tracing of vessel weaknesses described in the Introduction. We would also like to highlight the effects of reduced mass and moment of inertia, specifically in the eigenvalue equation (2.10). The reduction leads to one real negative root for Q along with two complex conjugates and corresponds directly to demanding that the right-hand sides of the body motion balances (2.8) be zero. Thus the pressures have to adjust to make the lift and moment integrals remain zero throughout the evolution. In this mass reduction case the time derivatives of the fluid flow stay significant, in contrast with the mass enhancement case of section 2.2 where the time derivatives of the body movements dominate the interaction. Work in [73] considers the mass reduction case in a boundary-layer context for an ice particle in water; it would be interesting to continue this case for the present internal flow configuration.

Chapter 3

Further examples and features of ”Fluid flow past a freely moving body in a straight or distorted channel”

3.1 Model creation

In the previous chapter, we reached some conclusions about the motion as single particle and some cases concerned with channel expansions. With those results, we find a possible constraint to keep our particle moving within the channel. We may have some oscillations or rotations during the particle movement. However, we can keep our particle moving between the parallel walls for a considerable time. That is felt to be possibly, in some settings, the most ideal form of the particle movement in real applications. In reality, on the other hand, the channel containing the sensors on airplane wings might not have straight or smooth walls. Thus, we should consider the effects of changing wall shape, such as by means of a sunken surface. In this chapter we undertake an investigation of wall-shape-changing accordingly.

With the above considerations, we would like as a first investigation to change the wall shape by means of the forms

$$f_L(t^*) = s_1 * t^{*2}, \; f_U(t^*) = 1 + s_2 * t^{*2}, \tag{3.1}$$

where $f_L(t^*)$ represents the shape of the lower wall and $f_U(t^*)$ represents the shape of the upper wall. It is notable here that the wall shape behaviour involving t^{*2} is just a very simple model to mimic the expansion of the channel. Really we would need a function of (x,t) say to allow for a fixed (originally fixed) shape of channel to enter the calculation domain and to then move across the domain from right to left. See particular examples in chapter 2. To be specific concerning the forms f_L,f_U above we also set the constants s_1,s_2 with s_1 between (-0.4,0.4), s_2 between (0,0.6). Thus we can change the height H_1 and H_2 as below,

$$H_1{}^* = f^- - s_1 * t^{*2}, \tag{3.2a}$$

$$H_2{}^* = 1 + s_2 * t^{*2} - f^+. \tag{3.2b}$$

Then we substitute the new variables H_1 and H_2 into equation (2.13a) to (2.15b). We obtain new relations as below,

$$u_1{}^* = \frac{d_1{}^*}{H_1{}^*} = \frac{d_1{}^*}{f^-(x,t^*) - s_1 * t^{*2}}, \tag{3.3a}$$

$$u_2{}^* = \frac{d_2{}^*}{H_2{}^*} = \frac{d_2{}^*}{1 + s_2 * t^{*2} - f^+(x,t^*)}, \tag{3.3b}$$

$$p_1{}^* = \frac{1}{2} - \frac{1}{2}(\frac{d_1{}^*}{f^-(x,t^*) - s_1 * t^{*2}})^2, \tag{3.3c}$$

$$p_2{}^* = \frac{1}{2} - \frac{1}{2}(\frac{d_2{}^*}{1 + s_2 * t^{*2} - f^+(x,t^*)})^2. \tag{3.3d}$$

where again $*$ represents the non-dimensional values,

With above relations, we apply the Kutta condition which has the form $p_1{}^* = p_2{}^*$ at $x = 1$. This leads to

$$(\frac{d_1{}^*}{f^-(x,t^*) - s_1 * t^{*2}})^2 = (\frac{d_2{}^*}{1 + s_2 * t^{*2} - f^+(x,t^*)})^2. \tag{3.4}$$

We assume $\alpha = 0.3$, $\beta = 0.1$, $h(0) = 0$, $\theta(0) = -0.1$, $COM(\text{center of mass}) = 0.5$ in the particle motion function (f^+ and f^-). By using these assumptions and the relation (3.4), we can easily derive the values $d_1{}^* = 0.25$ and $d_2{}^* = 0.75$ at $t^* = 0$.

Generally, because d_1, d_2, H_1, H_2 are real positive values, if we have $(\frac{d_1{}^*}{H_1*})^2 = (\frac{d_2{}^*}{H_2{}^*})^2$, we can draw the conclusion that $\frac{d_1{}^*}{H_1*} = \frac{d_2{}^*}{H_2{}^*}$. Then we use this relation along with equation (2.4), to reach the relation below,

$$d_1{}^* = \frac{H_1{}^*}{H_1{}^* + H_2{}^*}, \tag{3.5a}$$

$$d_2{}^* = \frac{H_2{}^*}{H_1{}^* + H_2{}^*}. \tag{3.5b}$$

Then we substitute equation (3.3c),(3.3d) into (2.8) to get the new core equations as below,

$$M^* \frac{d^2h}{dt^{*2}} = \frac{1}{2}\int_0^1 \{(\frac{d_2{}^*}{1 + s_2 * t^{*2} - f^+(x,t^*)})^2 - (\frac{d_1{}^*}{f^-(x,t^*) - s_1 * t^{*2}})^2\}dx, \tag{3.6a}$$

$$I^* \frac{d^2\theta}{dt^{*2}} = \frac{1}{2}\int_0^1 \{(x-a)\{(\frac{d_2{}^*}{1 + s_2 * t^{*2} - f^+(x,t^*)})^2 - (\frac{d_1{}^*}{f^-(x,t^*) - s_1 * t^{*2}})^2\}\}dx. \tag{3.6b}$$

The behavior of the nonlinear system will be considered below.

3.2 Effects of different channel expansion rates on the model

3.2.1 Rapid expansion

Heretofore we have studied a single particle moving in a channel of fixed shape and also investigated some particle movements with changing channel shape. Recalling the previous results, we now want to check in more detail how the channel expansion parameters s_1 and s_2 influence our model. To compare with the rapid expansion cases, first of all here, and consistent with what was mentioned in section 3.1, we set $\alpha = 0.3, \beta = 0.1, a = 0.1, s_1 = 0$ and $s_2 = 0$ for the case of a particle moving between fixed straight parallel-wall channel and the results shown in figure below,

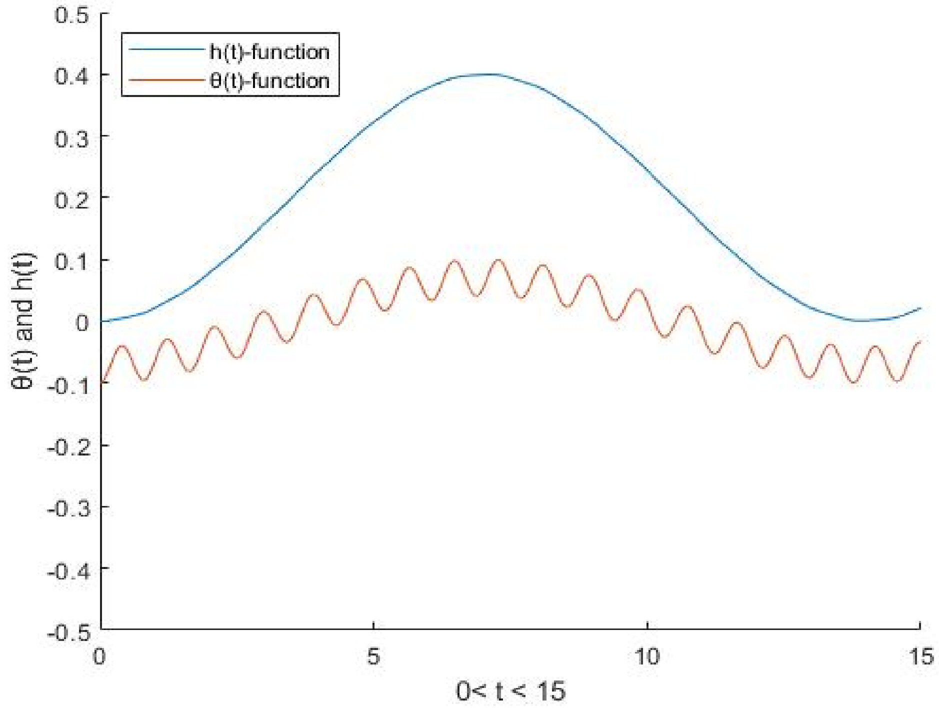

Figure 3.1: $h\ and\ \theta$ function for straight parallel wall case

From the figure 3.1, there is no abrupt change of the particle height function, which tells us that our particle can move between the parallel walls for quite a long time under the initial conditions we mentioned before. It is not difficult to see from the figure that the height curve of the particle forms a regular trigonometric function image. This means that the particle moves up and down regularly during its motion and does not collide with the wall. In addition, in the process of particle motion, its $\theta - function$ also shows that the particle oscillates regularly in the process of motion. Which means the oscillating angle and motion height of the particle both are changing regularly. The next step for the research is to change the wall shape with different values of the parameters s_1 and s_2 where s_1 and s_2 are the parameters for changing our model channel shape.

3.2.1.1 Effects of different s_1 and s_2 values on the model

Previously we have given images of h and θ equations for particle moving inside parallel channel. In this section, we will test the effect of different s_1 and s_2 on the particle motion. To avoid the model having a sudden change in its parameter space, we will start with a small value for both s_1 and s_2. In the following tests, unless otherwise stated, the following values are used as initial conditions. To control the variables, we choose the same initial conditions as figure 3.1 which $\alpha = 0.3, \beta = 0.1, a = 0.1$ but $s_1 = -0.01$ and $s_2 = 0.01$. Then we show the result as below,

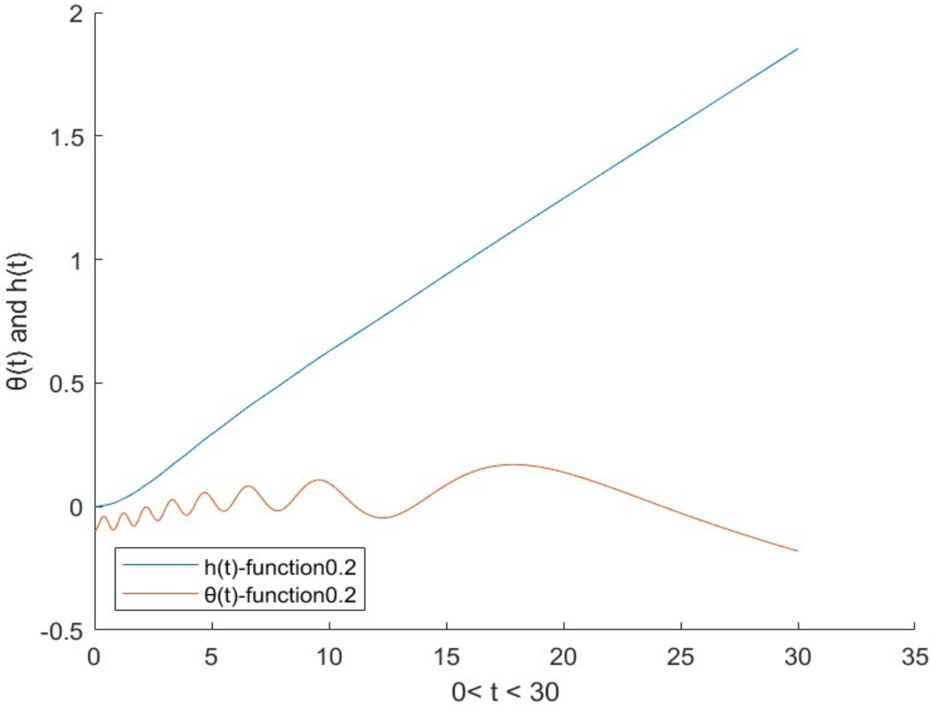

Figure 3.2: *h and* θ function for $s_1 = -0.01$ and $s_2 = 0.01$ case

At the very beginning, the height equation of the particle in figure 3.2 is similar to the height equation of the particle in figure 3.1. All have a gentle start. However, unlike figure 3.1, the height of the particle in figure 3.2 gradually rises with time, and there is no obvious sudden change. This means that the particle keep moving inside the channel and does not collide with the channel. Let's go ahead and increase the value of s_1 and s_2 to see how larger s_1 and s_2 affects the model. Thus we keep the initial conditions same as before but set $s_1 = -0.1$ and $s_2 = 0.1$. The result is shown below,

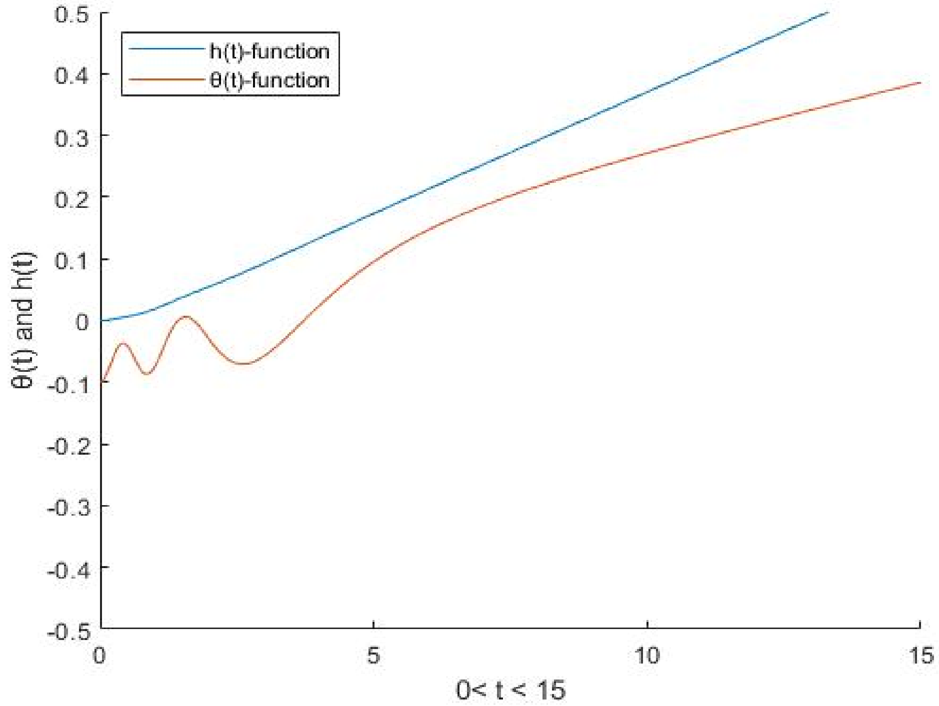

Figure 3.3: h *and* θ function for $s_1 = -0.1$ and $s_2 = 0.1$ case

It is not hard to see from this figure that the initial flat part in the height equation of the particle also disappears. In addition to this, we observe that the oscillation frequency of the particle is also reduced. This means the particle essentially reaches its 'stable' (asymptotic for large-time) state sooner than figure 3.2. Therefore we speculate that as the channel widens, the particle will reach the stable state faster. In order to verify this term, we chose a rather exaggerated value. Same as before, we keep the initial conditions but set $s_1 = -0.4$ and $s_2 = 0.4$ and the show the result as below,

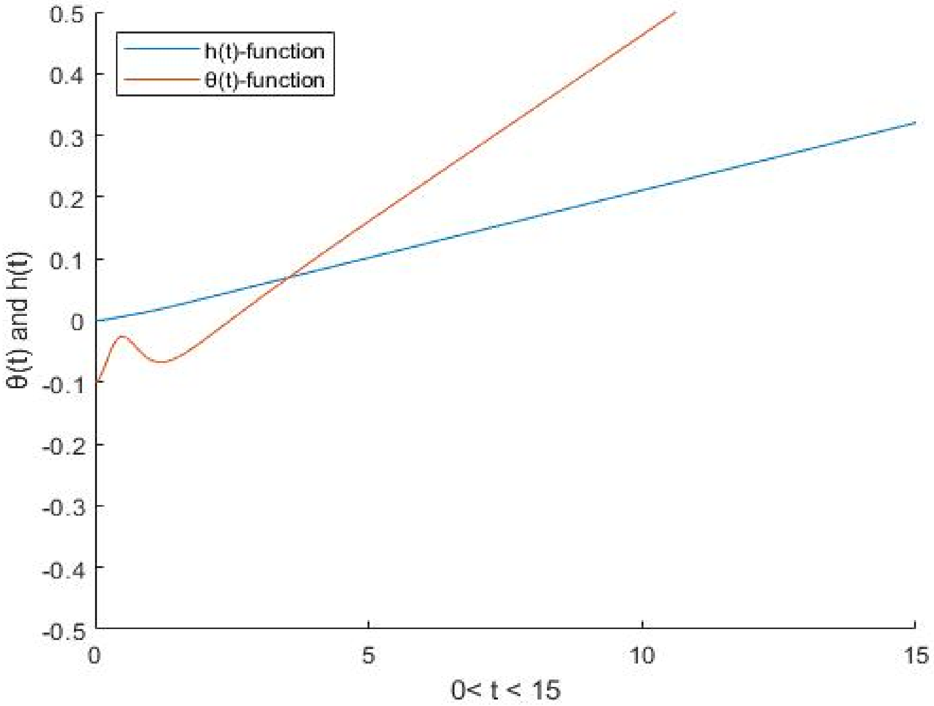

Figure 3.4: *h and* θ function for $s_1 = -0.4$ and $s_2 = 0.4$ case

From the figure, it is easy to see that the particle can move in the channel for a considerable time without colliding with a wall and reach the stable state faster than in previous cases.

One thing that needs to be noticed is that the θ we used here is a scaled θ^*. For the real angle θ_r, θ_r should be $\theta_r = \gamma\theta^*$, where $\gamma = \frac{L_2^*}{L_1^*}$ and L_2^* represents the non-dimensional channel width and L_1^* stands for the non-dimensional particle length. The θ_r is small as γ is small, but θ^* is an $O(1)$ quantity. If θ^* gets big, as in the cases where my plots show it increasing (or decreasing) linearly, then when θ^* is about the size of $\frac{1}{\gamma}$, the real angle is not small but $O(1)$. Thus my model is only valid for $1 \sim \theta \ll \frac{1}{\gamma}$. If $\theta \sim \frac{1}{\gamma}$, the model is not valid anymore and we would have to reconsider the model.

For the height function, we observe that when the absolute value of s_1 and s_2 increases, our h function shows that our particle may stay between the parallel moving walls for a longer time.

Previously we used the same increase for the coefficients s_1 and s_2. Only this kind of variation amplitude cannot fully show the interaction between particle and channel. Therefore, we will study the interaction between different shapes of channel and particle in the following research.

3.2.2 Effects of different absolute values of s_1 and s_2

Previously, we only consider s_1 and s_2 having the same absolute value. For the next step, we want to test what will happen if s_1 and s_2 do not have the same absolute value. For an example we set $s_1 = -0.2$ and $s_2 = 0.1$ and then we find the result shown in figure 3.5.

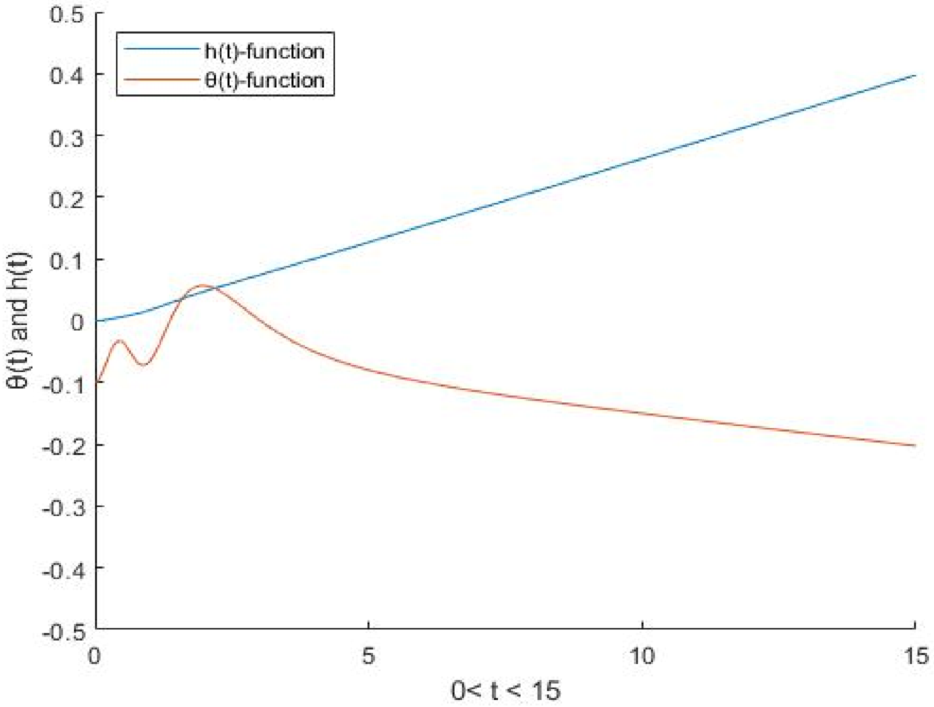

Figure 3.5: h and θ functions $s_1 = -0.2$ and $s_2 = 0.1$ (rapid expansion)

From the graphs we discover that there are some quantitative differences between the earlier results for the same absolute values of s_1 and s_2 in figure 3.2-3.4 and different absolute values of s_1 and s_2 in figure 3.5. However, the general direction of the graph is qualitatively similar to the results of the previous tests. Thus we would like to do some further test in the following chapters.

In the previous analysis we only considered expansions having opposite signs, which act to increase the gap width. Here we treat cases of s_1, s_2 having the same signs. First of all, we assume both s_1 and s_2 are positive. Thus we have 2 different situations:

1.$s_1 < s_2$, these changes can widen the channel.

2.$s_1 > s_2$, these changes narrow the gap.

The computational results obtained are described below.

3.2.2.1 $s_1 < s_2$ cases

Following tests show the results of first situation, which $s_1 < s_2$. In order to compare the cases where s_1 and s_2 are the same sign, as a control experiment, we keep the value of s_2 unchanged and set $s_2 = 0.4$ in the test. First of all, we started with a small value of s_1 and gradually increase the value of s_1 close to s_2. The following test shows the result of $s_1 = 0.01$,

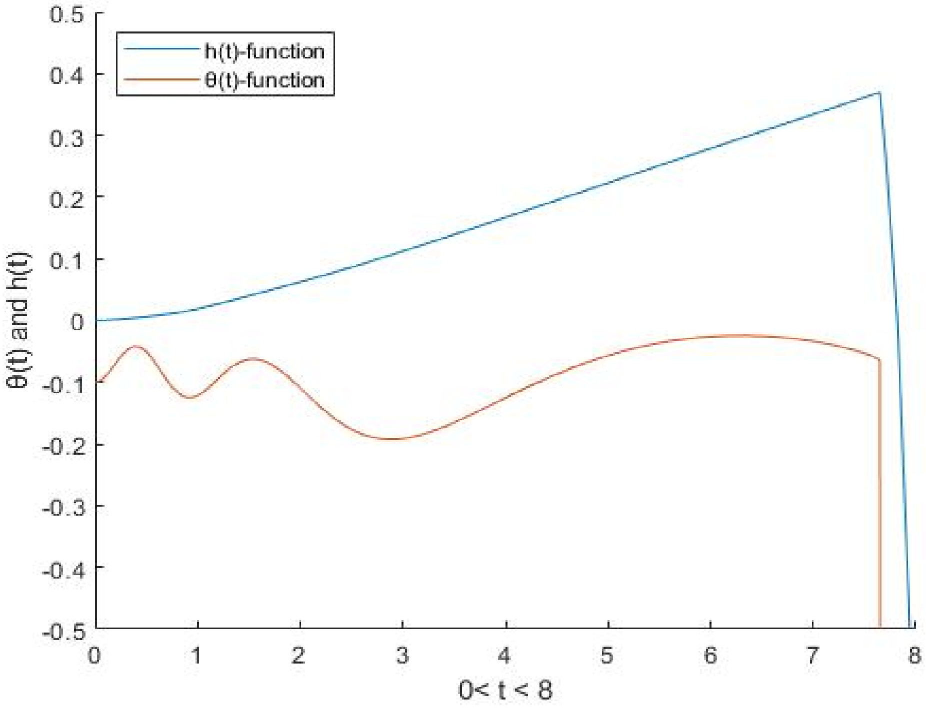

Figure 3.6: h and θ functions $s_1 = 0.01$ and $s_2 = 0.4$ (rapid expansion)

Figure 3.6 represents the height function(blue) and angular motion function(red) when we choose $s_1 = 0.01$ and $s_2 = 0.4$. From the graph we notice that there is a sharp decrease of the height function and the angular motion function. This is caused by our particle hitting the bottom wall. The whole movement of our particle is over. We believe this is caused by the bottom wall move up faster than the front-loaded particle ($COM = 0.1$). To test this, we use a faster upward speed for the bottom wall and the test result is shown below,

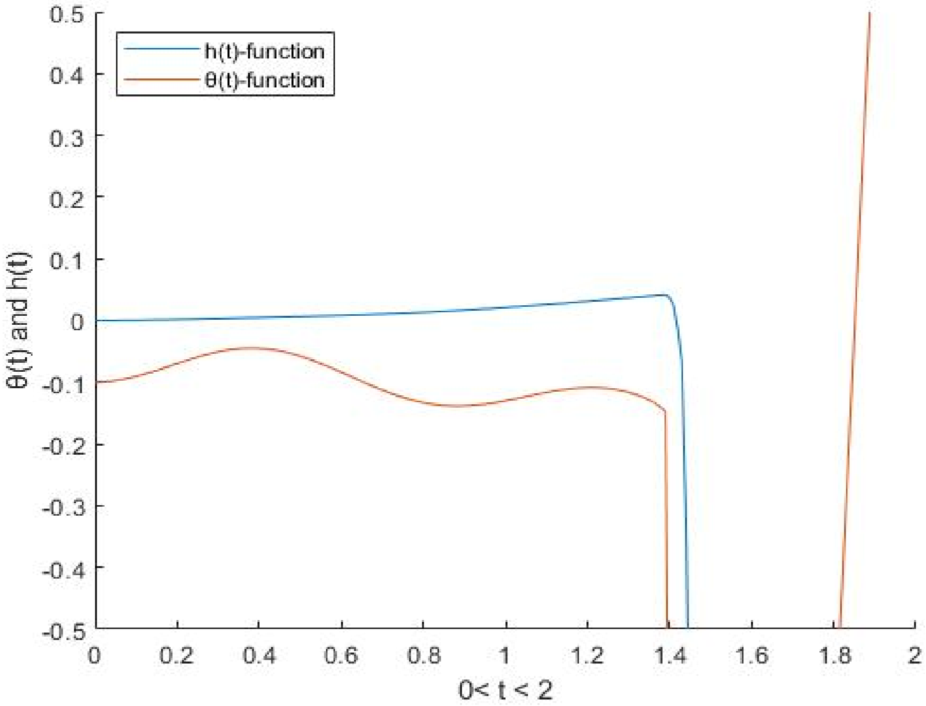

Figure 3.7: h and θ functions $s_1 = 0.1$ and $s_2 = 0.4$ (rapid expansion)

Figure 3.7 represents the height function(blue) and angular motion function(red) when we choose $s_1 = 0.1$ and $s_2 = 0.4$. From the graph we notice that the particle hits the bottom wall sooner than $s_1 = 0.01$ case. The conjecture is also verified here. We also did one more test with $s_1 = 0.3$ as below,

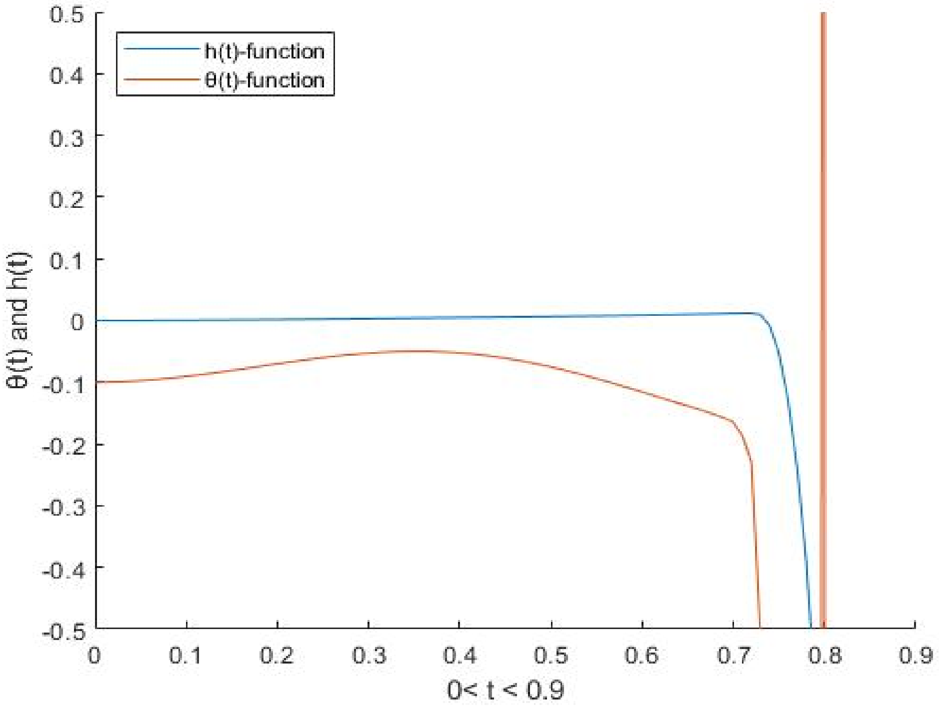

Figure 3.8: h and θ functions $s_1 = 0.3$ and $s_2 = 0.4$ (rapid expansion)

Figure 3.8 represents the height function (blue) and angular motion function (red) when we choose $s_1 = 0.3$ and $s_2 = 0.4$. From the graph we notice that the particle hits the bottom wall even quicker than $s_1 = 0.1$ case. This is also because our bottom wall is moving up quicker than $s_1 = 0.1$ case. In the future research, if we consider about the gravity, our particle may hit the bottom wall quicker.

We can conclude from the above three cases that the particles will collide with the wall during the process of movement, and as the upward movement speed of the lower wall increases, our particles will collide with that wall earlier. On the one hand, from the figure 3.6-3.8, we can find that the slope of the height function is much smaller than the value of s_1. On the other hand, the influence of the pressure caused on the particle is much less than the shape changing of the channel. Eventually, the particle will hit the bottom wall and the particle motion terminates.To verify that pressure does have effects during particle motion, we can compare the data in figure 3.6-3.8. Because of the effects of pressure, the collision time does not decrease proportionally when we increase s_1 proportionally. Thus in this case the smaller s_1 value we use, the longer time our particle moves. If the value of s_1 is negative, the particle will never collide with the wall under the given initial conditions.

In the previous 3 cases, we see that when $s_1 = 0.01$ the particle remains the longest between the parallel walls. Hence next we keep $s_1 = 0.01$ and gradually change the value of the parameter s_2. We set 3 new conditions as below,

1.$s_1 = 0.01, s_2 = 0.4$;

2.$s_1 = 0.01, s_2 = 0.2$;

3.$s_1 = 0.01, s_2 = 0.1$.

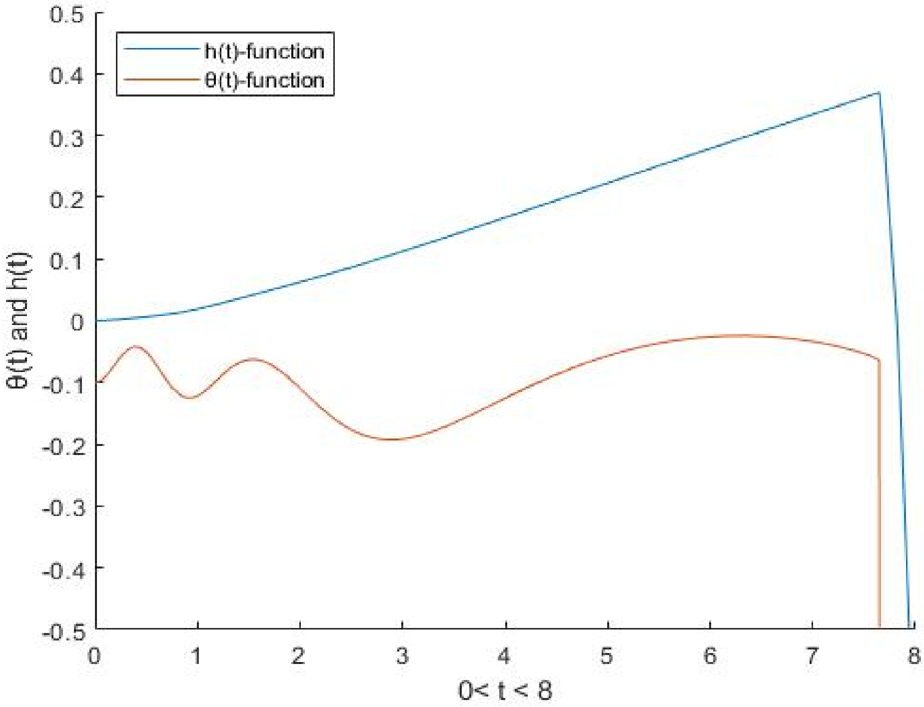

Figure 3.9: h and θ functions $s_1 = 0.01$ and $s_2 = 0.4$ (rapid expansion)

Figure 3.9 is the same as the figure 3.6. We put figure 3.9 here is just for comparing with other 2 conditions.

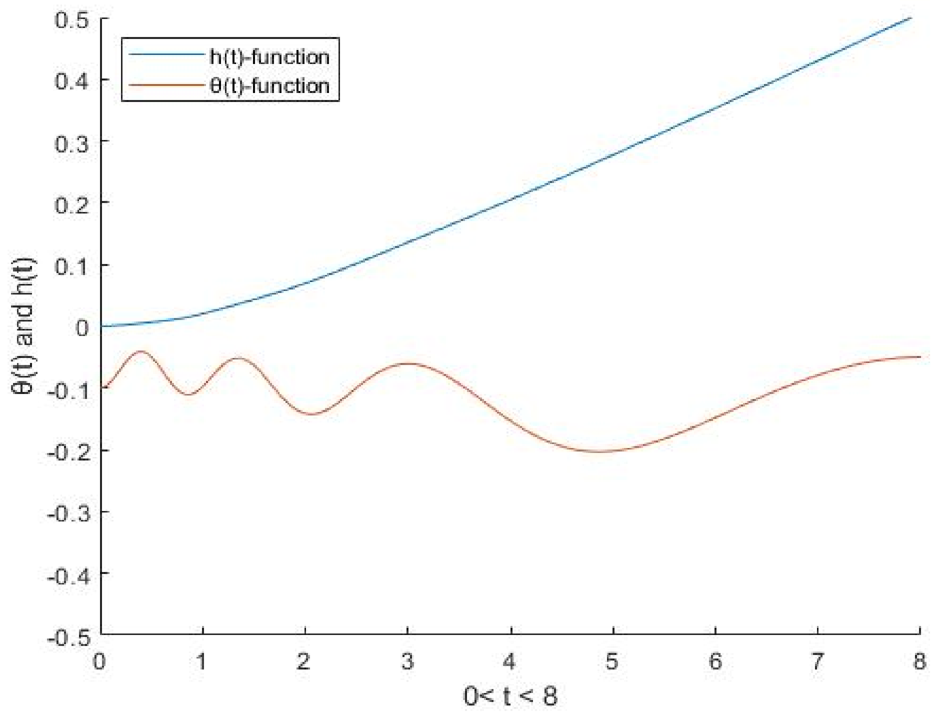

Figure 3.10: h and θ functions $s_1 = 0.01$ and $s_2 = 0.2$ (rapid expansion)

Figure 3.10 represents the height function (blue) and angular motion function (red) when we choose $s_1 = 0.01$ and $s_2 = 0.2$. From the graph we notice that our particle does not hit the wall, because there is not any sharply decreasing or increasing for either height function or angular motion function. Then we do one more case with $s_2 = 0.1$,

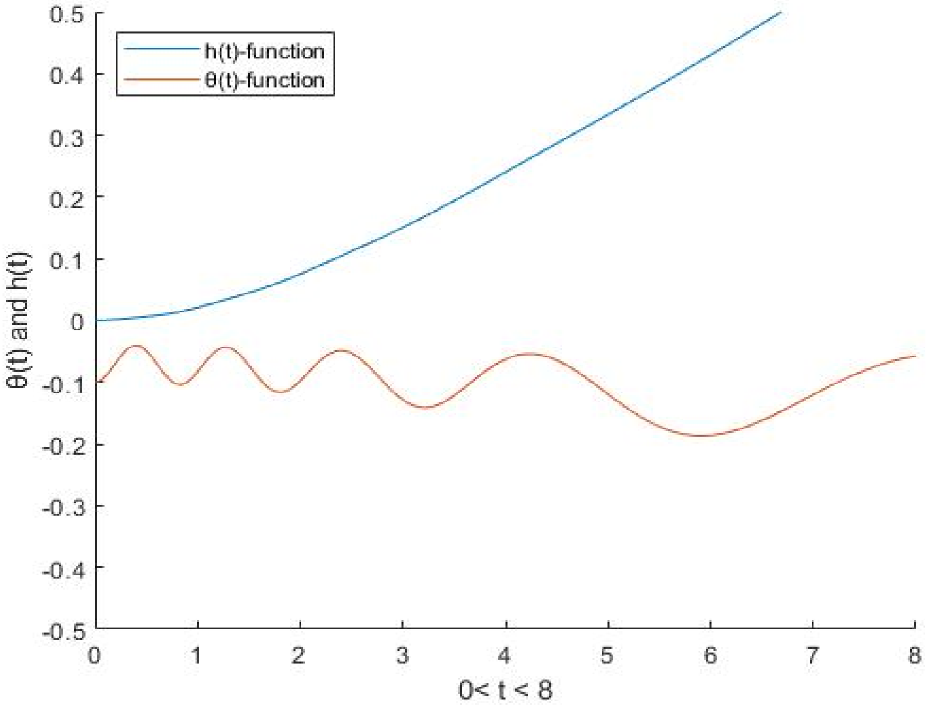

Figure 3.11: h and θ functions $s_1 = 0.01$ and $s_2 = 0.1$ (rapid expansion)

Figure 3.11 represents the height function (blue) and angular motion function (red) when we choose $s_1 = 0.01$ and $s_2 = 0.1$. From the graph we notice that from the slope that our particle can move in the channel for smoother time than $s_2 = 0.4$ case but not smoother than $s_2 = 0.2$. Therefore in order to make the particle move more smoothly in the pipe, we should not always reduce s_2.

One possible explanation is the pressure above our particle does not have such significant influence. As a conclusion, the particle will move smoother than $s_2 = 0.4$ case. Comparing this situation with $s_2 = 0.4$ and $s_2 = 0.1$, we found the slope for this situation is smoother than other 2 cases. The height equation of the particle indicates that the particle moves more gently.

3.2.2.2 $s_1 > s_2$ cases

Previously, we have already tested few different conditions about $s_1 < s_2$. Thus in this part we would like to focus on $s_1 > s_2$ case. Since when we set the values of s_1 and s_2 such that $s_1 > s_2$, the upper and lower walls gradually move towards each other with the channel suffering a contraction. In this situation we need only test one representative sample. We randomly choose $s_1 = 0.2$, $s_2 = -0.3$ as the initial conditions and keep others the same as we mentioned before.

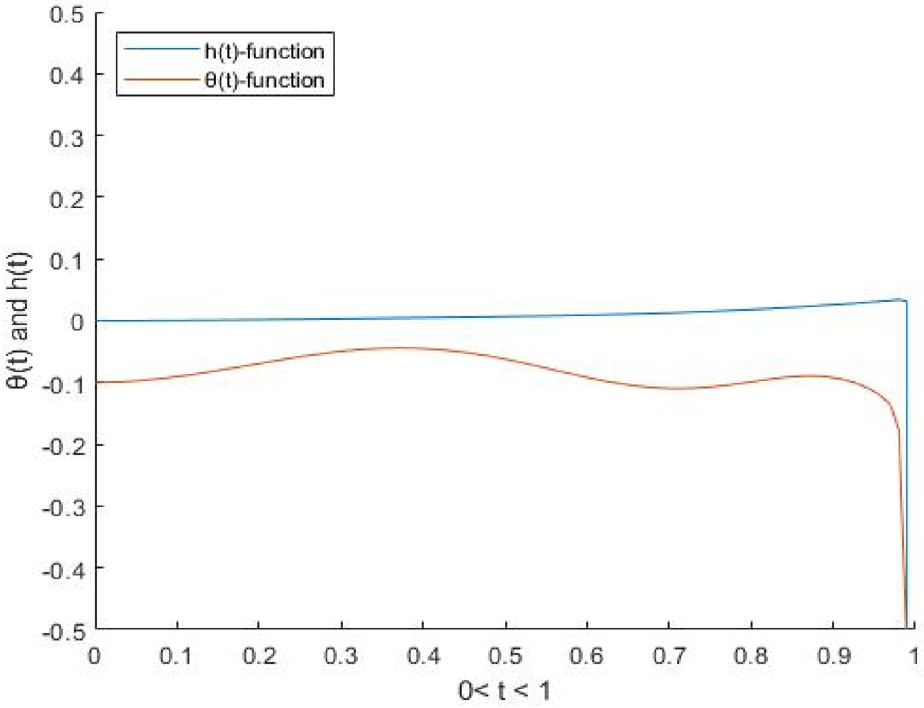

Figure 3.12: h and θ functions $s_1 = 0.2$ and $s_2 = -0.3$ (rapid expansion)

As we can see from the graphs in figure 3.12, there is a sharp change in the trajectory of the particle near scaled time t=1. This arises because the gap between the top and the bottom of the wall has shrunk to a value small enough for the particle to collide or even squeeze against the wall.

Previously we set the channel as a fixed shape. In this section we discuss some situations about different wall shape changing. First if we have a negative value of s_1 and positive value of s_2 and with s_1 decreasing and s_2 increasing, the particle can move in the channel for longer and longer time. This might be caused by the width of model channel is too big comparing with the size of our particle. Thus our particle can move ”freely” in the channel. Next we discuss about the s_1 and s_2 are both positive. Firstly, we set $s_2 = 0.4$ as a constant and we change the value of s_1. We notice that with the value of s_1 increasing, the particle will hit wall sooner and sooner. This is because the bottom wall moving up speed quicker than our particle moving up speed. As a result, our particle will hit the bottom wall. Secondly, we keep $s_1 = 0.01$ as a constant and change the value of s_2. Unlike before, the smoothest trajectory of the particle does not occur at the minimum value of s_2. Finally, we discuss the situation that $s_1 > s_2$, we notice the channel will close quickly. There is not enough space for our particle oscillating or moving up or down.

3.2.3 Modest expansion

Wall deformation involving st^2 (rapid expansion) is just one of the many possibilities we might encounter, but a simpler variation is change proportional to st. The latter gives modest expansion. We still use a scaled thickness of $\beta = 0.1$ to simulate the problems addressed here. We still use $\alpha = 0.3, \beta = 0.1, a = 0.1$ but $s_1 = -0.01$ and $s_2 = 0.01$ as the initial condition.

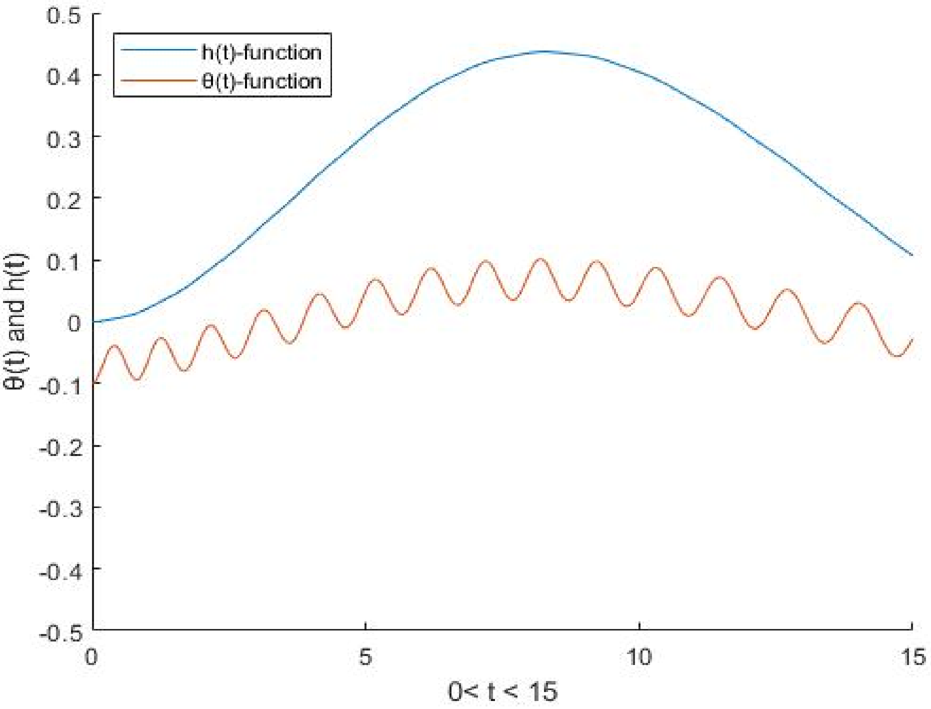

Figure 3.13: h and θ functions $s_1 = -0.01$ and $s_2 = 0.01$ (rapid expansion)

Figure 3.13 represents the height function (blue) and angular motion function (red) when we choose $s_1 = -0.01$ and $s_2 = 0.01$. Figure 3.13 compare with 3.2, it is not difficult to see from the figure that there is a clear difference between the height equation and the θ equation of the particle. For next step, we choose $s_1 = -0.1$ and $s_2 = 0.1$ as the second test.

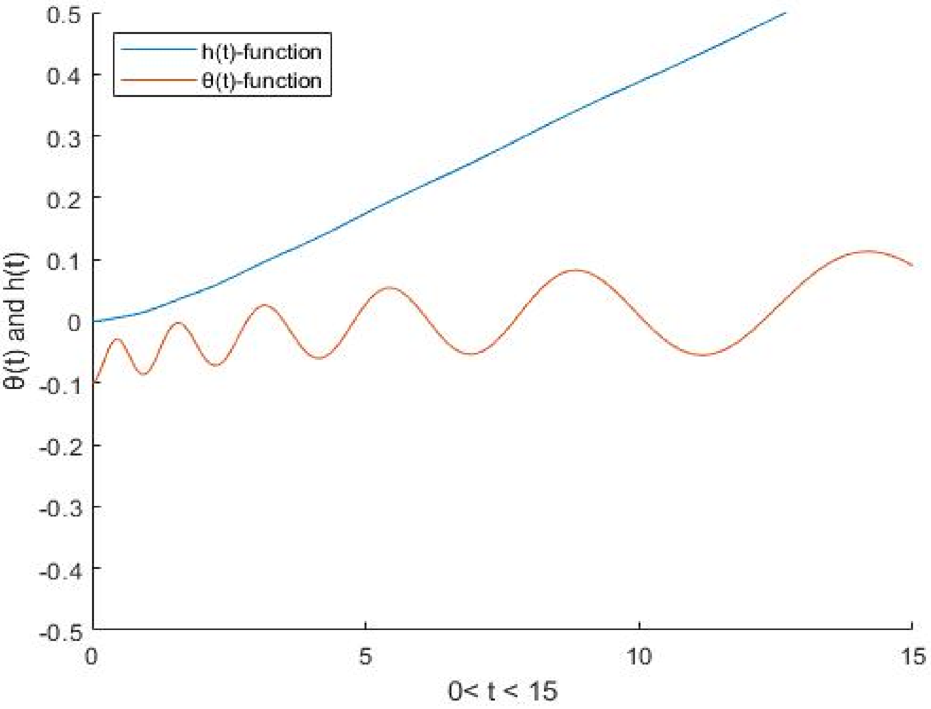

Figure 3.14: h and θ functions $s_1 = -0.1$ and $s_2 = 0.1$ (rapid expansion)

Figure 3.14 represents the height function (blue) and angular motion function (red) when we choose $s_1 = -0.1$ and $s_2 = 0.1$. From the graph we notice that due to the decreasing of the value of s_1 and the increasing of the value s_2, our particle can move more ”freely” than $s_1 = -0.01$ and $s_2 = 0.01$ case. As a result, our particle will hit the top wall with longer time. The figure below is the third test, where we choose $s_1 = -0.4$ and $s_2 = 0.4$ and the result is shown below,

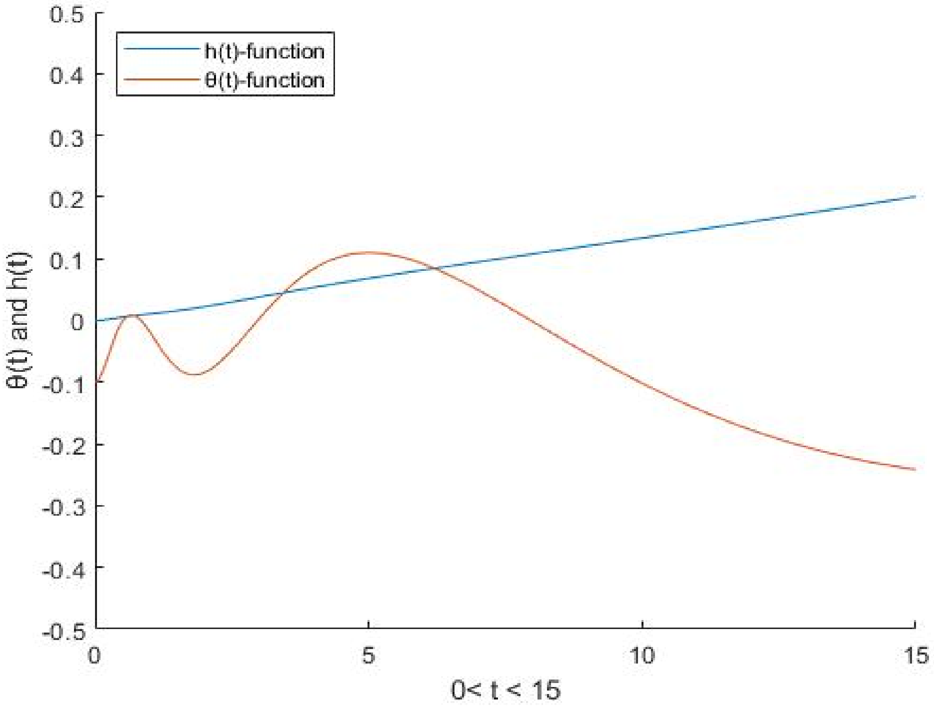

Figure 3.15: h and θ functions $s_1 = -0.4$ and $s_2 = 0.4$ (rapid expansion)

Figure represents the height function (blue) and angular motion function (red) when we choose $s_1 = -0.4$ and $s_2 = 0.4$. From the graph we notice that our particle will still move upward and the trajectory is smoother than figure 3.13 and figure 3.14. Figure 3.15 compared with figure 3.4, figure 3.15 has a smaller height variation. This means that in the part 3.2.3, the particle have smoother trajectories under same conditions.

From figures 3.13-3.15, we notice that the particle can keep moving between the parallel walls for a comparatively long time with some oscillations apparent in θ. When we earlier chose our parallel wall to be deformed like st^2, the pressure difference between the upper and lower parts of the particle had a larger impact on the response of the particle. In other words, the excessive pressure difference caused our particle to move up faster and perhaps in large time t, this will lead to a chaos motion. When we deform our wall shape like st, the pressure difference is not as big as st^2 model. In this case, our particle can move up slowly. Another feature that due to the pressure difference is smaller than st^2 model, the particle will move up less and in this kind of channel our particle has enough space to do some oscillations and we are more likely to predict the trajectory of the particle in this case.

In this chapter we have created several different simplistic models of an expanding channel and compared the results obtained, especially concerning whether the particle remains between the channel walls or instead collides with the walls over a given time interval. The study for a single particle movement with channel expansion finishes here as far as this thesis concerned. In the next chapter we will start on multi-particle problems.

Chapter 4

On interaction between freely moving bodies and fluid in a channel flow

This chapter, like chapter 2, is based on a recently published paper ”On interaction between freely moving bodies and fluid in a channel flow” by the present author, Samire Yazar and Frank T Smith. The paper appeared in the journal ”Theoretical and Applied Mechanics Letters” (2022). As before, we present the paper in full as follows.

4.1 Introduction

The motivation for this study on dynamic fluid/body interactions comes partly from the many practical application areas of these interactions. Included are significant issues of air vehicle safety concerned with the icing of external surfaces (wing, fuselage) or internal surfaces (engine) when impacted upon by ice particles, supercooled liquid droplets or other bodies or particles [1], [2], [3]. Similar issues arise for land and sea transport. Another wide area is in biomedical science where relatively small particles such as treatment drugs or thrombi travel through blood vessels [8], [9], [10] which are often relatively long. Yet another area is centred on environmental applications, for example the movement of dirt, dust and sand, both on Earth and on other planets. Finally here the application to food-sorting can be mentioned, involving for example rice grains travelling down a chute in order to be investigated systematically for defects [11]. The motivation is also partly from the intrinsic scientific interest and challenge of the interactive area, as distinct from that of the classical problem of fluid flow around a fixed body. During a dynamic fluid/body interaction the fluid motion affects the body motion because of the induced flow forces acting on the body surface but the moving body in turn alters the fluid motion around it by virtue of (e.g.) the kinematic conditions on the body surface and so there is two-way coupling.

One of our prime aims is to increase physical understanding of the mechanisms involved. We use rational modelling based on reduced equations, which then tend to shed light on the mechanisms by means of analysis and reduced computation [11], [17], [19], [74], [15], [67]. The study is meant to be complementary to direct numerical simulations [63], [64], [62]. In addition there has been much work on fluid/body interaction for a single body or particle: see inviscid-based theory in Refs. [11], [17], [19], [74], [15], [67] and viscous-inviscid interaction theory in Ref. [23], [23], [71], [21]. Among these works are found close connections between reduced-equation results of the type discussed in the current paper and the numerical findings from direct numerical simulation: see Refs. [23] and [21].

The specific interest in the present investigation is in fluid/body interactions for two or more bodies (finite-sized particles, objects) free to move in fluid within a straight-walled channel. This has practical connections with applications to engine dynamics [57] and food-sorting processes [75] in particular. Concerning the latter and its modelling, the situation is that many food objects such as peas or rice grains are projected down an inclined open chute for subsequent sorting [32]. The study in Ref. [11] addressed this scenario by consideration of many slender particles being present inside a channel through which fluid (air in their case) is flowing towards, around and past the particles in a coordinate frame fixed in the typical particle as opposed to the laboratory frame. The particles in the above study are assumed to be stacked, having identical lengths, being nearly parallel with the axial flow direction (horizontal say) and being aligned (vertically or laterally) such that their leading and trailing edges are sited at the same axial locations, namely at x values of zero and unity respectively where x denotes the scaled distance in the axial direction.

We aim to generalise the modelling in order to incorporate non-aligned bodies. That is, the bodies are taken to be stacked but with their leading and trailing edges being at different axial locations. In most applications of concern the representative Reynolds number and Froude number are very large, as in references above, and so as a very first model it seems reasonable to suppose viscous effects and gravity can be neglected. That being so we are led to the unsteady Euler equations of motion for the fluid flow and these are to be coupled with Newton's equations of motion for the bodies, yielding fluid/body interaction. The model at this stage is also to allow for the feature that the bodies of interest are slender in the sense that their typical lateral or vertical extent is significantly less than their axial or horizontal extent.

4.2 Model formulation for a single free particle in channel flow

For a single particle use is made of non-dimensional variables, namely Cartesian coordinates x^*(axial), y^*(lateral), time t^*, fluid velocity vector $u^* = (u^*, v^*)$ and pressure p^*, based on the channel width vertically, the typical incident flow velocity and the density ρ_{DF} of the fluid. Assuming viscous and gravity effects are negligible as discussed in the introduction we may then work within the framework of the Euler equations,

$$div\, u^* = 0, \quad u^*_{t^*} + (u^* \cdot grad)u^* = -grad p^*, \tag{4.1}$$

as regards the fluid flow. Here 'div' and 'grad' represent divergence and gradient respectively. The boundary conditions appropriate here are kinematic boundary conditions on the moving body surfaces and tangential flow (zero normal flow) at the fixed walls, along with a match with the oncoming flow $u^* = u_0(y)$ with zero v^* far upstream in the channel, where p^* is taken to be zero, and, after consideration of overall conservation of mass and vorticity, the same conditions are expected to apply far downstream as well. Thus

$$u^* \to u_0(y), \quad v^* \to 0, \quad p^* \to 0 \; as \; x^* \to \pm\infty, \; for \; 0 < y^* < 1. \tag{4.2}$$

There is clearly upstream influence ahead of the body and downstream influence aft of the body.

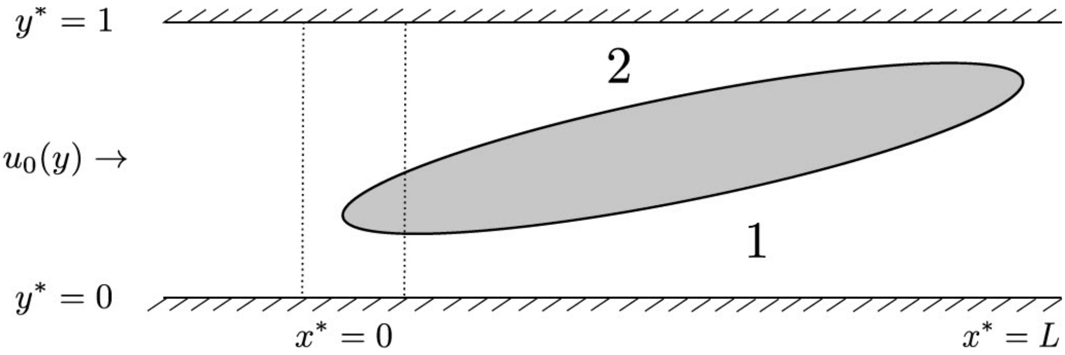

Figure 4.1: One body in channel flow, indicating regions 1, 2 below and above the body respectively. Upstream influence concentrates in the dashed zone when the body length L is large. The diagram is not to scale: the horizontal (x^*) scale has been reduced in comparison with the vertical (y^*) scale.

The slenderness of the body within the channel as shown in Fig. 4.1 now suggests scaling axial distances by the body length $L(\gg 1)$. The flow then acquires an interesting structure. First, the continuity balance implies that generally the lateral flow velocity scales with L^{-1} and so the solution form

$$(u^*, v^*, p^*) = (u, L^{-1}v, p), + ... \tag{4.3a}$$

$$(x^*, y^*, t^*) = (Lx, y, Lt), \tag{4.3b}$$

is indicated. This long-scale form applies in the two gaps between the body surface and the wall, for $0 < x < 1$, and it leads from Eq. (4.1) to the slender-layer equations

$$u_x + v_y = 0, \tag{4.4a}$$

$$u_t + uu_x + vu_y = -p_x(x,t), \tag{4.4b}$$

$$0 = -p_y, \tag{4.4c}$$

at leading order, where the y-momentum balance Eq.(4.4c) leaves p depending only on x, t. Second, due to the hyperbolic nature of Eq. (4.4a-4.4c), a different solution form is found to hold near the body's leading edge $x = 0$. Here, in a region sometimes called the Euler zone [11], [76],

$$(u^*, v^*, p^*) = O(1), \tag{4.5a}$$

$$(x^*, y^*, t^*) = (x^*, y, Lt), \tag{4.5b}$$

and so the Euler equations (4.1) hold in full except for the unsteady term $u^*_{t^*}$ which becomes negligible: the flow is thus quasi-steady. The boundary conditions on Eq. (4.5a, 4.5b) include the requirement Eq. (4.2) as $x^* \to \infty$, tangential flow at the walls $y^* = 0,\ 1$ and tangential flow on the leading-edge part of the body, a part which for all the body shapes studied herein appears as a flat horizontal plate because of the slenderness of the body. As $x^* \to \infty$, on the other hand, the conditions holding can be deduced from the Bernoulli relation since the flow is quasi-steady, giving conservation of $p^* + \frac{1}{2}(u^{*2} + v^{*2})$ along streamlines. These streamlines become effectively horizontal at large negative and positive x^*, as v^* tends to zero there, and hence a match with Eq. (4.2) upstream and with the form Eq. (4.3a, 4.3b) downstream is achieved.

In consequence the boundary conditions acting on the long-scale flow can now be written down completely. This is done here for the basic case of an incident profile $u_0(y) = 1$ corresponding to uniform or so-called plug flow far upstream. The conditions are

$$v = 0 \ at \ y = 0,\ 1 \ \text{(tangential flow on channel walls)} \tag{4.6a}$$

$$v = f_{nt} + u f_{nx} \ at \ y = f_n(x,t) \ \text{(kinematic conditions on body surfaces)} \tag{4.6b}$$

$$p + \frac{1}{2}u^2 = \frac{1}{2} \ at \ x = 0^+ \ \text{(matching with the Euler zone solution)} \tag{4.6c}$$

$$p = 0 \ at \ x = 1 \ \text{(the trailing edge constraint)} \tag{4.6d}$$

The condition Eq. (4.6c) coupled with the response Eq. (4.5a, 4.5b) in the

Euler zone accounts for the upstream influence mentioned earlier, while Eq. (4.6d) is the well-known Kutta requirement [11], [76] at the body's assumed non-blunt trailing edge. In Eq. (4.6b) $y = f_n(x,t)$ denotes the moving body surfaces for $n = 1,2$. Further progress can be made by observing that the vorticity is zero to leading order in this basic case, which leads to the replacement equations

$$H_{nt} + (H_n u_n)_x = 0, \tag{4.7a}$$

$$u_t + u u_x = -p_x(x,t), \tag{4.7b}$$

where Eq. (4.7a) replaces Eqs. (4.4a), (4.6a) and (4.6b), Eq. (4.7b) replaces Eq. (4.4b), (4.4c) and H_n are the two gap widths, namely $H_1 = f_1(x,t)$ and $H_2 = 1 - f_2(x,t)$. The fluid motion is therefore governed by Eq. (4.7a) and (4.7b) subject to Eq. (4.6c) and (4.6d). Initial conditions at time zero are supposed given also.

The body motion is governed by the mass-acceleration physics of a solid body of density ρ_{DB} whose centre of mass $(x,y) = (C, h(t))$ is moving vertically, combined with a scaled rotation angle $\theta(t)$, in response to the evolving pressure field from the fluid flow. The moving body surfaces are therefore given by

$$f_1(x,t) = F_1(x) + h(t) + (x - C)\theta(t), \tag{4.8a}$$

$$f_2(x,t) = F_2(x) + h(t) + (x - C)\theta(t), \tag{4.8b}$$

where $F_n(x)$ are the fixed underbody and overbody shapes, and we have at leading order the body-motion equations

$$M\frac{d^2h}{dt^2} = \int (p_1(x,t) - p_2(x,t))dx, \tag{4.9a}$$

$$I\frac{d^2\theta}{dt^2} = \int (x - C)(p_1(x,t) - p_2(x,t))dx, \tag{4.9b}$$

with the prime denoting the ordinary t derivative and M, I denoting the scaled mass and moment of inertia of the body. Account has been taken of the small angles inherent in the current slender-body analysis as well as the fixed axial positions $x = 0\,, C, 1$ of the leading edge, centre of mass and trailing edge of the body respectively in the present body-based coordinate frame.

Numerical and analytical properties of the fluid/body interaction Eqs. (4.6c), (4.6d), (4.7a), (4.7b), (4.8a), (4.8b), (4.9a) and (4.9b) are investigated in Ref. [19]. There is also interest in the regime where M and I are large and comparable, which occurs if the density ratio ρ_{DF}/ρ_{DB} is sufficiently small as for example with an ice particle moving through air: the density ratio in that example is about 10^{-3} . In this regime time t tends to scale like $M^{\frac{1}{2}}$ because of Eq. (4.9a) and (4.9b) and so the fluid flow becomes quasi-steady everywhere. Helpful simplifications then stem from Eq. (4.7a) and (4.7b), yielding conservation of $H_n u_n$ and $p + \frac{1}{2}u^2$ in each gap.

In the next section we extend the above modelling in order to describe the fluid/body interaction when two bodies are presented in a channel.

4.3 Model for two free particles in flow

Consideration is now given to two slender bodies interacting in a channel flow as depicted in non-dimensional form in Fig. 4.2. The bodies are non-aligned with their leading edges at different axial stations and likewise for their trailing edges. They also overlap in the sense that the leading edge of the second body (on the right) is positioned between the leading edge and the trailing edge of the first body (the body on the left). In the laboratory frame the bodies are moving with equal horizontal components of velocity and it follows that in the current body based frame they each have zero velocity in the horizontal direction, although able to move vertically and azimuthally, to leading order.

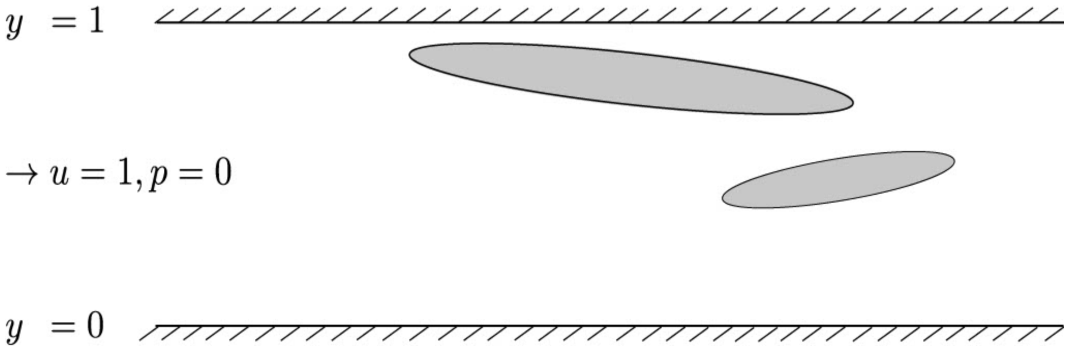

Figure 4.2: Two bodies in a uniform channel flow. The diagram is not to scale; as before, the horizontal (x) scale has been reduced in comparison with the vertical (y) scale.

Concerning the flow part of the fluid/body interaction, guided by the previous work as summarised in the previous section we suggest that there is a flow structure as shown in Fig. 4.3. This comprises five zones $1-5$. In Fig. 4.3 the dashed lines indicate the two Euler zones, surrounding the two leading edges of the bodies, and the two trailing edges where Kutta conditions apply. The lower and upper surfaces of the first body are written $y = f_1(x,t),\ y = f_2(x,t)$ respectively, while the lower and upper surfaces of the second body are $y = f_4(x,t),\ y = f_3(x,t)$ respectively: we note the ordering.

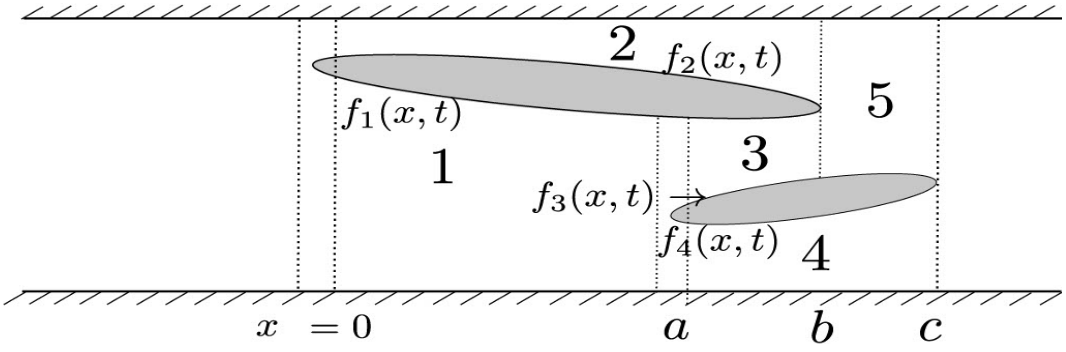

Figure 4.3: The interactive structure for two bodies, showing zones 1-5.

The density ratio is taken to be small and hence the flow can be treated as if steady, for the sake of simplicity in the present first modelling; the flow is assumed to be forward from left to right throughout such that $u_n > 0$ for all n. So, using and extending the assumptions and notation from the previous section, we have in the successive gaps ($n = 1-5$) the mass balances

$$u_n H_n = d_n (constants), \tag{4.10}$$

where the gap widths are $H_1 = f_1, H_2 = 1 - f_2, H_3 = f_1 - f_3, H_4 = f_4, H_5 = 1 - f_3$. Similarly the usual Bernoulli quantity is conserved throughout the zones $1-5$ because of the known properties of the Euler regions and hence

$$p_n + \frac{1}{2}\frac{d_n^2}{H_n^2} = \frac{1}{2}, \tag{4.11}$$

again holding for $n = 1-5$. There are expected to be jumps in pressure p and velocity u across the Euler regions in general but the quantities in Eq . (4.11) remain conserved across those regions.

Next, the total mass fluxes must be taken into account. These require the following relations to hold,

$$d_1 + d_2 = 1, d_3 + d_4 = d_1, d_2 + d_3 = d_5. \tag{4.12}$$

From the above relations we see that the required balances $d_4 + d_5 = d_1 + d_2 = 1$ also hold. Also the Kutta conditions at the two trailing edges $x = b,\ x = c$ are that the pressures there are equal, leading from Eq. (4.11) to the equations

$$\frac{d_2^2}{H_2^2(b,t)} = \frac{d_3^2}{H_3^2(b,t)}, \tag{4.13}$$

and

$$\frac{d_4^2}{H_4^2(c,t)} = \frac{d_5^2}{H_5^2(c,t)}, \tag{4.14}$$

in turn. The equality of the values in Eq. (4.13) with the value $\frac{d_5^2}{H_5^2(b,t)}$ implied by zone 5 is found to be assured, i.e. it is guaranted by the displayed equations above.

Thus there are five equations Eqs. (4.12), (4.13) and (4.14) for the five unknowns $d_1 - d_5$. The balances Eqs. (4.13) and (4.14) can now be simplified to give

$$\frac{d_2}{H_2(b,t)} = \frac{d_3}{H_3(b,t)}, \; \frac{d_4}{H_4(c,t)} = \frac{d_5}{H_5(c,t)}, \tag{4.15}$$

since all the velocities u_n are positive. Hence the solutions are found to be

$$d_1 = 1 - \frac{H_2(b,t)H_5(c,t)}{H_5(b,t)}, \tag{4.16a}$$

$$d_2 = \frac{H_2(b,t)H_5(c,t)}{H_5(b,t)}, \tag{4.16b}$$

$$d_3 = \frac{H_3(b,t)H_5(c,t)}{H_5(b,t)}, \tag{4.16c}$$

$$d_4 = H_4(c,t), \tag{4.16d}$$

$$d_5 = H_5(c,t). \tag{4.16e}$$

These are to be used in conjunction with the body-movement properties described below. It is notable meanwhile that a non-overlapping scenario would involve zero feedback between the two bodies because of the Kutta condition and the ensuing lack of a wake in the present quasi-steady flow model for small density ratios.

Concerning the body motions, the two bodies have to move by virtue of the mass-acceleration effects. Thus

$$M_1\frac{d^2h_1}{dt^2} = \int_0^a (p_2 - p_1)dx + \int_a^b (p_2 - p_3)dx, \tag{4.17a}$$

$$I_1\frac{d^2\theta_1}{dt^2} = \int_0^a (x - C_1)(p_2 - p_1)dx + \int_a^b (x - C_1)(p_2 - p_3)dx, \tag{4.17b}$$

$$\tag{4.17c}$$

for the first body and

$$M_2\frac{d^2h_2}{dt^2} = \int_a^b (p_3 - p_4)dx + \int_b^c (p_5 - p_4)dx, \tag{4.18a}$$

$$I_2\frac{d^2\theta_2}{dt^2} = \int_a^b (x - C_2)(p_3 - p_4)dx + \int_a^b (x - C_2)(p_5 - p_4)dx, \tag{4.18b}$$

(4.18c)

for the second body. The right-hand sides in Eqs. (4.17a), (4.17b), (4.18a) and (4.18b) depend on the pressure differences to be calculated from the fluid flow. We also need to relate h_1 , θ_1 , h_2 , θ_2 to the gap widths $H_1 - H_5$ and to the prescribed shapes of the body surfaces

The properties resulting from the interactive equations of the fluid flow in Eqs. (4.11)-(4.16e) and the bodies' motions in Eqs. (4.17a), (4.17b), (4.18a) and (4.18b) are investigated in the following section.

4.4 Results and discussion for two particles in flow

Here for the sake of numerical and analytical study we would like to consider concrete examples of the previous model configurations. What we are particularly interested in is investigating how to make particles remain between the parallel channel walls for as long as possible without any impacting on each other or on the walls. Our current study stops when one of the particles collides with the wall, either the top or the bottom wall, or when there is a particle-particle impact. It is necessary now to address specific examples.

In detail, the equations for the unknown moving body surfaces are now taken to be as follows,

$$f_1(x,t) = F_1^-(x) + h_1(t) + (x - \frac{1}{2})\theta_1(t), \tag{4.19}$$

$$f_2(x,t) = F_1^+(x) + h_1(t) + (x - \frac{1}{2})\theta_1(t), \tag{4.20}$$

$$f_3(x,t) = F_2^+(x) + h_2(t) + (x - 0.8 - \frac{1}{4})\theta_2(t), \tag{4.21}$$

$$f_4(x,t) = F_2^-(x) + h_2(t) + (x - 0.8 - \frac{1}{4})\theta_2(t), \tag{4.22}$$

where Eqs. (4.19) and (4.20) represent the lower and upper shape functions for particle 1 respectively, while Eqs. (4.21) and (4.22) represent the upper and lower shape functions for particle 2 respectively.

In addition, particle 1 has its leading edge at $x = 0$ and its trailing edge at $x = 1$, thus having unit length, whereas particle 2 has length $\frac{1}{2}$ with its leading and trailing edges being at $x = 0.8$ and $x = 1.3$ in turn. The respective centres of mass are located at the halfway positions, namely $x = 0.5$ and $x = 1.05$. We also define our particles to be elliptically shaped. Thus here we define the particle shape functions as

$$F_1^+(x) = \alpha_1 + x^{\frac{1}{2}}(1-x)^{\frac{1}{2}}\beta_1 \tag{4.23}$$

$$F_1^-(x) = \alpha_1 - x^{\frac{1}{2}}(1-x)^{\frac{1}{2}}\beta_1 \tag{4.24}$$

$$F_2^+(x) = \alpha_2 + (x-0.8)^{\frac{1}{2}}(1.3-x)^{\frac{1}{2}}\beta_2 \tag{4.25}$$

$$F_2^-(x) = \alpha_2 - (x-0.8)^{\frac{1}{2}}(1.3-x)^{\frac{1}{2}}\beta_2 \tag{4.26}$$

with positive thickness constants β_1, β_2 and leading edge heights α_1 , α_2 . Typical studies described here are for (α_1 , α_2 , β_1 , β_2) equal to (0, 0, 0.1, 0.05) and initial conditions (h_1 , $\frac{dh_1}{dt}$, h_2 , $\frac{dh_2}{dt}$)(0) equal to (0.7, 0, 0.4, 0). During the course of the study, we tested many different values of initial angles and angular velocities but among them interesting values were found to be $\theta_1(0) = -0.1$, $\theta_2(0) = 0.1$ with $\frac{d\theta_1}{dt} = -1$ and $\frac{d\theta_2}{dt} = 1$. We found that with such initial conditions, the collision can occur not only in a finite time, but also neither too quickly nor too slowly. We also set the moment of inertia of particle 1 to be $I_1 = 0.25M_1$ and particle 2 to be $I_2 = 0.1M_2$.

In the following figures which show numerical solutions we plot three examples (1)-(3) with different mass values as described below.

(1) We set $M_1 = 1$ and $M_2 = 1$

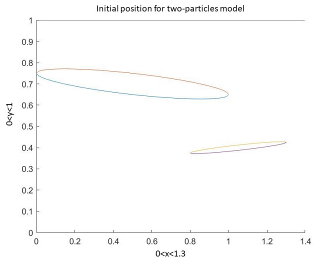

Figure 4.4: t=0

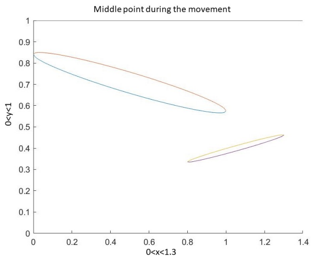

Figure 4.5: t=0.17

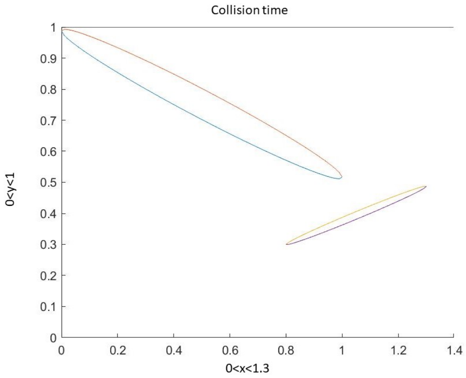

Figure 4.6: t=0.33

Figure 4.4 is the initial starting point of the whole system. Figure 4.5 shows in a sense the middle stage of the whole movement. Figure 4.6 is at the collision time where particle 1 impacts upon the upper wall. As we can see from the graph, the particle 1 moves upwards and rotates clockwise. The height of the centre of mass for particle 2 remains almost constant and its motion is almost only a rotation, slightly upward and anticlockwise. In order to make a clear contrast with this group, we next took two extreme values and tested them.

(2) We set $M_1 = 16$ and $M_2 = 1$ and keep other values the same as in example (1).

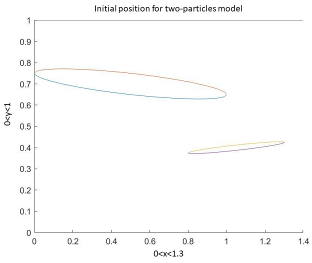

Figure 4.7: t=0

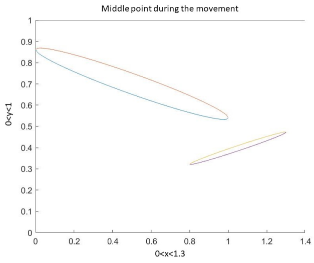

Figure 4.8: t=0.23

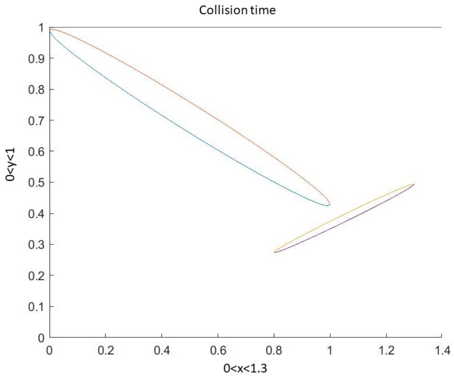

Figure 4.9: t=0.46

Here Fig. 4.7 is the initial starting point of the whole system, Fig. 4.8 is the middle stage of the evolution and Fig. 4.9 is essentially at the collision time. Despite the increased mass of particle 1 in example (2) we have almost the same motion as in example (1) except that the collision happens somewhat later than in example (1).

(3)We set $M_1 = 1$ and $M_2 = 16$ and keep other values same as for example (1)

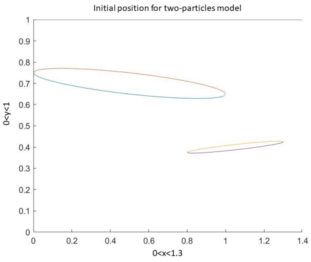

Figure 4.10: t=0

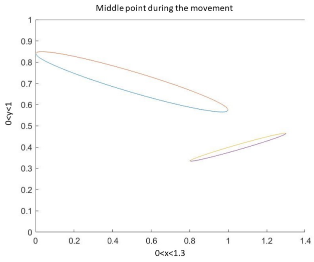

Figure 4.11: t=0.23

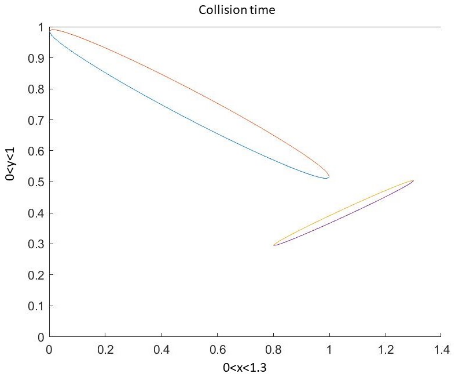

Figure 4.12: t=0.46

Again Fig. 4.10 is the initial starting point of the whole system. Figure 4.11 is the middle stage of the whole movement. Figure 4.12 is at the collision time. We have almost the same motion as in example (1). From the graphs we notice that there is a tiny difference between examples (1) and (3) (and likewise between examples (1) and (2)). This might well be caused by the different mass of particle 2. With larger mass and moment of inertia, particle 2 is harder to stop in a sense; its motion is virtually ballistic. In particular the displacement of particle 2 in example (3) is larger than that in example (1).

The height and theta functions for these three examples are presented in Figs. 4.13 and 4.14 .

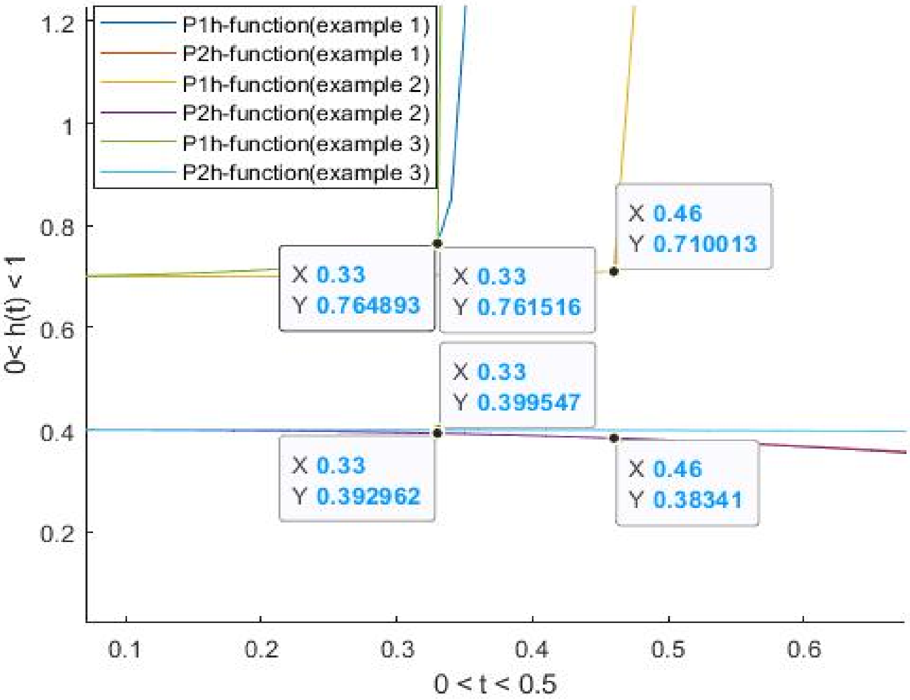

Figure 4.13: Height functions for the two-particle model in three examples

Figure 4.13 gives a graph showing the height trajectories of each case. The top three lines represent the trajectories for particle 1 in these three examples and the bottom three lines represent the trajectories for particle 2. From the sudden change of the height functions for particle 1 we can read that the collision happened between particle 1 and the top wall. That is, the fluid gap there closed at a finite time, after which the results are unphysical. Similarly, we plot the theta functions for particles in these three cases in Fig. 4.14.

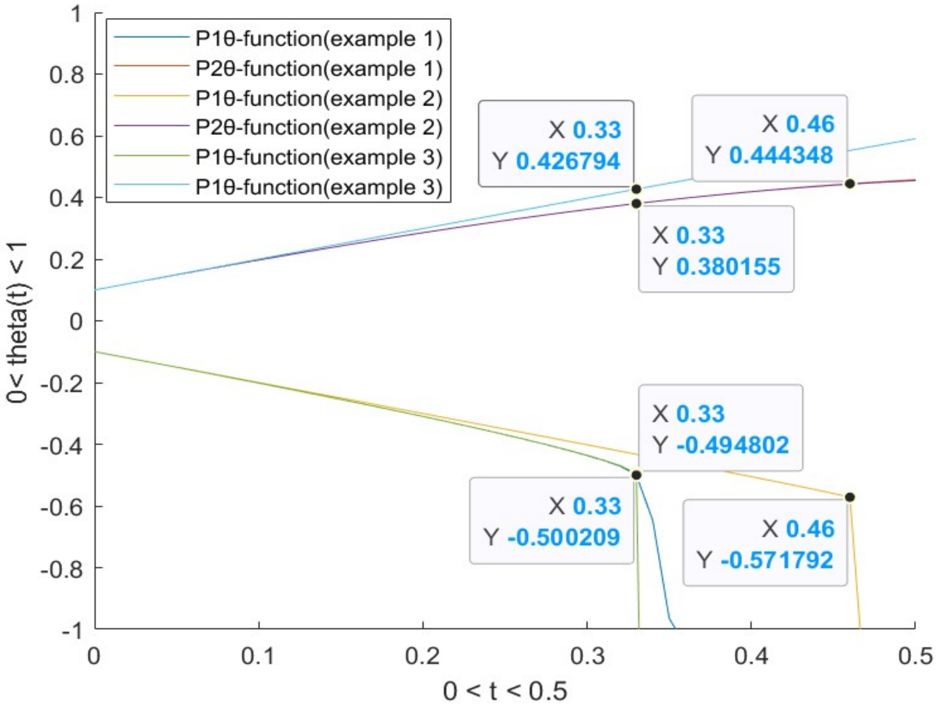

Figure 4.14: θ functions for the two-particle model in three examples.

Figure 4.14 presents the θ trajectories of each case. In contrast to the height trajectory, the bottom three lines represent the θ trajectories for particle 1 and the top three lines represent the θ trajectories for particle 2. Once again the collision time is indicated by the rapid turning point in the results.

Analysis provides some insight here. When M_1 and I_1 are large the suggestion is that, to leading order, the equations for particle 1 become simply

$$M_1 \frac{d^2 h_1}{dt^2} = 0, I_1 \frac{d^2 \theta_1}{dt^2} = 0, \tag{4.27}$$

for times t of order unity. Hence

$$h_1(t) = h_1(0), \theta_1(t) = \theta_1(0) + \theta_1'(0)t, \tag{4.28}$$

for all such t. In our model we can regard $M = 16$ as large enough to use the above analysis. Thus for the case of $M_1 = 16$ and $M_2 = 1$, the asymptotic analysis shows that particle 1 is free to rotate about its centre of mass $x = \frac{1}{2}$ at a constant rotation rate (constant angular velocity) which is -1, from the initial conditions. In effect the centre of mass of particle 1 stays still. Hence the leading edge rises uniformly and the trailing edge falls uniformly. (Particle 1 is in essence independent of particle 2 in this extreme.) However, particle 1 is long compared with particle 2 and so the leading and trailing edges of particle 1 appear to be displaced by large amounts compared with the movement of the smaller particle 2. For the $M_1 = 1$ and $M_2 = 16$ case, similarly, the leading and trailing edges of particle 2 move up or down uniformly and its centre of mass effectively stays still, in line with the asymptotic behaviour

$$h_2(t) = h_2(0), \theta_2(t) = \theta_2(0) + \theta_2'(0)t, \tag{4.29}$$

for t of order unity. However, particle 2 is the shorter particle and so its displacement appears smaller in the results.

The analytical trends Eqs. (4.28) and (4.29) appear to agree with those of the numerical solutions in Figs. 4.4-4.14. The analysis behind forms Eqs. (4.28) and (4.29) also suggests repeating the numerical study of case (3) but with the initial rotation $\theta_2'(0)$ increased to 4 and the initial vertical distances between the centres of mass decreased, in which case particle 2 might be expected to collide with particle 1 before any other collision can occur. Thus an additional example (4) is examined next.

(4) We set $\theta_2'(0) = 4$ and $h_1(0) = 0.5$ and keep other values the same as for example (3). The result is given in Fig. 4.15 and 4.16 .

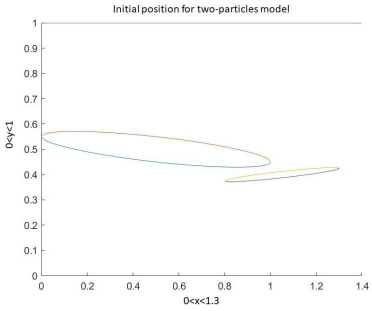

Figure 4.15: t=0

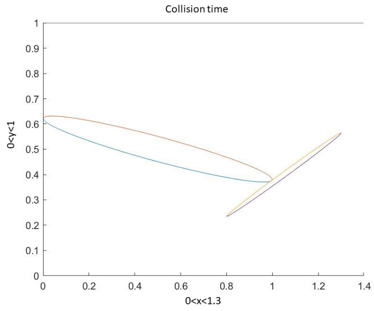

Figure 4.16: t=0.14

The finding in case (4) is that, whereas in the earlier cases the gap between the two particles is too large to let them collide with each other (before hitting a wall), now a collision can occur between the particles due to the change of initial height of particle 1 from 0.7 to 0.5 and the enlarged initial rotation of particle 2. A consequent body-to-body collision time of about $t = 0.14$ is seen to be encountered.

It is felt that the examples (1)-(4) as described above indicate the two types of impact phenomena likely to be present in the two-body fluid/body interaction problem in a channel. The types are body-wall and body-body impacts. The examples also suggest that further analysis on parametric influences could be especially fruitful. It is to be expected that many other specific cases lead potentially to the occurrence of the two types of impact above.

4.5 Further discussion

The present work points immediately to a number of useful follow-up studies and also to addressing certain difficult issues of combined fluid and solid mechanics.

One natural follow-on is to extend the understanding to the case of many bodies being present in the channel. This has only been done in the aligned scenario of [11]. In the more general non-aligned setting we can begin by creating a model for three free particles. Extending the model of the previous sections to three bodies leads to the interactive solution structure displayed in Fig. 4.17. The figure gives one example of how the three leading edge positions and the three trailing edge positions of the bodies can overlap but in all examples there must be three short-scale Euler zones and three Kutta conditions to apply, a feature which guides the subsequent working. In this example eight separate long-scale regions are present as shown in the figure.

The governing equations in the eight regions are analogous, thus yielding

$$u_n H_n = d_n (constants), \tag{4.30}$$

$$p_n + \frac{1}{2}\frac{d_n^2}{H_n^2} = \frac{1}{2}, \tag{4.31}$$

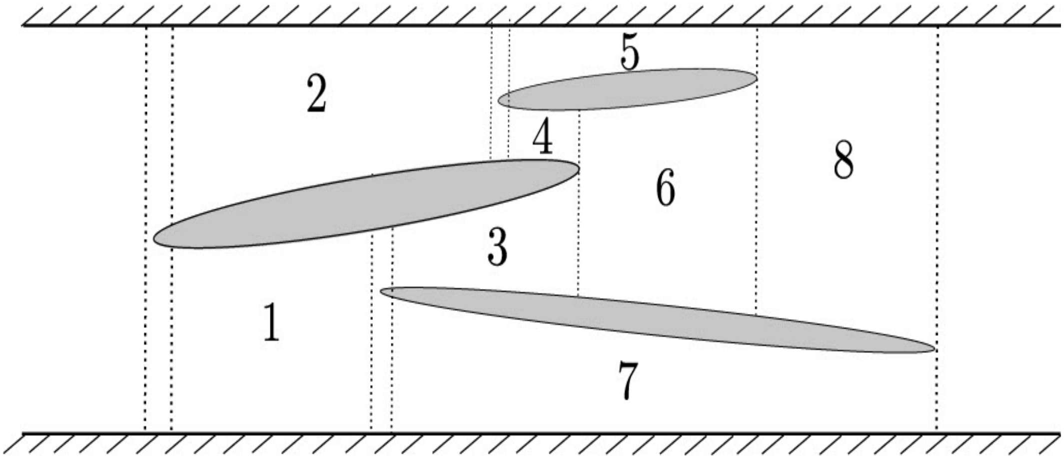

Figure 4.17: Sketch of the three-body problem and its solution structure.

for $n = 1-8$ where the gap widths $H_n(x,t)$ are defined by differences between adjacent body positions or between a body position and the adjacent wall of the channel. Because of the number of leading and trailing edges the total mass fluxes then require the six relations

$$\begin{aligned} &d_1 + d_2 = 1, d_3 + d_7 = d_1, \\ &d_4 + d_5 = d_2, d_3 + d_4 = d_6, \\ &d_5 + d_6 = d_8, d_7 + d_8 = 1, \end{aligned} \tag{4.32}$$

to hold. Notably the final relation Eq. (4.32) is linearly dependent on the other relations. Further the Kutta conditions at the three trailing edges, say $x = b$, $x = c$, $x = d$ point to the equations

$$\frac{d_3^2}{H_3^2(b,t)} = \frac{d_4^2}{H_4^2(b,t)}, \tag{4.33}$$

$$\frac{d_5^2}{H_5^2(c,t)} = \frac{d_6^2}{H_6^2(c,t)}, \tag{4.34}$$

$$\frac{d_7^2}{H_7^2(d,t)} = \frac{d_8^2}{H_8^2(d,t)}, \tag{4.35}$$

in turn. The eight equations Eqs. (4.32)-(4.35) can then be solved for the eight unknowns $d_1 - d_8$ in order to provide the pressure distributions p_n . The latter act as forcing effects in the body-motion balances which are analogous with Eqs. (4.17a), (4.17b), (4.18a) and (4.18b) but extended for three bodies, i.e. involving unknown functions of time (h_1, θ_1) , (h_2, θ_2) and (h_3, θ_3) . The solution responses remain to be pursued.

Challenging issues are also involved in tackling several extra aspects of fluid/-body interactions relevant to the current area. These include in particular: different horizontal speeds of the bodies in the laboratory frame, causing slip in the body based frame and hence time-dependent overlaps; rebounds after clashes (in particular a post-collision two-particle model will be investigated in future research); the effects of viscosity, three-dimensional and surface flexibility; comparison of the predictions from unsteady and quasi-steady flow; the full influence of body shapes and wall shapes. Just as there are many parameter regimes to study, there are in addition many interesting shapes to consider. These extra issues should enable the connection with practical applications to be made firmer.

4.6 Conclusion

The two-dimensional fluid/body interaction arising when fast- moving bodies, or particles of finite size, are free to move within the fluid surrounding them has been studied. New modelling and results on the behaviour of two interacting bodies inside a channel flow have been described for an assumed inviscid fluid. The extension to more bodies has also been discussed with a view to treating arrays of non-aligned bodies in a rational manner. For the case of many bodies the role of overlap as described is notable. Thus if there are groups of bodies separated by vertical gaps, i.e. not overlapping, then the feedback between the groups is negligible even if the groups are nearby each other; the absence of significant flow separation and hence the absence of significant wakes for the present slender bodies is a substantial factor here. For the case of two overlapping bodies it has been found specifically that the initial conditions and the relative body masses and moments of inertia exert considerable influence not only on the occurrence of body-body impacts as distinct from wall-body impacts but also on the corresponding impact times. (Both the wall-body and the body-body impacts in the present context of quasi-steady fluid flow can be described locally by analyses akin to those applied in recent work [77] within the context of a boundary layer.)

The modelled interaction between fluid flow dynamics and the free movement of bodies holds over a wide range of scales, from macro- to nano-scales. Here the potential relevance to industry, aerodynamics, biomedicine and the environment seems positive. In terms of understanding the mechanics and the physical aspects, it is felt that there is far more still to be explored (on three-dimensional effects, on many-particle interactions, on non-linear and conventional instability effects for example) than has been done to date in the area. Continuing studies along the current lines are concerned with skimming, with the growth or erosion of ice on a substrate, and with tackling three-dimensional interactions as well as with attempting to accommodate many bodies as described in the previous section. The combination of physical modelling, analysis and allied computation, whether small-scale or large-scale, appears to have been beneficial in this work.

Chapter 5

Particle moving within a channel which shape changing with pressure

5.1 Introduction

In this chapter, we will create a new model for a particle moving within a channel whose shape changes with the pressure exerted on the channel walls. The model will be built on the work in chapters 2-4 concerned with quasi-inviscid fluids and fluid-body interactions, but now allowing for flexibility in one of the walls of the channel. There appears to have been no previous study of the present particular model.

Recalling from the previous research, we have already built a model in which the shape of the channel changes. In that model, however, we specified the shape of the channel. In this way, we could more easily predict the trajectory of particles and possible collisions. That model works better for situations with fixed walls such as needles or conduits. The present model may work better for the soft (flexible, see references below) wall shape channel such as a modelled blood vessel. As in our previous chapters, we can anticipate that there will be many parameters involved, a feature which may be expected to be reinforced by the parameters associated with the wall flexibility. Our intention in this chapter will be to inspect part of the new parameter space, not the whole of it.

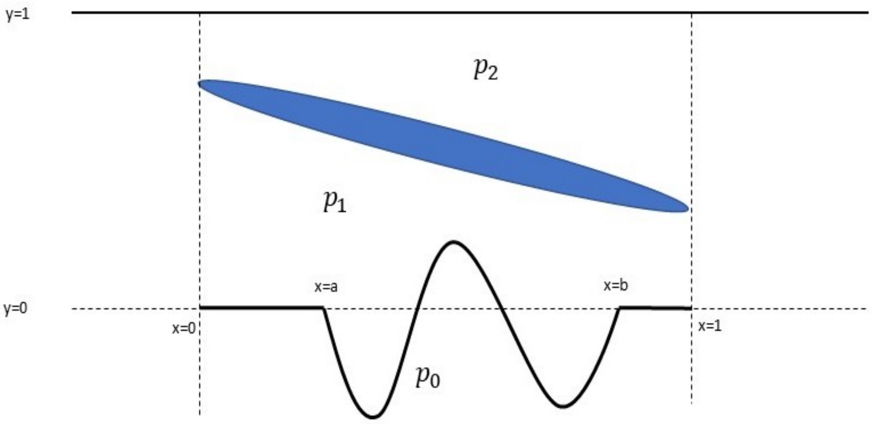

Figure 5.1: The initial position of our particle in the flexible channel shape model.

In the present model we assume that flexible parts of the channel wall could exist in the x interval of $[a,b]$. The coordinates x, y, t are defined as in earlier chapters of the thesis. Here $x=0$ and $x=1$ represent the leading edge and the trailing edge of our particle respectively. Meanwhile, we assume the channel width at $x=a$ and $x=b$ is equal and equal to 1. We note that our concern will usually be with the case where $0<a<b<1$. We assume the p_0 is the non-dimensional base (external) pressure relative to the oncoming pressure level, which is taken to be zero, p_1 is the pressure between the bottom wall and the lower edge of the particle, p_2 is the pressure between the top wall and the upper edge of the particle.

Regarding the flexible surface shape's response to fluid flow across the surface, models by [49], [45], [46], [43], and others show that the shape and flow interact via the local pressure. The main assumptions are those of the commonly used membrane-model type as in the references above, with [47] as well as [42], [78], [44], and [48] providing particularly interesting background discussions of linearly elastic materials and related aspects relevant here. We refer here to equation (2.5) in [50] as our governing equation,

$$e_1 f_{xxxx} + e_2 f_{xx} + e_3 f + e_4 f_{tt} + e_5 f_t = p - p_0. \tag{5.1}$$

In this model we assume the spike shape is $y=f(x,t)$ and the non-dimensional constant coefficients $e_1 = \frac{-B^*}{U^{*2}L^{*3}\rho^*}$, $e_2 = \frac{T_t^*}{U^{*2}L^*\rho^*}$, $e_3 = \frac{-\kappa^* L^*}{U^{*2}\rho^*}$, $e_4 = \frac{-M^*}{L^*\rho^*}$, $e_5 = \frac{C^*}{U^*\rho^*}$, with U^*, L^*, ρ^*, M^*, C^*, κ^*, T_t^* being the fluid velocity, the typical length factor, the uniform density of the incompressible fluid, the mass, the damping constant, the flexural rigidity, the spring stiffness, longitudinal tension respectively. During the test, p_0 is the dimensionless base pressure relative to the oncoming pressure level and we take p_0 zero or nonzero depending on the circumstances. For specific materials, the values of the aforementioned quantities are calculated by experimentation or tabulated. Importantly, according to the physical quantities contained in the above variables we conclude $e_1 < 0$, $e_2 > 0$, $e_3 < 0$.

We assume for simplicity that the flexible part of the channel wall is moving with the particle. For this and other reasons we could ignore the last two terms in the left-hand-side of the equation (5.1) and rewrite the equation as below,

$$e_1 f_{xxxx} + e_2 f_{xx} + e_3 f = p_1 - p_0. \tag{5.2}$$

Here $p_1 = p$ is the internal pressure and others are the same as mentioned before.

The boundary conditions for f are

$$f = f_X = 0 \; at \; X = a, b, \tag{5.3}$$

if $X = a, b$ are assumed for the single flexible region's end points for certainty. Additionally, we still use the same body shape and motion functions as before,

$$f_p{}^{\pm}(x,t) = F^{\pm}(x) + h(t) + (x - 1/2)\theta(t). \tag{5.4}$$

We still assume $F_1^+(x) = \alpha + x^{\frac{1}{2}}(1-x)^{\frac{1}{2}}\beta$ and $F_1^-(x) = \alpha - x^{\frac{1}{2}}(1-x)^{\frac{1}{2}}\beta$ as our body shape functions representing an ellipse, where α, β are real constants and $0 < \alpha, \beta < 1$.

With all above new conditions, the whole system will be changed into,

$$f_p{}^{+}(x,t) = F^{+}(x) + h(t) + (x - 1/2)\theta(t). \tag{5.5}$$

$$f_p{}^{-}(x,t) = F^{-}(x) + h(t) + (x - 1/2)\theta(t). \tag{5.6}$$

At the trailing edge we have ${f_p}^+(1,t) = {f_p}^-(1,t)$. By the contunity equations and Bernoulli relations and Kutta conditions, we have the relations below,

$$d_1 + d_2 = 1, \tag{5.7}$$

$$\frac{{d_1}^2}{{H_1}^2} = \frac{{d_2}^2}{{H_2}^2}, \tag{5.8}$$

$$p_1 = \frac{1}{2}(1 - {u_1}^2),\ p_2 = \frac{1}{2}(1 - {u_2}^2), \tag{5.9}$$

where $d_1 = u_1 H_1$, $d_2 = u_2 H_2$, $H_1 = {f_p}^- - f$, $H_2 = 1 - {f_p}^+$. Same as before, we still use the Newton's motion functions for the rigid body as the governing equations,

$$M\frac{d^2h}{dt^2} = \int (p_1(x,t) - p_2(x,t))dx, \tag{5.10a}$$

$$I\frac{d^2\theta}{dt^2} = \int (x - C)(p_1(x,t) - p_2(x,t))dx, \tag{5.10b}$$

where C represents the center of mass of the particle.

In this section we have created a new model to describe particle motion. In the next section, we will give the initial conditions and test the model. During the test, we will use almost the same motion functions as before. At the same time, we will seek to verify the accuracy of the model.

5.2 Model creation

For the first test, we randomly choose $e_1 = -1$, $e_2 = 1$, $e_3 = -1$ and we assume the external pressure $p_0 = 0$. At the same time, we assume the flexible part of the bottom wall is from $x = 0.2$ (point $x = a$) to $x = 0.7$ (point $x = b$), that is, with 0.2 corresponding to point a and 0.7 corresponding to point b. With the previous and above conditions, we can take the initial test as below,

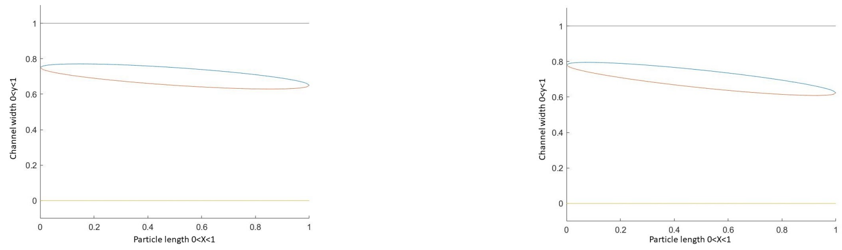

(a) Particle position at t=0 **(b)** Particle position at t=0.13

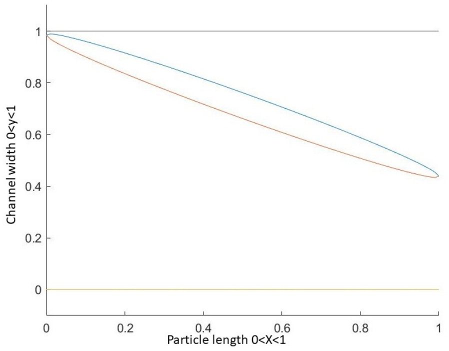

(c) Particle position at t=0.26

Figure 5.2: Initial test with $e_1 = -1$, $e_2 = 1$, $e_3 = -1$, $p_0 = 0$

From the figure 5.2, we can see that the particle trajectory is not much different from the previous tests, which had no flexibility of the wall, and indeed the shape of the lower wall is not significantly changed. It is changed a small amount, however. We plot the graph for the bottom wall to better present the changes.

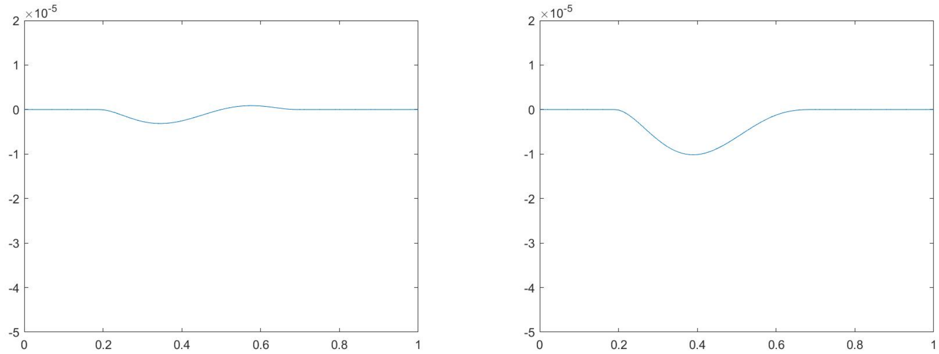

(a) Bottom wall shape at t=0 **(b)** Bottom wall shape at t=0.13

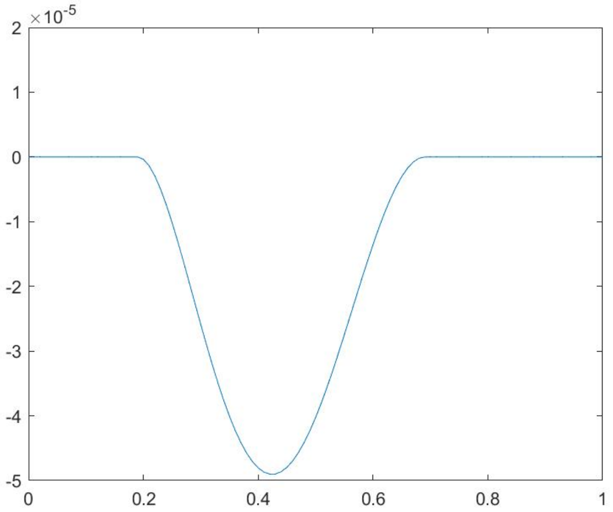

(c) Bottom wall shape at t=0.26

Figure 5.3: Initial test for bottom wall shape

From the figure 5.3, we know that the typical variation of the bottom wall is too small to have a significant effect on our particle motion. Responding to this, we increase the external pressure p_0 and the results are shown in figure 5.4,

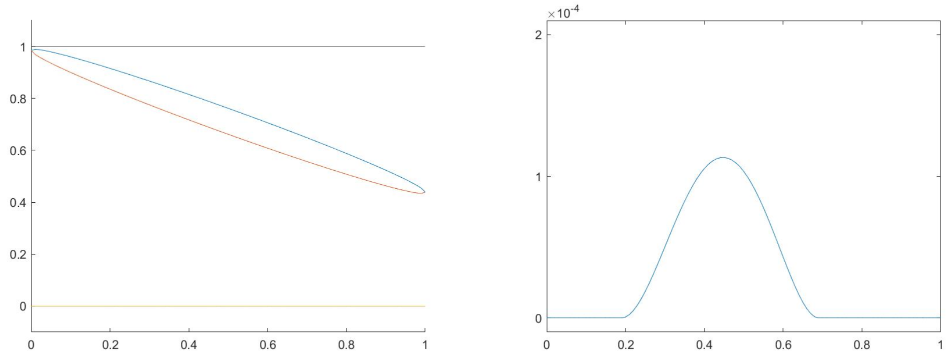

(a) Particle position at t=0.26 ($p_0 = 1$) **(b)** Bottom wall shape at t=0.26 ($p_0 = 1$)

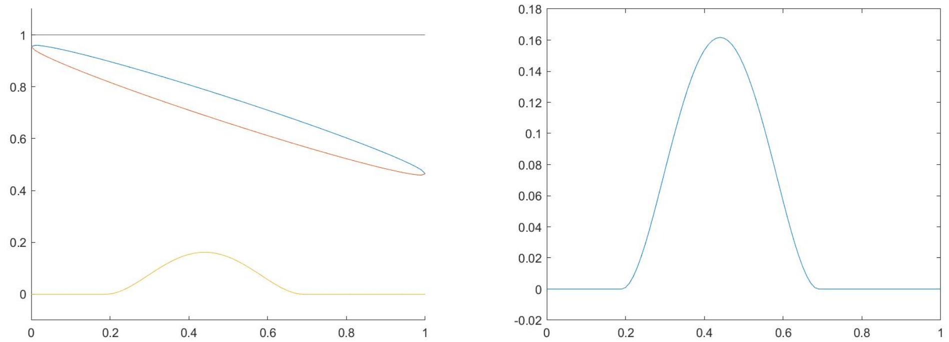

(c) Particle position at t=0.26 ($p_0 = 1000$) **(d)** Bottom wall shape at t=0.26 ($p_0 = 1000$)

Figure 5.4: Particle collision point and bottom wall shape with different external pressure

Referring to figure 5.4b, we notice the shape changing with order of 10^{-4}. If we increase the wall effect 1000 times, there could be a noticeable change on the bottom wall. Thus we change the external pressure from 0 to 1000. See figure 5.4d which shows a much more substantial response.

To prove we have the correct bottom wall shape, we examine the wall equation more closely. For example, recalling from the previous 4^{th} order differential equation (5.2) with $e_1 = -1$, $e_2 = 1$, $e_3 = -1$, we address

$$-f_{xxxx} + f_{xx} - f = p_1 - p_0. \tag{5.11}$$

When we have a large value of p_0, for example in the last test, $p_0 = 1000$, the right-hand-side of the equation will be dominated by p_0 and the left-hand-side of the equation will be dominated by f_{xxxx} as an approximation. Thus, roughly, we can treat the equation as

$$f_{xxxx} = p_0. \tag{5.12}$$

After solving equation (5.12), we have the approximate answer as below,

$$f(x) = \frac{p_0}{4!}(x-a)^4 + A(x-a)^3 + B(x-a)^2 + C(x-a) + D, \tag{5.13}$$

where the constants A, B, C, D need to be solved. Recalling from the initial conditions

$$f(a) = 0, f'(a) = 0. \tag{5.14a}$$

$$f(b) = 0, f'(b) = 0. \tag{5.14b}$$

We can have the relation below,

$$0 = \frac{p_0}{4!}(b-a)^4 + A(b-a)^3 + B(b-a)^2. \tag{5.15a}$$

$$0 = \frac{p_0}{3!}(b-a)^3 + 3A(b-a)^2 + 2B(b-a). \tag{5.15b}$$

In our assumption, $b-a$ is a real nonzero number. Therefore, we can divide $(b-a)^2$ on both sides of equation (5.15a) and divide $(b-a)$ on both sides of equation (5.15b). Hence, we obtain 2 new equations

$$0 = \frac{p_0}{4!}(b-a)^2 + A(b-a) + B. \tag{5.16a}$$

$$0 = \frac{p_0}{3!}(b-a)^2 + 3A(b-a) + 2B. \tag{5.16b}$$

After solving the above equation pair, we have $A = -\frac{p_0}{12}(b-a)$, $B = \frac{p_0}{24}(b-a)^2$. We substitute above values A, B, C, D into equation (5.13) to find,

$$f(x) = \frac{p_0}{4!}(x-a)^4 - \frac{p_0}{12}(b-a)(x-a)^3 + \frac{p_0}{24}(b-a)^2(x-a)^2. \tag{5.17}$$

Then we may substitute any value of x to check the accuracy. For instance, we choose $x = \frac{(a+b)}{2}$, which gives,

$$f(x) = \frac{p_0}{4!}(x-a)^4 - \frac{p_0}{12}(b-a)(x-a)^3 + \frac{p_0}{24}(b-a)^2(x-a)^2. \tag{5.18}$$

After substitution we have $f((a+b)/2) = 0.16276$, while the numerical finite-difference value is 0.16171. The error is about 0.001 which, can be accepted in our model. Thus, we are going to use this model in the future tests.

In this part, we checked to find the appropriate external pressure ($p_0 = 1000$) to make an observable change in our model, and we verified the accuracy of the bottom wall shape. In the next chapter we will focus on varying the particle height and internal pressures to examine the collisions between the particle and the bottom wall.

5.3 Varying the external and internal pressure and particle height

5.3.1 Vary the external and internal pressure

In the previous section, we have already found an appropriate external pressure. Now we are more interested in possible collisions. Thus, we change the external pressure and rescale the bottom wall shape governing equation. After rescaling, our bottom wall shape governing equation (5.2) becomes,

$$e_1^* f_{xxxx}^* + e_2^* f_{xx}^* + e_3^* f^* = c_1^*(p_1 - p_0^*). \tag{5.19}$$

Because when we use the original equations for the calculation, we will always get a high spike on the flexible part, this restricts our particle's movement which means the particle will collide with the bottom wall very quickly. That is why we need a constant c_1^* on the right hand side of the equation (5.19). Here $e_1^* = \frac{e_1}{c_2}$, $e_2^* = \frac{e_2}{c_2}$, $e_3^* = \frac{e_3}{c_2}$, $c_1^* = \frac{c_1}{c_2}$. The external pressure now becomes $p_0^* = \frac{p_0}{c_1^*}$. With the above rescaling equation we set $e_1^* = -0.001$, $e_2^* = 0.001$, $e_3^* = -0.001$, and $c_1^* = 0.001$. To tell the difference between $p_0 = 1$ and $p_0 = 2$, we plot the new graphs with the equation (5.19) and use $\alpha = 0.7$, $\beta = 0.1$, $c = 0.5$, $\theta(0) = -0.1$, $h(0) = 0$, $\theta'(0) = 0$, $h'(0) = 0$ as the initial conditions. We also set $a = 0.2$ to $b = 0.7$ as the part of the bottom wall that is flexible. First we plot the graphs with $p_0 = 1$ and the results are shown as below in figure 5.5,

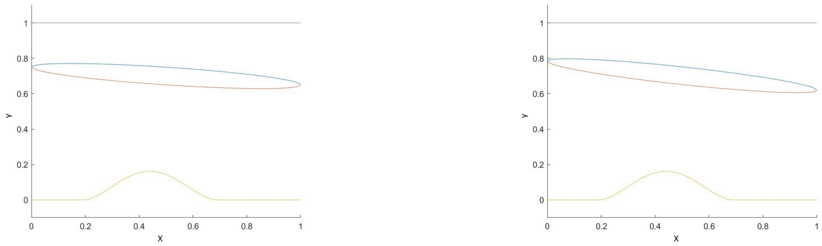

(a) Particle position at t=0 ($p_0 = 1$)

(b) Particle position at t=0.13 ($p_0 = 1$)

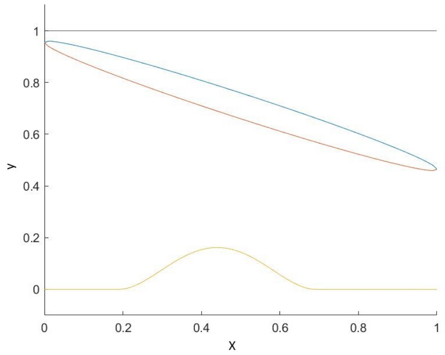

(c) Particle position at t=0.26 ($p_0 = 1$)

Figure 5.5: Particle movement with external pressure $p_0 = 1$

Figure 5.5 are some results with $p_0 = 1$. We put this set of test here as a comparison. Next we keep all the initial conditions the same as before but change to $p_0 = 2$; the results are shown as below in figure 5.6,

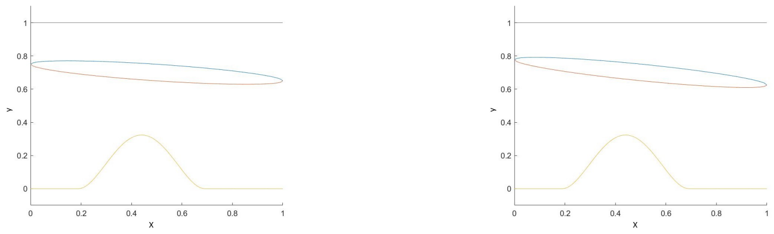

(a) Particle position at t=0 ($p_0 = 2$) **(b)** Particle position at t=0.13 ($p_0 = 2$)

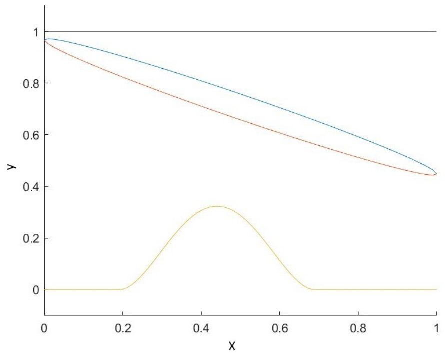

(c) Particle position at t=0.26 ($p_0 = 2$)

Figure 5.6: Particle movement with external pressure $p_0 = 2$

As we can see from the figures 5.5 and 5.6, the height for the bottom flexible part varies. Obviously, figure 5.6 suggests that it is easier to make a collision happen. Thus we are going to use $p_0 = 2$ in our subsequent tests.

In addition, we recall the research interest in avoiding collision between the particle and the channel walls. Because the pressure p_1 above the flexible part is always negative for a the smaller gap, increasing the parameter c_1 is a possible way to drag the particle downwards or reduce the particle's upwards velocity. On the other hand, this is a delicate method because the negative pressure will also tend to increase the height of the bottom flexible part. With these concerns, we undertook 4 different tests ($c_1^* = 0.001$, $c_1^* = 0.1$, $c_1^* = 0.3$, $c_1^* = 0.5$). We use the same initial conditions mentioned before along with $p_0 = 2$. The only difference is that different values for c_1^* are taken. The results are shown as below.

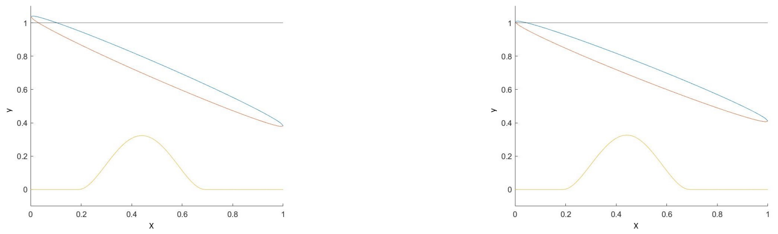

(a) Particle position at t=0.29 ($c_1^* = 0.001$) **(b)** Particle position at t=0.29 ($c_1^* = 0.1$)

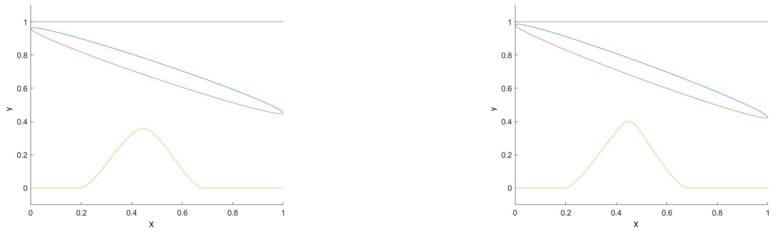

(c) Particle position at t=0.30 ($c_1^* = 0.3$) **(d)** Particle position at t=0.31 ($c_1^* = 0.5$)

Figure 5.7: Particle collision point with different values of c_1^*

From the figure 5.7, the results are exactly the same as our conjectures in the previous paragraph. In the subsequent tests we would like to know all these parameters' influences on our particle, including the different initial heights of the particle. For this we need to keep some space for the particle movement. As a consequence, $c_1^* = 0.5$ seems a reasonable value for the tests.

5.3.2 Vary particle height

In the section 5.3.1, we simulated numerically the motion of the particle and the flexible lower wall, including variations of the internal and external pressure. We found that using an external pressure $p_0 = 2$ is a helpful condition to let the lower flexible wall produce a significant change. Thus, in this section, we aim to keep this condition. Besides this, we only test 1 case where the particle collides with the top wall. Hence, in this section, we work to seek numerically some other possible collisions.

(1) h(0)=0.5 case

For the numerical analyses in the last section, we kept $h(0) = 0.7$ and varied the parameter multiplying p_1 which is c_1^* to change the internal pressure and vary p_0 to change the external pressure. In the present part, we add some variation for the initial height as well. In order to better observe the influence of initial height, the value $c_1^* = 0.5$ was selected as the initial control group (in effect) and results are shown below.

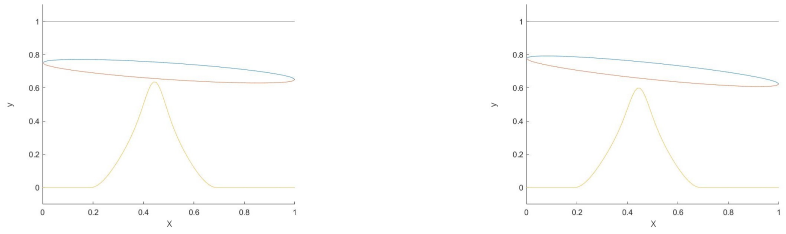

(a) Particle position at t=0 ($h(0) = 0.7$) **(b)** Particle position at t=0.15 ($h(0) = 0.7$)

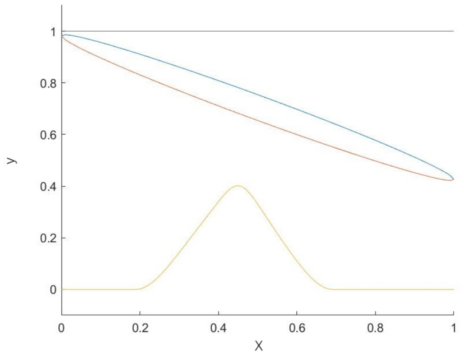

(c) Particle position at t=0.3 ($h(0) = 0.7$)

Figure 5.8: Particle position with $h(0) = 0.7$

Just for reminding, we use $\alpha = 0.7$, $\beta = 0.1$, $c = 0.5$, $M = 2$, $I = 0.01$, $\theta(0) = -0.1$, $\theta'(0) = 0$, $h'(0) = 0$, $p_0 = 2$ as the initial conditions during the test and $h(0)$ needs to be set in each test. Besides, figure 5.8a shows the starting point of the test. By the way, the particle and wall are very close together but do not collide.

To compare with these results, we change $h(0) = 0.7$ to $h(0) = 0.5$ and we notice, under the same conditions, the bottom flexible wall cannot cross the particle, even though it appears to do so. This is clearly not a reasonable model and it is physically incorrect. Therefore, as we mentioned before, the value for p_1 is negative. Thus reducing c_1^* could reduce the drag force to the bottom flexible part. Thus this should be a useful way to make the model reasonable. The process of reducing c_1^* from 0.5 to 0.05 is shown in figure 5.9.

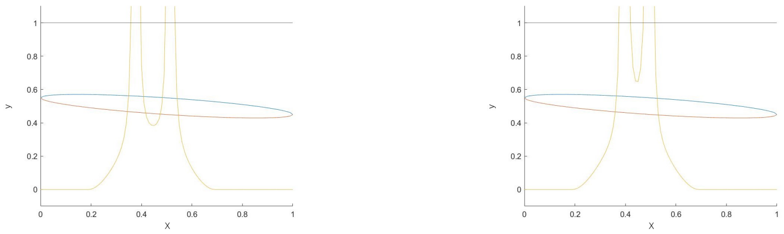

(a) Particle position at t=0 ($c_1^* = 0.5$) **(b)** Particle position at t=0 ($c_1^* = 0.3$)

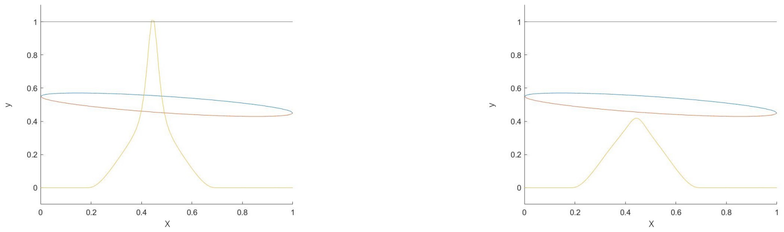

(c) Particle position at t=0 ($c_1^* = 0.1$) **(d)** Particle position at t=0 ($c_1^* = 0.05$)

Figure 5.9: Tests of different values of c_1^* influence to the model with h(0)=0.5

After testing the results as in figure 5.9, we find when the value for c_1^* reduces to 0.05, the particle is not crossed by the bottom flexible part at the initial position. Then we show some middle steps and collision point of this case as in figure 5.10.

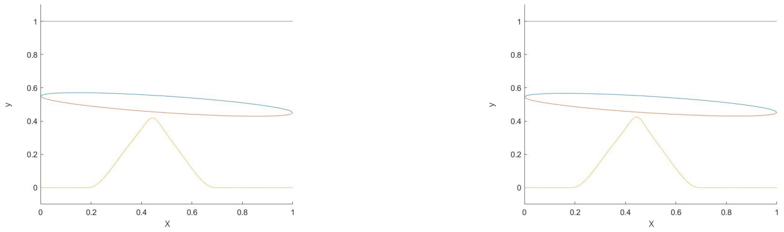

(a) Particle position at t=0 ($h(0) = 0.5,\ c_1^* = 0.05$)

(b) Particle position at t=0.07 ($h(0) = 0.5,\ c_1^* = 0.05$)

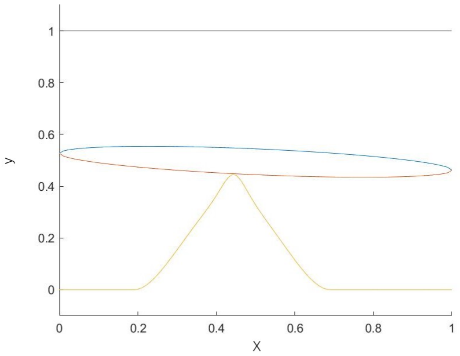

(c) Particle position at t=0.14 ($h(0) = 0.5,\ c_1^* = 0.05$)

Figure 5.10: Particle motion with $h(0) = 0.5,\ c_1^* = 0.05$

From the figure 5.10, we notice the particle and the bottom wall start close together, but, same as before, they did not collide. After a few steps, they become even closer to each other until the collision occurs. Although let the particle travel time in the channel reach t=0.14 is an encouraging result, we still want longer travel time to make sure the model is a sensible model. Thus, given the previous results, we further reduce c_1^* to $c_1^* = 0.01$ and show the results below,

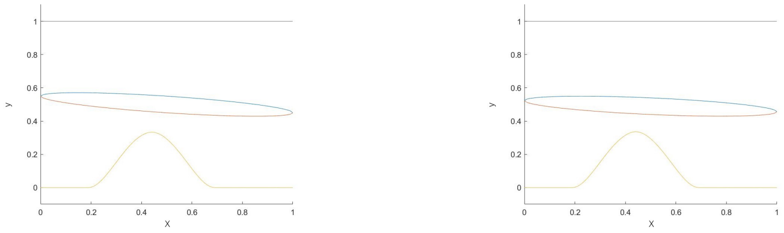

(a) Particle position at t=0 ($h(0) = 0.5,\ c_1^* = 0.01$)

(b) Particle position at t=0.24 ($h(0) = 0.5,\ c_1^* = 0.01$)

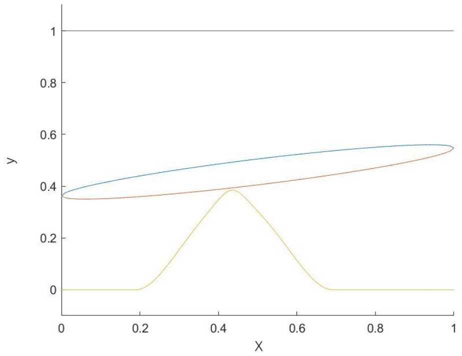

(c) Particle position at t=0.45 ($h(0) = 0.5,\ c_1^* = 0.01$)

Figure 5.11: Particle motion with $h(0) = 0.5,\ c_1^* = 0.01$

From the graphs in figure 5.11 we can see the particle can move between the channel walls for about 0.45 unit time. Since c_1^* only affects the flexible wall on the lower side, it can be concluded via the tests that, under the same conditions, smaller c_1^* will make the particle move for a longer time. We assume that c_1^* is always a non-negative number ($c_1^* \geq 0$), that is, the existence of c_1^* will not cause downward bending of the flexible wall on the lower side. In this way, there is a situation in our model that can make the particle move for the longest time, that is, let c_1^* approach zero indefinitely. At this point, the function and shape of the lower wall with $e_1^* = -0.001$, $e_2^* = 0.001$, $e_3^* = -0.001$ are shown in figure 5.12.

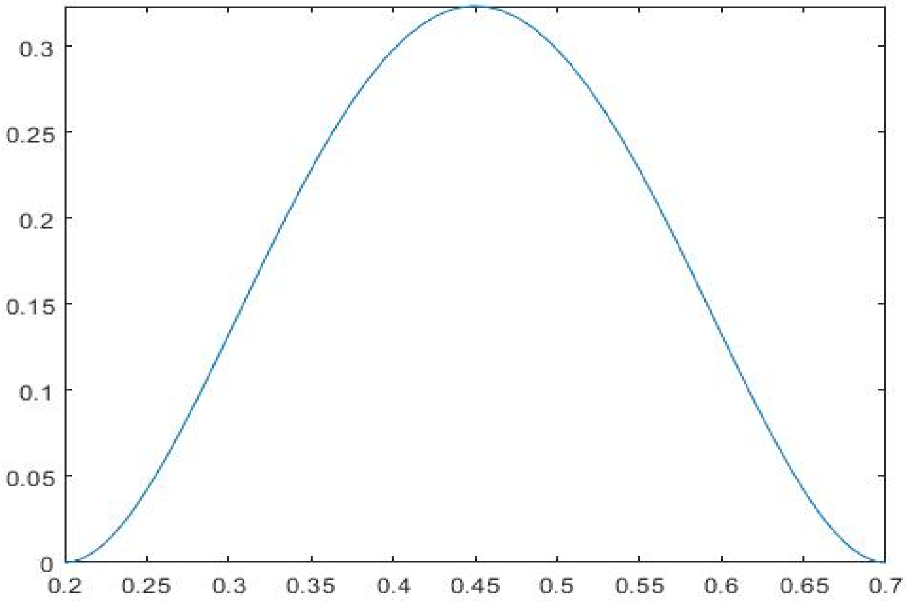

Figure 5.12: Bottom wall shape with $c_1^* = 0$, $p_0 = 2$

From these cases, we can draw a conclusion that inner pressure with parameter $c_1^* = 0.05$ is perhaps apt to keep the particle moving in the channel. At the same time, we found that smaller c_1^* leads to longer translational time for the particle.

(2)h(0)=0.3 case

Previously, we have drawn some conclusion about the $h(0) = 0.5$ case. In this part, we prefer a lower starting point $h(0) = 0.3$. As in the previous tests, we use $h(0) = 0.3$, $h'(0) = 0$, $\theta(0) = -0.1$, with $e_1^* = -0.001$, $e_2^* = 0.001$, $e_3^* = -0.001$, $c_1^* = 0.5$ as the initial conditions but we vary $p_0 = 0.5$ to find a ”reasonable” initial position. The reason why we use $p_0 = 0.5$ as the initial condition is because when we use a larger pressure (for example $p_0 = 2$), no matter what value of c_1^* we choose, we cannot find physical results. After few tests, we decide to use $p_0 = 0.5$ as the initial condition to give us a ”reasonable” start and the results are shown below.

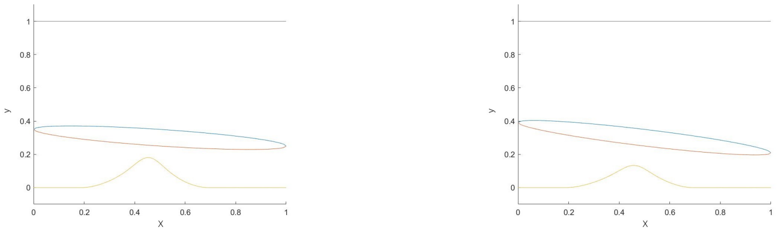

(a) Particle position at t=0 ($p_0 = 0.5$) **(b)** Particle position at t=0.2 ($p_0 = 0.5$)

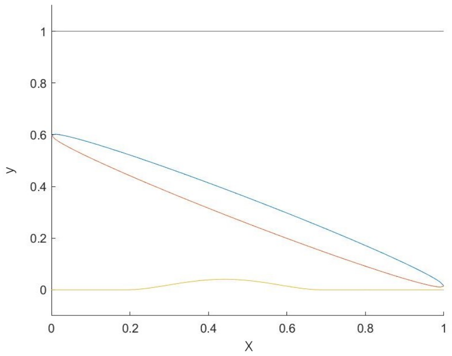

(c) Particle position at t=0.41 ($p_0 = 0.5$)

Figure 5.13: Particle motion with $p_0 = 0.5$

Figure 5.13 shows the collision happens between the bottom wall (non-flexible part) and the particle's trailing edge.

In this section, we discussed 3 different height cases. Luckily, we found some possible ways to make the collisions happen. For instance, when $h(0) = 0.5$ with the conditions we mentioned above, if we could adjust the parameter for the inner pressure $c_1^* = 0.01$, we may find an improved solution such that the particle could move for 0.45 unit time. Furthermore, if we start with a lower position, for instance, $h(0) = 0.3$, with the conditions we mentioned earlier in this section, we found no matter how small we adjust the value for c_1^*, we could not find a reasonable initial position for our model. Therefore, we adjusted the external pressure p_0 from $p_0 = 2$ to some smaller value and we suppose there should be a solution between $p_0 = 0.5$ and $p_0 = 0.8$ to make the collision happen between the particle and the bottom flexible wall. In the following part, we would like to present a few further tests. First, we aim to find the collision for $h(0) = 0.7$ case. Besides this, we also want to test the particle with zero thickness and the bottom wall shape function without the

4th order term.

5.4 Further cases

As a reminder from the beginning of the current chapter, we should comment here that our fluid-body interaction with a flexible wall present involves a multi-parameter space. Our aim is to address certain particular aspects of that space and the effects of certain particular parameters. Additionally it is notable that inclusion of the wall equation (6.2) or (6.5) makes the overall system considerably more difficult to solve and sensitive to the values of the parameters involved.

5.4.1 Runs with initial downwards velocity

Besides the previous runs, we now add a downwards initial velocity to our particle. The reason is that with such an initial velocity, the collision should happen much easier than in the previous zero-initial-velocity cases. The present part of the study is found to reveal several interesting phenomena. Trials were carried out to derive reasonable initial conditions. and these trials led to much 'detective' work. Many details can be omitted but for openness and completeness we show several lead-up investigations below.

Firstly, we choose $c_1^* = 0.5$, $dt = 0.01$, $p_0 = 2$, $h(0) = 0.7$, $h'(0) = -0.5$, $\theta(0) = -0.1$, $\theta'(0) = 0$ and others are the same values as in section 5.3 to check whether the collision could happen. The negative value of $h'(0)$ here indicates the downward initial velocity of the particle. The results are shown in figures 5.14.

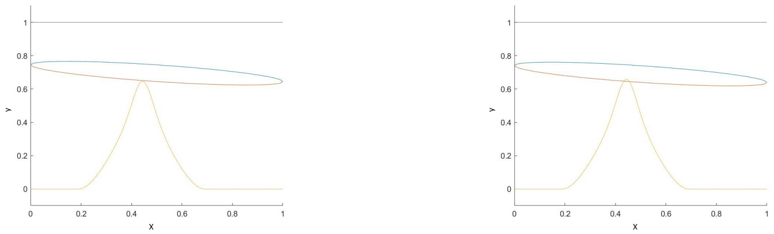

(a) Particle position at t=0 ($h'(0) = -0.5$) **(b)** Particle position at t=0.01 ($h'(0) = -0.5$)

Figure 5.14: Particle motion with $h'(0) = -0.5$

Although it is hard to see any difference in the subfigures but this is considered in the text below. Recalling the section 5.3, we found that $c_1^* = 0.5$ can cause a collision between the particle and the lower side wall, so we continued to use $c_1^* = 0.5$ in the following experiments (some tests will modify the parameters). At the same time, based on the previous test, if we set the initial height at 0.7, the particle can have enough time to move in the channel, and then we can modify the parameters later to study the particle movement trajectory and the deformation process of the lower wall in more detail. Since we care more about the relation between the particle and the lower side wall, we add an initial downward velocity and a negative angle to the particle. At the same time, in the previous test, we learned that when the external pressure is equal to 2, the lower wall can be significantly deformed, and the speed of deformation will not be too fast, which leaves us a certain operating time of the whole system. At the same time, when we set time-step equals to 0.01, we get a continuous trajectory. To sum up, we chose $c_1^* = 0.5$, $dt = 0.01$, $p_0 = 2$, $h(0) = 0.7$, $h'(0) = -0.5$, $\theta(0) = -0.1$, $\theta'(0) = 0$ and others are the same values as in 5.3 as our initial condition. But unfortunately, when we chose these as the initial variables, the lower side wall was already very close to our particle at the beginning position. And figure 5.14b shows what the system looks like after a time-step. We see that the lower side wall has passed through our particle, which is against the original intention of our research, so we need to modify the parameters and retry the test.

Next, given the graphs above and previous results, if the particle moves down slowly enough to give the lower wall enough time to move down, it might keep the particle moving through the channel longer. Thus, we try to reduce the initial velocity from $h'(0) = -0.5$ to $h'(0) = -0.3$ and the results are shown below in figure 5.15.

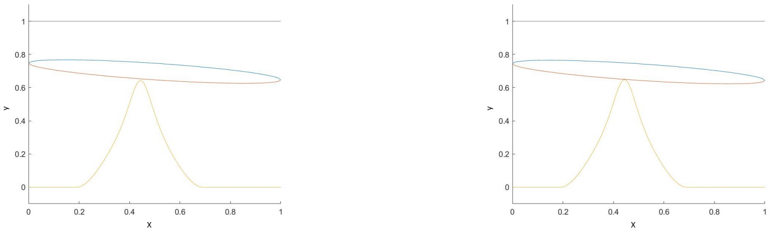

(a) Particle position at t=0 ($h'(0) = -0.3$) **(b)** Particle position at t=0.01 ($h'(0) = -0.3$)

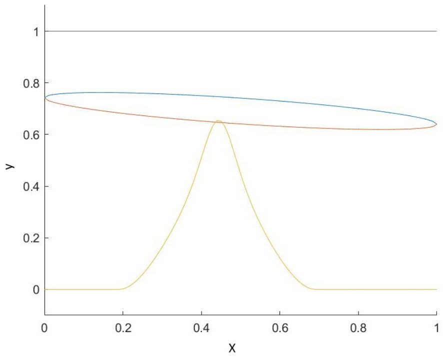

(c) Particle position at t=0.02 ($h'(0) = -0.3$)

Figure 5.15: Particle motion with $h'(0) = -0.3$

In the test with $h'(0) = -0.5$ as the initial velocity, we found that the particle had almost no time to move in the tube, which is not consistent with the results we wanted. We can extend the movement time of the particle in the pipe by modifying the parameters. First, we chose to reduce the initial downward velocity of the particle and show the results in figure 5.15. We can see from the figure that the motion time of the particle increases from less than 0.01-unit time in $h'(0) = -0.5$ test to less than 0.02-unit time in $h'(0) = -0.3$ test. Prove that we are modifying the parameters in the right direction. Reducing the initial velocity allows the particle to travel in the tube for a longer time.

With this encouraging result, we further reduce the value from $h'(0) = -0.3$ to $h'(0) = -0.1$ and the results are shown in figure 5.16.

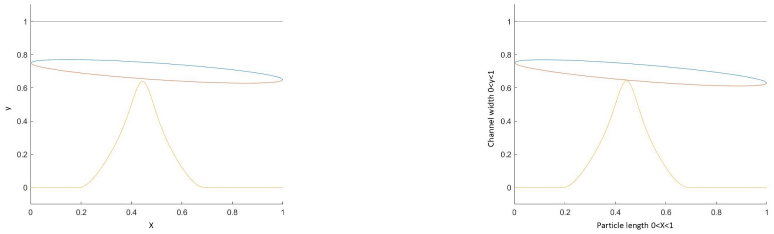

(a) Particle position at t=0 ($h'(0) = -0.1$) **(b)** Particle position at t=0.1 ($h'(0) = -0.1$)

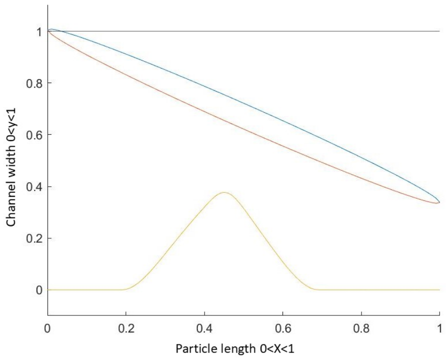

(c) Particle position at t=0.33 ($h'(0) = -0.1$)

Figure 5.16: Particle motion with $h'(0) = -0.1$

It is not difficult to see that after we modify the initial velocity to $h'(0) = -0.1$, our particle has a slow enough initial falling velocity for the lower wall to complete the ascending and then descending process. During the process we found that the running time of the particle in the channel is greatly increased, because the particle has a very close but non-collision trajectory with the lower wall during the movement. This situation can be understood as approaching the boundary condition, if the initial speed of the particle moving downward is increased, the particle will collide with the lower side wall, resulting in the particle cannot continue to move, and the test will stop. We can treat this kind of condition as the “optimal solution”. The minimum gap between the lower wall and the particle during the entire motion is about $4.25 * 10^{-3}$. The above run was stopped after the particle collided with the upper wall.

5.4.2 Runs with initial downwards velocity and zero thickness

Previously, we made simulation runs of a single particle with thickness and we almost obtained an optimal solution for a single particle movement within a part-flexible channel. In the previous chapter, we have studied a lot of similar models. Since zero thickness is almost impossible in a real-life problem, therefore we only do one case for this model. In this case, we use $h(0) = 0.7$, $h'(0) = -0.3, \theta(0) = -0.1$, equation (5.19) with $e_1^* = -0.001$, $e_2^* = 0.001$, $e_3^* = -0.001$, $c_1^* = 0.5$, $p_0 = 2$, $dt = 0.01$ as our initial conditions. We also choose zero-thickness as our test objective and show the results in figures 5.17.

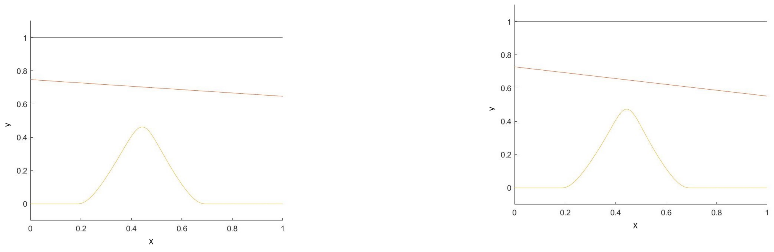

(a) Particle position at t=0 (zero-thickness)

(b) Particle position at t=0.21 (zero-thickness)

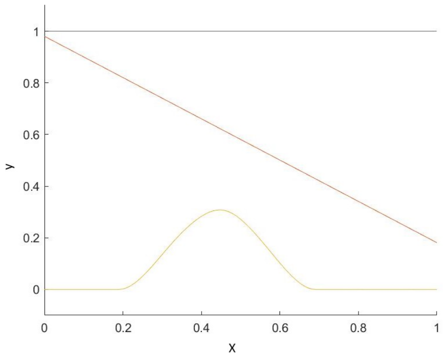

(c) Particle position at t=0.42 (zero-thickness)

Figure 5.17: Particle motion with $h'(0) = -0.3$

It is clear from the figures that during the whole process of motion, the zero-thickness particle remains significantly far away from the lower wall. Because of this, a clash with the flexible wall is not the limitation for the model. To optimize this model, we increase the downwards speed from h'(0)=-0.3 to h'(0)=-0.5 and show the results below. See figure 5.18.

(a) Particle position at t=0 ($h'(0) = -0.5$) **(b)** Particle position at t=0.34 ($h'(0) = -0.5$)

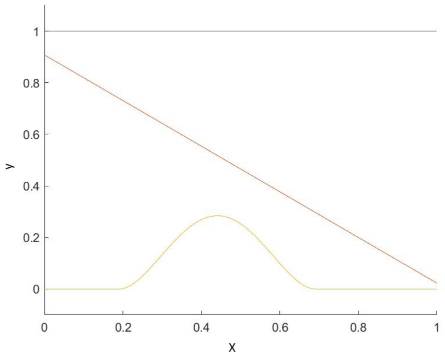

(c) Particle position at t=0.48 ($h'(0) = -0.5$)

Figure 5.18: Particle motion with $h'(0) = -0.5$

The run stops one time step before the collision with the fixed part of the lower wall in figure 5.18c. As we can see from the graphs, this is not a realistic model. For, as the particle moves, the lower wall still remains a small gap even at the closest time in figure 5.18b. Therefore, next we can improve the model by increasing the initial velocity from $h'(0) = -0.5$ to $h'(0) = -0.55$ to find the "optimal solution". The results are shown in figure 5.19.

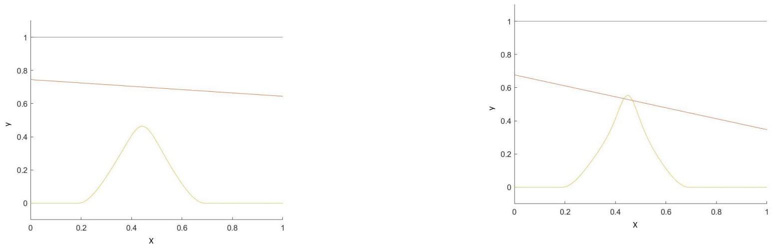

(a) Particle position at t=0 ($h'(0) = -0.55$) **(b)** Particle position at t=0.34 ($h'(0) = -0.55$)

Figure 5.19: Particle motion with $h'(0) = -0.55$

As in the previous cases, this test stops one time step before the collision with the lower wall. From the results in the figure 5.19, we notice that lower wall goes through the particle in figure 5.19b, breaking the original assumptions. Therefore, we can conclude that when the initial velocity of the particle is between $h'(0) = -0.55$ and $h'(0) = -0.5$, we can obtain an "optimal solution" of the model in which the particle almost touches the flexible part of the lower wall without significant deformation. Some other initial conditions are found to be unrealistic physically in the sense that they make the particle and the lower wall overlap immediately. We omit such cases.

In this chapter we tested a number of different cases: a particle with downwards speed, a particle with zero thickness. We almost have one optimal solution for the "touch" model – the model uses $c_1^* = 0.5$, $p_0 = 2$, $-0.5 < h'(0) < -0.55$, $\theta_0 = -0.1$ as the initial conditions. Also we will do further researches with this model in the following sections.

5.5 Accuracy check

The current part and subsequent parts 5.5-5.7 examine further aspects of the parameter space of solutions of the fluid-body interactions in a channel. The aim here is to increase understanding of the interactions and in particular study the phenomenon of possible spiking of the flexible wall. Spikes, in the sense of near-discontinuities in the slope of the flexible wall, are suggested by the numerical findings in a number of the present results. Eventually we would wish to comprehend the nature of such spikes in analytical terms.

Recall from the core equations for particle movements,

$$mh_{tt} = c_L, \tag{5.20}$$

where m is the particle mass, h is the height function for the particle, c_L represents the lift force which acts on the particle. We set $h_t = \frac{V}{m}$ and we find $V_t = c_L$. However, it is impossible to solve the equation (5.20) analytically. Thus in the coding language, we treat the particle movement as a discrete time movement. We believe, when the time-step is small enough, the particle movement could simulate the continuous motion. Thus in the coding, we are using the relation (5.21) to solve the equation (5.20).

$$\frac{V(t+\delta t)-V(t))}{\delta t}=c_L. \tag{5.21}$$

But when we use Taylor expansion of $V(t+\delta t)$, we should have the Taylor relation below,

$$V(t+\delta t)=V(t)+\delta t V'(t)+O((\delta t)^2)+\dots . \tag{5.22}$$

Thus when we substitute equation (5.22) into equation (5.21), we will have the relation as (5.23),

$$V'(t)+O(\delta t)=c_L. \tag{5.23}$$

Actually, the analytical ODE is (to repeat)

$$V'(t)=c_L. \tag{5.24}$$

Thus reducing δt should make (5.21) closer to (5.24). The $O(\delta t)$ error is the usual finite-difference error for an Euler scheme such as ours.

With above analysis, we check the accuracy for this model. We use $h(0)=0.5$, $h'(0)=0$, $\theta(0)=-0.1$, with $e_1^*=-0.001$, $e_2^*=0.001$, $e_3^*=-0.001$, $c_1^*=0.05$, $p_0=2$, $dt=0.01$ as our test conditions and the results are shown in figure 5.20.

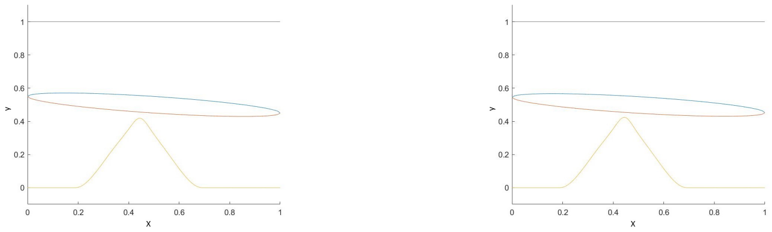

(a) Particle position at t=0 ($dt = 0.01$) **(b)** Particle position at t=0.07 ($dt = 0.01$)

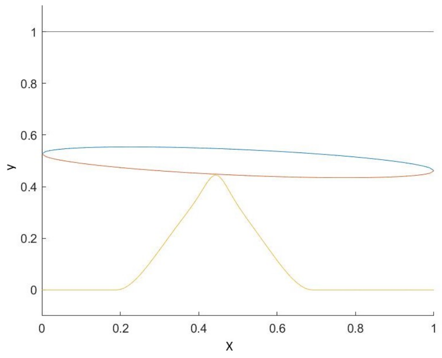

(c) Particle position at t=0.15 ($dt = 0.01$)

Figure 5.20: Accuracy check with time step $dt = 0.01$

For comparison, we keep all the values same as in the last test, except $dt = 0.005$, and the results are shown in figure 5.21.

(a) Particle position at t=0 ($dt = 0.005$) **(b)** Particle position at t=0.07 ($dt = 0.005$)

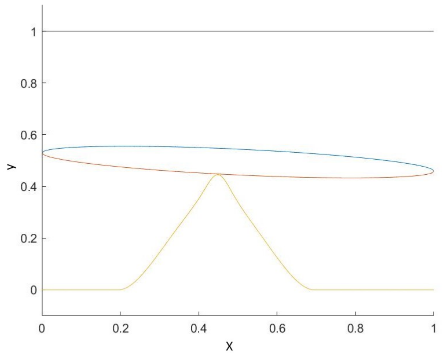

(c) Particle position at t=0.145 ($dt = 0.005$)

Figure 5.21: Accuracy check with $dt = 0.005$

From the figures 5.20 and 5.21 (and their data) we can read, the positions of the particle are almost the same at almost the same times and the shape changes of the lower wall are almost the same too. Besides the collision between the bottom wall and particle, we also ran a test about the collision between the particle and the upper wall. Unlike before, we use $h(0) = 0.7$, $h'(0) = -0.1$, $\theta(0) = -0.1$, with $e_1^* = -0.001$, $e_2^* = 0.001$, $e_3^* = -0.001$, $c_1^* = 0.5$, $p_0 = 1.8$,$dt = 0.01$ as our test conditions. The reason why we use this is that when we use a lower initial height, the particle collision happens too fast. Thus we increase the initial height a little bit. We also would like to see more difference, which means we would like our particle to be moving in the channel for a longer time. With these concerns, we decrease the external pressure a little and add a small downward speed. With all the above considered, we run the test and show the results below.

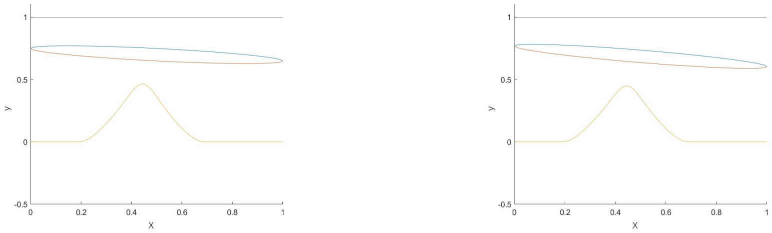

(a) Particle position at t=0 ($dt = 0.01$, upper collision)

(b) Particle position at t=0.16 ($dt = 0.01$, upper collision)

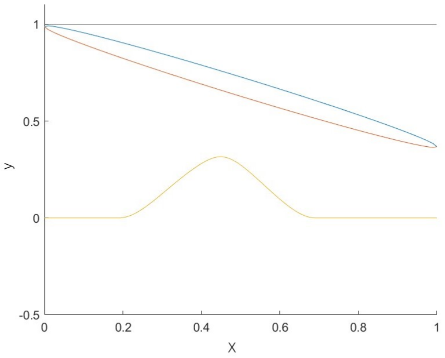

(c) Particle position at t=0.31 ($dt = 0.01$, upper collision)

Figure 5.22: Accuracy check with $dt = 0.01$, upper collision

In the serial comparison, we find the final collision point is just 1 time-step different. Thus, we use a smaller time-step $dt = 0.001$ to test a more accurate result. With this time-step, the results are shown below.

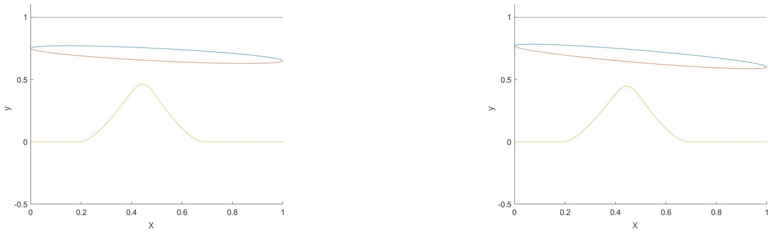

(a) Particle position at t=0 ($dt = 0.001$, upper collision)

(b) Particle position at t=0.16 ($dt = 0.001$, upper collision)

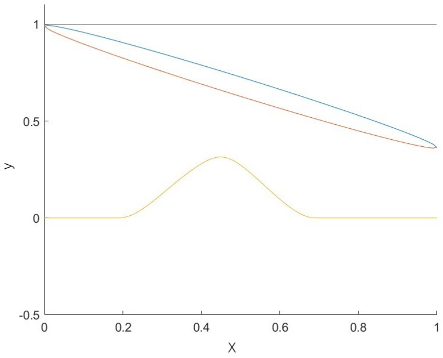

(c) Particle position at t=0.306 ($dt = 0.001$, upper collision)

Figure 5.23: Accuracy check with $dt = 0.001$, upper collision

From the figure 5.23 we notice that with a longer motion, there is more difference. But compared with the previous test, the collision times are closer between $dt = 0.01$ and $dt = 0.001$ cases. From the figure 5.23, we can see that under the more accurate calculation results, the motion trajectories of the particle and the lower side wall are roughly the same as in the previous results shown in figure 5.22. Therefore, we can deduce that the result of our operation is probably accuracy enough.

In this section, we checked the accuracy of applying different time-steps in two collision models. Both of them tell us that our calculations are fairly accurate. As a consequence, in the rest of the research, if more accuracy is not required, we may reasonably use $dt = 0.01$ to reduce the time taken by the program. In the next section, we will focus on the system of bottom wall shape equation without its 4th derivative term.

5.6 Bottom wall shape function without 4-th order cases

5.6.1 Background

Recalling from the equation (5.2), because in our model, the typical length factor $L*$ is large enough, thus, we can have the result that the parameter e_1 is much smaller than e_2 and e_3. Therefore, we derive the governing equations for our model as below,

$$e_2^* f_{xx} + e_3^* f = c_1^*(p_1^* - p_0^*). \tag{5.25}$$

In this model we still assume the blip shape is $y = f(x,t)$ and the non-dimensional constant coefficients $e_2^* = \frac{T_t^*}{U^{*2}L^*\rho^*}$, $e_3^* = \frac{-\kappa^* L^*}{U^{*2}\rho^*}$, with U^*, L^*, ρ^*, M^*, C^*, B^*, κ^*, T_t^*, p_1^*, p_2^* being the fluid velocity, the typical length factor, the uniform density of the incompressible fluid, the mass, the damping constant, the spring stiffness, longitudinal tension, internal lower pressure, external pressure respectively.

5.6.2 Test results for bottom wall shape function without 4-th order cases

We start the test with $h(0) = 0.7$, $h'(0) = -0.1$, $e_1^* = 0$, $e_2^* = 0.1$, $e_3^* = -0.1$, $c_1^* = 0.5$, $p_0 = 2$ and the results are shown below,

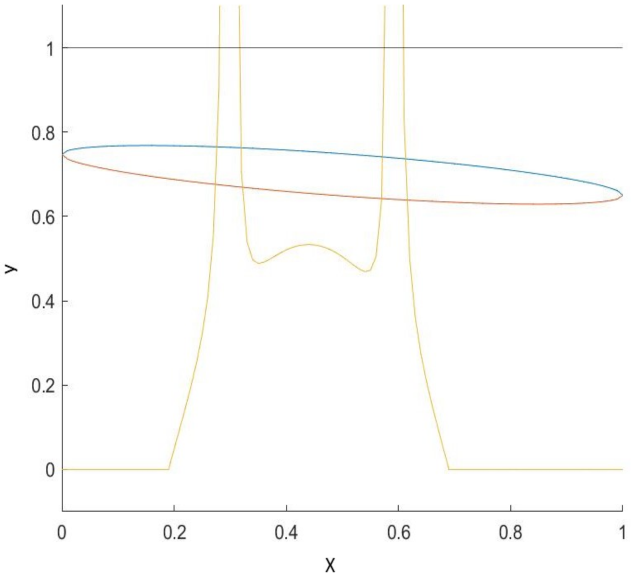

Figure 5.24: Initial test

From the figure 5.24, we notice that from the beginning, the bottom wall starting with a strange shape and cross the particle. Thus, we need to change the conditions to test the results. We increase the value e_2^* and decrease the value e_3^* and we got the results as below,

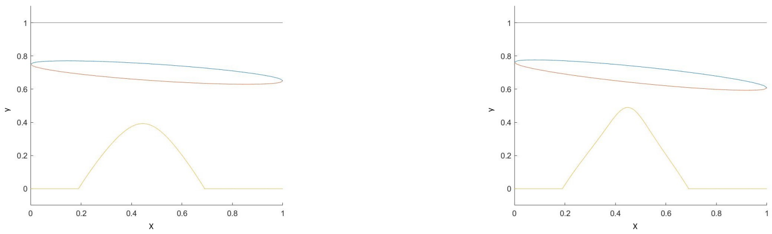

(a) Particle position at t=0 ($e_2^* = 0.2, e_3^* = -0.2$) **(b)** Particle position at t=0.15 ($e_2^* = 0.2, e_3^* = -0.2$)

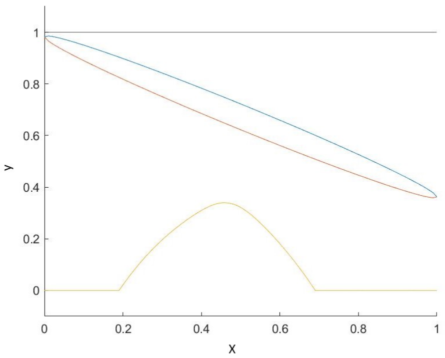

(c) Particle position at t=0.32 ($e_2^* = 0.2, e_3^* = -0.2$)

Figure 5.25: Particle motion with $e_2^* = 0.2, e_3^* = -0.2$

From figure 5.25, with above mentioned initial conditions, there are still a lot of space between the particle and the bottom flexible wall. Thus, we still need to increase the downwards speed or change other conditions. With this consideration, we keep the same initial conditions, except changing the parameters e_2^* from 0.2 to 0.3 and e_3^* from -0.2 to -0.3 and show the result as below,

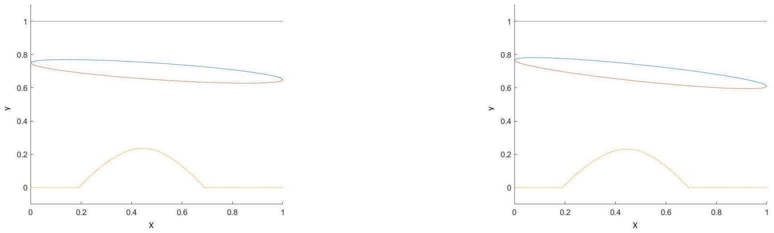

(a) Particle position at t=0 ($e_2^* = 0.3, e_3^* = -0.3$)

(b) Particle position at t=0.14 ($e_2^* = 0.3, e_3^* = -0.3$)

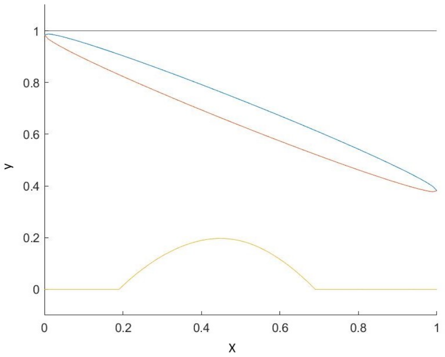

(c) Particle position at t=0.28 ($e_2^* = 0.3, e_3^* = -0.3$)

Figure 5.26: Particle motion with $e_2^* = 0.3, e_3^* = -0.3$

With $h(0) = 0.7$, $h'(0) = -0.1$, $e_2^* = 0.3$, $e_3^* = -0.3$, $c_1^* = 0.5$, $p_0 = 2$ initial conditions, the blip of the bottom wall is much lower than the second case. Also, the collision between the particle and the top wall happens sooner than the previous case.

From the results we can deduce that when we increase the values of e_2^* and decrease e_3^*, the height of the spike of the bottom wall will also decrease. Thus, if we want the collision happens between the particle and the bottom flexible wall, we should find a e_2^* between 0.1 to 0.2 and e_3^* between -0.1 to -0.2 and keep all the other conditions same.

Besides the above possible way, there is another method to make the collision happen—increasing initial downwards speed. With this assumption and above analysis, we increase the initial downwards speed from $h'(0) = -0.1$ to $h'(0) = -0.3$ and we start with $h(0) = 0.7$, $h'(0) = -0.5$, $c_1^* = 0.5$, $p_0 = 2$ as our initial conditions. We also notice that smaller values of e_2^* and e_3^* can make the spike of the bottom wall higher which means the collision might happen between the bottom wall and the particle before the test begins. With this result, we slightly increase the values of e_2^* and e_3^* and the typical results are shown below.

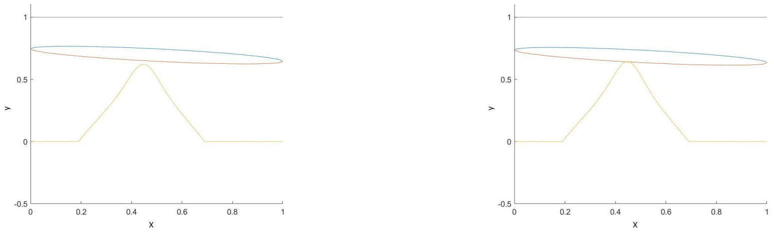

(a) Particle position at t=0 ($e_2^* = 0.19, e_3^* = -0.19$) **(b)** Particle position at t=0.03 ($e_2^* = 0.19, e_3^* = -0.19$)

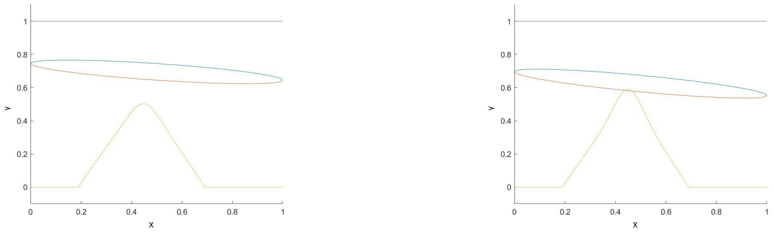

(c) Particle position at t=0 ($e_2^* = 0.2, e_3^* = -0.2$) **(d)** Particle position at t=0.15 ($e_2^* = 0.2, e_3^* = -0.2$)

Figure 5.27: Particle motion with different e_2^* and $e_3^* = -0.3$

In all the above cases we find that collisions happen. But when we keep increasing e_2^* to 0.21 and decreasing e_3^* to -0.21, figure 5.28 tells the results.

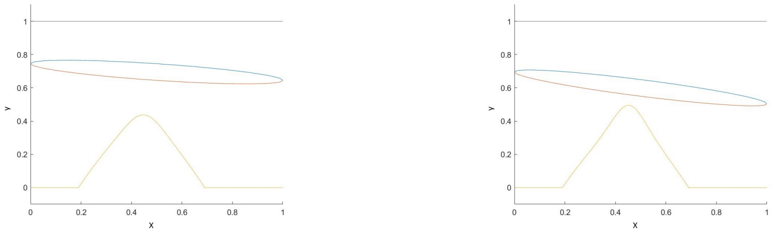

(a) Particle position at t=0 ($e_2^* = 0.21, e_3^* = -0.21$)

(b) Particle position at t=0.21 ($e_2^* = 0.21, e_3^* = -0.21$)

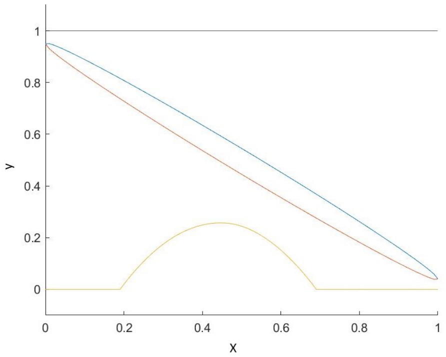

(c) Particle position at t=0.42 ($e_2^* = 0.21, e_3^* = -0.21$)

Figure 5.28: Particle motion with $e_2^* = 0.21, e_3^* = -0.21$

From the results we notice that there is no collision. Thus, with $h(0) = 0.7$, $h'(0) = -0.5$, $c_1^* = 0.5$, $p_0 = 2$ the interval value of $0.18 < e_2^* < 0.21$ and $-0.21 < e_3^* < -0.18$ enables the collision to occur.

In this section, we test some cases about bottom wall shape without 4th order term. During the test, we find increasing e_2^* and decreasing e_3^* will reduce the deformation of the wall. Therefore, this can reduce the collision possibility of the particle with the wall. As a consequence, the particle can move in the channel for a longer time. Besides this, we also find a possible ”optimal solution” for this kind of case. In the next section, we would like to do the research about negative external pressure’s influence to our model.

5.7 Negative external pressure

5.7.1 Background

In the previous sections, we conducted many groups of experiments and drew certain conclusions. But these conclusions and these experiments are all for positive external pressure. Therefore, in this chapter, we changed the external pressure to be negative. The specific experimental procedure will be shown below.

We use the same formula, but we change external pressure $p_0 = 2$ to $p_0 = -2$. Because in previous tests we found that when external pressure $p_0 = 2$, the lower wall will undergo obvious deformation, and the motion trajectory of the whole particle will also change accordingly. Thus, in this test, we set the initial conditions as $h(0) = 0.7$, $h'(0) = -0.1$, $e_1^* = -0.001$, $e_2^* = 0.001$, $e_3^* = -0.001$, $c_1^* = 0.3$, $p_0 = -2$. The result is shown below,

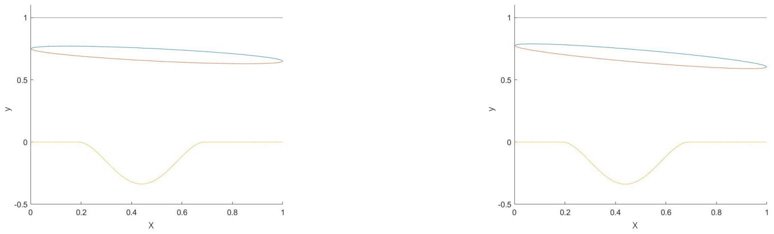

(a) Particle position at t=0 $(h'(0) = -0.1, c_1^* = 0.3)$ **(b)** Particle position at t=0.14 $(h'(0) = -0.1, c_1^* = 0.3)$

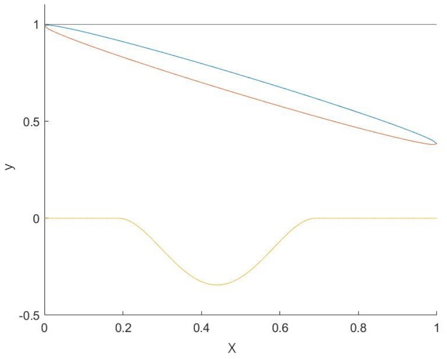

(c) Particle position at t=0.27 $(h'(0) = -0.1, c_1^* = 0.3)$

Figure 5.29: Particle motion with $h'(0) = -0.1, c_1^* = 0.3$

In above case we don't see any collisions between the particle and the bottom flexible wall. Due to the particle length is much more greater than the channel width, no matter what initial conditions we choose, there will be no collision between the bottom flexible part and particle. But the collision does exist between the bottom wall and particle. For instance, as we increase the initial downward velocity. We use different initial downwards velocity $h'(0) = -0.3$, $h'(0) = -0.5$, $h'(0) = -0.9$ as our initial condition and the results are shown in figure 5.30

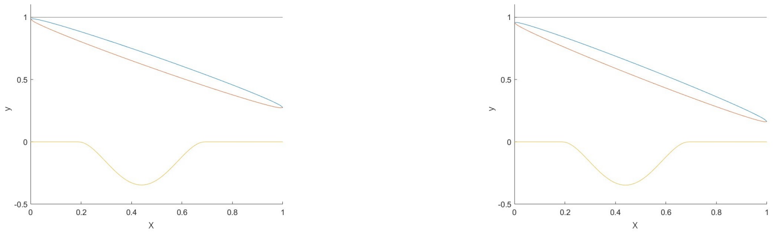

(a) Particle position at t=0.3 ($h'(0) = -0.3$) **(b)** Particle position at t=0.33 ($h'(0) = -0.5$)

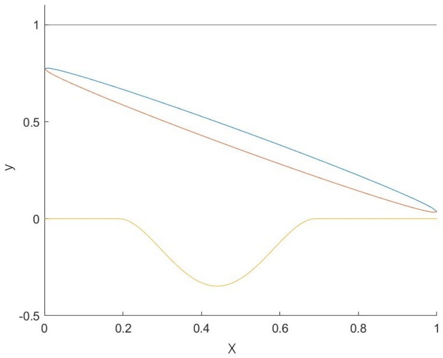

(c) Particle position at t=0.36 ($h'(0) = -0.9$)

Figure 5.30: Particle motion with different initial downwards velocity

All these results in figure 5.30 represent one time step before collision. It's not hard to read from the figure 5.30 that the particle position at the collision time is moving downwards. At the same time, with a larger downwards velocity, the particle will move longer in the channel. From the results we conclude that for the particle with downwards velocity less than 0.5, the particle will collide with the top wall. If downwards velocity greater than 0.9, the particle will collide with the bottom wall. Besides, with a faster downward speed, the collision will happen sooner. Also from the figure, we can read that there might be a longest motion between $h'(0) = -0.5$ and $h'(0) = -0.9$ case. For example, when we choose a special downwards velocity, the particle will "touch" the bottom wall but not collide. Then the particle moves back to collide with the top wall. Maybe the particle will have some oscillation or a quite stable case to moving in the channel forever.

5.8 Conclusion

In previous chapters, we considered fixed channel shapes. In this chapter, we extended the research from the previous studies to address a model in which one channel wall is partly flexible. Firstly, we found a ”suitable” external pressure to make the deformation more clear. Here the ”suitable” means the bottom wall flexible part has a noticeable deformation and it provides a large enough space (the gap between the bottom wall and upper wall) for the particle to move freely. With such a kind of ”suitable” external pressure, we ran tests to find out the influence of the internal pressure, external pressure and particle initial height. Then we added some initial downwards velocity to our particle and we also tested the zero-thickness case. For the next step, we did some tests about the bottom wall shape equation without its 4th order derivative. The reason why we did that is because when the typical length factor is large enough, which is similar to our previous assumptions, the parameter e_1^* may be small. Thus we have a new shape function as (5.25). With equation (5.25), we examined the influence of the parameters e_2^* and e_3^*. The influence of e_2^* and e_3^* is suitable for large longitudinal tension and spring stiffness respectively. We also gave an example of finding a possible ”near-optimal solution” in section 5.6. Prior to section 5.6, we studied the effects of positive external pressure, but next we focused on the negative external pressure cases. Here we found it is impossible to make the collision happen between the bottom flexible part and particle. But it is possible to have the collision between the particle and the bottom wall. In addition to these tests, there could be also some other interesting cases; for example, setting the whole bottom wall to be flexible or both of the top and the bottom walls being flexible could be a challenge topic. Finally here, the typical local behaviour during the onset of collision between the particle and the flexible wall when the external pressure is positive has still to be analyzed in detail.

Chapter 6

Particle in channel flow at low Reynolds numbers

6.1 Background creation

In the beginning of the thesis, we described research concerned with the motion of a particle in the high Reynolds number regime. This initial investigation focused on examining the behavior of the particle within the framework of the Euler equations of motion, which describe the dynamics of an ideal, inviscid fluid. The analysis was applied to reduced systems where the assumption of a separation-free, inviscid flow was adopted, simplifying the complex interactions between the particle and the fluid. These assumptions enabled a clearer understanding of the motion under high Reynolds number conditions, where inertial forces dominate and viscous effects are negligible.

By contrast, in this chapter, we shift our focus to a different flow regime, specifically considering a body moving in a channel flow at low Reynolds number. The transition to low Reynolds number flows introduces a new set of challenges, as the dynamics are now governed predominantly by viscous forces rather than inertial forces. This regime is characterized by slow, steady flows, where the influence of viscosity becomes more pronounced and cannot be neglected, unlike the high Reynolds number case. In this context, the flow is typically laminar, and the motion of the body must be analyzed under the influence of viscous drag and the associated resistance to movement.

This shift in focus allows for a more detailed exploration of the phenomena occurring at low Reynolds numbers, where the traditional assumptions of an inviscid fluid no longer hold. Instead, we must now consider the full effects of viscosity and explore how these forces influence the motion of the body within the confined geometry of a channel. This chapter aims to build on the insights gained from the high Reynolds number analysis and apply them to the distinct physical phenomena encountered in the low Reynolds number regime.

6.2 Model analysis (lubrication regime)

In this chapter, we continue to consider a particle with some thickness. However, for convenience, we begin by analyzing and testing the properties of the model using a zero-thickness particle. The aim here is to determine the lift and moment of inertia on the particle due to lubrication forces and then analyze the fluid-body interaction in full. (Later on, numerical study rather than analysis will be needed for less simple particle shapes.)

Now we assume that the gap widths are of the form $H_n = A_n + B_n x$, with constants satisfying

$$A_2 = 1 - A_1 \text{ and } B_2 = -B_1. \tag{6.1}$$

The graph of the setup is shown in figure 6.1.

We consider the flow past a thin freely-moving body in a channel. This model has notation $(p_1, H_1, p_2, H_2, h(t), \theta(t))$ similar to that studied in the previous chapter 2, but now the Reynolds number is small and the scaled pressures p_0, p_3 at the leading and trailing edge ($x = 0, 1$) respectively are prescribed constants with $p_0 > p_3$. Typically we can take $p_0 = 1, p_3 = 0$.

The gap widths are written as

$$H_1 = F^-(x) + h(t) + (x - C)\theta(t), \tag{6.2}$$

$$H_2 = 1 - [F^+(x) + h(t) + (x - C)\theta(t)] \tag{6.3}$$

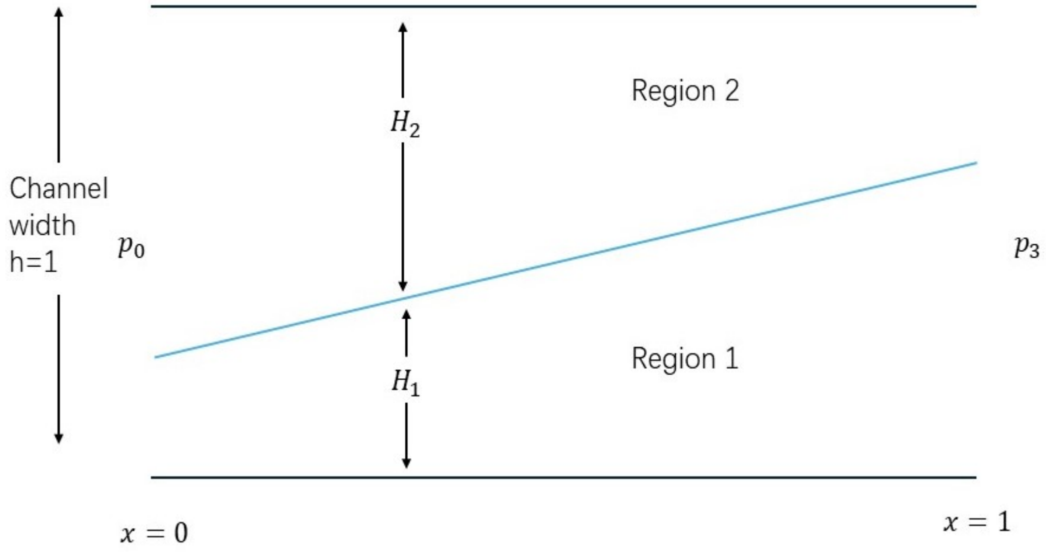

Figure 6.1: Model setup. Total channel width is 1. The pressure at $x = 0$ is p_0 and the pressure at $x = 1$ is p_∞. The distance between the upper wall and the particle is $H_2(x,t)$. The distance between the bottom wall and the particle is $H_1(x,t)$.

with the usual notation.

Recalling from the incompressible Navier–Stokes equation we have,

$$\rho(u_t + uu_x + vu_y) = -p_x + \mu(u_{xx} + u_{yy}) \tag{6.4}$$

Since we assume the whole process happens in steady flow, thus we ignore the u_t term on the left hand side of equation (6.4). Thus the typical magnitudes of left hand side of equation (6.4) is $\rho\frac{U_0{}^2}{L}$ while the viscous terms scales as $\mu\frac{U_0{}^2}{h^2}$.

In lubrication theory, we assume the inertia terms are negligible, thus we have the relation below,

$$\rho\frac{U_0{}^2}{L} \ll \mu\frac{U_0{}^2}{h^2} \Rightarrow Re(\frac{h}{L})^2 \ll 1 \text{ where } Re = \frac{\rho U_0 L}{\mu} \text{ and } h \ll L \tag{6.5}$$

Then we keep the dominate terms in 2D lubrication theory

$$P_x = \mu u_{yy}, P_y = 0. \tag{6.6}$$

For convenience, we use P to represent the pressures to deduce the Reynolds lubrication equation.

Thus, solving (6.6) we can have,

$$P = P(x,t), u = \frac{P_x}{2\mu}(y^2 + Ay + B), \tag{6.7}$$

where A, B are constants. Then we impose the boundary conditions $u = 0$ at $y = 0$, $u = (U_0, V_0)$ at $y = h$ in (6.7) we have,

$$u = \frac{P_x}{2\mu}(y^2 - hy) + \frac{U_0}{h}y \tag{6.8}$$

Then we impose the continuity of mass, by integrating $\nabla \cdot u = 0$ across the layer we have,

$$\frac{\partial}{\partial x}\int_0^{h(x,t)} u(x.y.t)dy = \int_0^{h(x,t)} \frac{\partial u}{\partial x}dy + u(x,y,h,t)\frac{\partial h}{\partial x} = \int_0^{h(x,t)} u_x dy + U_0 h_x \tag{6.9}$$

Then we use the incompressibility condition,

$$u_x + v_y = 0 \Rightarrow v_y = -u_x. \tag{6.10}$$

Thus we have,

$$V_0 = \int_0^{h(x,t)} v_y dy = -\int_0^{h(x,t)} u_x dy. \tag{6.11}$$

After substituting (6.8) into (6.11) and solving it, we have,

$$\frac{1}{12\mu}\frac{\partial(h^3 P_x)}{\partial x} = V_0 - \frac{1}{2}U_0 h_x. \tag{6.12}$$

Because the channel walls are stationary, thus we can assume the $U_0 = V_0 = 0$. As a consequence, we have

$$\frac{\partial(h^3 P_x)}{\partial x} = 0 \tag{6.13}$$

After replacing h by H_n and P by p_n in (6.13), the result leads to Reynolds lubrication equation in the form

$$\frac{\partial({H_n}^3 p_{nx})}{\partial x} = 0 \tag{6.14}$$

for $n = 1,2$ in the lower gap and upper gap respectively. So

$$p_{nx} = \frac{c_n}{{H_n}^3} \tag{6.15}$$

where the unknown constant c_n represents the mass flux to be determined in each gap. Hence we have

$$p_n = p_0 + c_n \int_0^x {H_n}^{-3} dx, \tag{6.16}$$

for $0 < x < 1$ and n for 1 and 2 represent lower and upper gap respectively. Applying the condition $p_n = p_3$ at the trailing edge then gives us

$$p_3 = p_0 + c_n \int_0^1 {H_n}^{-3} dx, \tag{6.17}$$

We can use (6.17) to determine c_1 and c_2 in numerical steps. One thing that needs to be noticed is that when the particle is close to the channel walls, the gap width H_n decreases accordingly. However, in equation (6.17), P_3 and P_0 are constants, meaning that if the particle is close to the channel walls, the constants c_1 and c_2 will also decrease. Thus, from equation (6.15), the pressure in each gap also decreases, which makes the collision possible.

With the analysis above for the pressure contributions in the gaps we have,

$$p_n - p_0 = c_n \int_0^x \frac{1}{(A_n + B_n x)^3} dx, \tag{6.18}$$

where $p_n (n = 1,2)$ represents the different pressures at each position from 0 to 1 and the unknown constant c_n represents the mass flux to be determined in each gap.

Then we evaluate the right-hand-side of the above equation and rewrite the equation as below,

$$p_n - p_0 = c_n[\frac{(A_n + B_n x)^{-2}}{-2B_n} - \frac{(A_n)^{-2}}{-2B_n}]. \tag{6.19}$$

Then we can use the values at $x = 1$ to obtain the value for c_n. The detailed step is as follows,

$$P = p_3 - p_0 = c_n[\frac{(A_n + B_n)^{-2}}{-2B_n} - \frac{(A_n)^{-2}}{-2B_n}]. \tag{6.20}$$

Hence for the lift force term,

$$c_L = \int_0^1 (P_1 - P_2)dx. \tag{6.21}$$

Noting $P_1 = p_1 - p_0$, $P_2 = p_2 - p_0$, using $P_1 - P_2 = (p_1 - p_0) - (p_2 - p_0)$ and substituting into equation (6.21), then we can find the result as below,

$$c_L = \frac{c_1}{-2B_1}[\frac{(A_1+B_1)^{-1}-(A_1)^{-1}}{-B_1} - (A_1)^{-2}] - \frac{c_2}{-2B_2}[\frac{(A_2+B_2)^{-1}-(A_2)^{-1}}{-B_2} - (A_2)^{-2}]. \tag{6.22}$$

Similarly, for the moment equation's right-hand side,

$$c_M = \int_0^1 (x - C)(P_1 - P_2)dx, \tag{6.23}$$

we derive

$$c_M = -Cc_L + \int_0^1 x(P_1 - P_2)dx. \tag{6.24}$$

Putting

$$\int_0^1 x(P_1 - P_2)dx = \int_0^1 x(p_1 - p_0)dx - \int_0^1 x(p_2 - p_0)dx, \tag{6.25}$$

we set

$$I_1 = \int_0^1 x(p_1 - p_0)dx, \quad I_2 = \int_0^1 x(p_2 - p_0)dx. \tag{6.26}$$

After some algebraic steps we obtain the relations below,

$$\frac{-2B_1}{c_1}I_1 = \frac{1}{(B_1)^2}\ln(\frac{A_1+B_1}{A_1}) + \frac{A_1}{(B_1)^2}[(A_1+B_1)^{-1}-(A_1)^{-1}] - \frac{1}{2}(A_1)^{-2}. \quad (6.27)$$

With the steps above, we find

$$\begin{aligned} c_M = -Cc_L - \frac{c_1}{2B_1}[\frac{1}{(B_1)^2}\ln\frac{A_1+B_1}{A_1} + \frac{A_1}{(B_1)^2}[(A_1+B_1)^{-1}-(A_1)^{-1}] - \frac{1}{2}(A_1)^{-2}] \\ +\frac{c_2}{2B_2}[\frac{1}{(B_2)^2}\ln\frac{A_2+B_2}{A_2} + \frac{A_2}{(B_2)^2}[(A_2+B_2)^{-1}-(A_2)^{-1}] - \frac{1}{2}(A_2)^{-2}]. \end{aligned} \quad (6.28)$$

From the above analysis, our body motion equations can be rewritten as follows,

$$Mh_{tt} = c_L, \quad (6.29)$$

$$I\theta_{tt} = c_M. \quad (6.30)$$

Also, the relation between A_1, B_1, h, θ is

$$A_1 = E + h - C\theta, \quad B_1 = \theta, \quad (6.31)$$

where E represents the particle's initial height, which has the same meaning as $h(0)$. Since sometimes we need some mathematical analysis, we split it from the height h.

With these relations we can use equation (6.31) to obtain the value for A_1, B_1 and use equation (6.1) to obtain the values for A_2, B_2. From equation (6.17) and (6.20) we then derive the value for c_1 and c_2. Then from equation (6.22) and (6.28), we can obtain the values for c_L and c_M. With these values of c_L and c_M, we may update h and θ from equation (6.29) and (6.30) for the next time step, in numerical terms.

6.2.1 Stability test

To examine the basic stability issue for the initially symmetric case of $E = 0.5$, where E has the same influence as α in the previous chapter for particle initial height, we substitute

$$A_1 = 0.5 + \varepsilon x e^{\alpha t} + ..., \quad B_1 = \varepsilon y e^{\alpha t} + ..., \tag{6.32}$$

where the constant $\varepsilon \ll 1$ and the constant α needs to be found. The reason we do this is that, firstly, with the above assumptions, $(A_1,\ B_1) = (0.5, 0)$ corresponds to an exact solution of the system. Secondly, x, y are distinct from the original coordinates.Thirdly, in the system, we are considering the general case where the perturbations of A_1, B_1 significantly affect each other; this is why both of the perturbations are of order ε and proportional to $e^{\alpha t}$. The time-dependence $e^{\alpha t}$ applies because there is no explicit t in the governing equations(6.29, 6.30). Thus with (6.22), (6.29) and (6.31) we obtain

$$h = -E + (A_1 + CB_1), \tag{6.33}$$

$$\varepsilon M \alpha^2 (x + Cy) = c_1 R_1 - c_2 R_2. \tag{6.34}$$

where

$$R_1 = \frac{1}{2B_1}\left[\frac{(A_1 + B_1)^{-1} - (A_1)^{-1}}{B_1} + A_1^{-2}\right], \tag{6.35}$$

defined from equation (6.22). Similarly, we define the expression for R_2

$$R_2 = \frac{1}{2B_2}\left[\frac{(A_2 + B_2)^{-1} - (A_2)^{-1}}{B_2} + (A_2)^{-2}\right], \tag{6.36}$$

By taking the leading order from the Taylor expansion and substituting equation (6.32) to the equation (6.35), we can get

$$-2\varepsilon y R_1 = \frac{(\frac{1}{2} + \varepsilon x + \varepsilon y)^{-1} - (\frac{1}{2} + \varepsilon x)^{-1}}{\varepsilon y} + (\frac{1}{2} + \varepsilon x)^{-2}. \tag{6.37}$$

Previously, from equation (6.20) and (6.32), we had the leading orders as below,

$$-2\varepsilon yP = c_1[(\frac{1}{2}+\varepsilon x+\varepsilon y)^{-2} - (\frac{1}{2}+\varepsilon x)^{-2}] \tag{6.38}$$

Hence, by using the Taylor expansion and taking first 2 terms,

$$-2\varepsilon yP = 4c_1[(1-4\varepsilon(x+y)) - (1-4\varepsilon x)]. \tag{6.39}$$

So

$$c_1 = \frac{P}{8}. \tag{6.40}$$

This is the lubrication result for an aligned flat plate. Similarly, $c_2 = \frac{P}{8}$ to the leading order. Higher order contributions are also important here. We find that we need to use higher order terms, as shown below.

Expanding (6.37) by Taylor series and taking the first 3 terms, we find

$$\begin{aligned} 2\varepsilon yR_1 = {} & \frac{2(1-2\varepsilon(x+y)+4\varepsilon^2(x+y)^2-8\varepsilon^3(x+y)^3) - 2(1-2\varepsilon x+4\varepsilon^2x^2-8\varepsilon^3x^3)}{\varepsilon y} \\ & +4(1-4\varepsilon x+12\varepsilon^2x^2). \end{aligned} \tag{6.41}$$

After some numerical steps, we can reach to the result below,

$$2\varepsilon yR_1 = 8\varepsilon y - 16\varepsilon^2(3xy+y^2). \tag{6.42}$$

Thus, we have $R_1 = 4-8\varepsilon(3x+y)$. Similarly, we obtain $R_2 = 4+8\varepsilon(3x+y)$.

Then, we used the Taylor expansion and took the first 3 terms for equation (6.38) to find the values for c_1 and c_2,

$$\begin{aligned} -2\varepsilon yP &= c_1[(\frac{1}{2}+\varepsilon x+\varepsilon y)^{-2} - (\frac{1}{2}+\varepsilon x)^{-2}] \\ &= 4c_1[-4\varepsilon y+12\varepsilon^2(2xy+y^2)] \end{aligned} \tag{6.43}$$

Then we got $c_1 = P/(8-24\varepsilon(2x+y))$. Similarly, we got $c_2 = P/(8+24\varepsilon(2x+$

$y)$). Then we substituted all these values in equation (6.34) we can have

$$\begin{aligned}\varepsilon M\alpha^2(x+Cy) &= c_1R_1 - c_2R_2 \\ &= \frac{P(4-8\varepsilon(3x+y))}{8-24\varepsilon(2x+y)} - \frac{P(4+8\varepsilon(3x+y))}{8+24\varepsilon(2x+y)} \\ &= P\frac{\varepsilon y}{1-9\varepsilon^2(2x+y)^2}.\end{aligned} \tag{6.44}$$

Because ε is small enough, thus we can rewrite the result as

$$M\alpha^2(x+Cy) = Py. \tag{6.45}$$

We did the similar calculation to equation (6.30), then we can have

$$I\alpha^2 y = \frac{1}{2}P(1-2C)y. \tag{6.46}$$

From equation (6.46), we can solve the eigenvalue α by

$$\alpha^2 = \frac{P(1-2C)}{2I} \tag{6.47}$$

This implies that for such a particle, when its center of mass $C < 1/2$, the equation has only imaginary solution. This will lead to a stable oscillation in our model. When $C = 1/2$, we have neutrality. For $C > 1/2$, α has a real positive root which implies that the interaction is unstable and a collision may happen readily between the particle and the channel.

To test this, we use zero thickness, center of mass position at 0.1, mass equal to 2, moment of inertia equal to 0.4, $p_0 = 10$, $p_3 = 0$, $dx = 0.001$, $dt = 0.01$, total time equal to 10, initial angle equal to 0.01, initial angular acceleration equal to 0, initial height equal to 0.5, initial velocity equal to zero as the initial conditions. With the above initial conditions, we find,from numerical solution of the system described at the end of section 6.2, the θ graph as in figure 6.2,

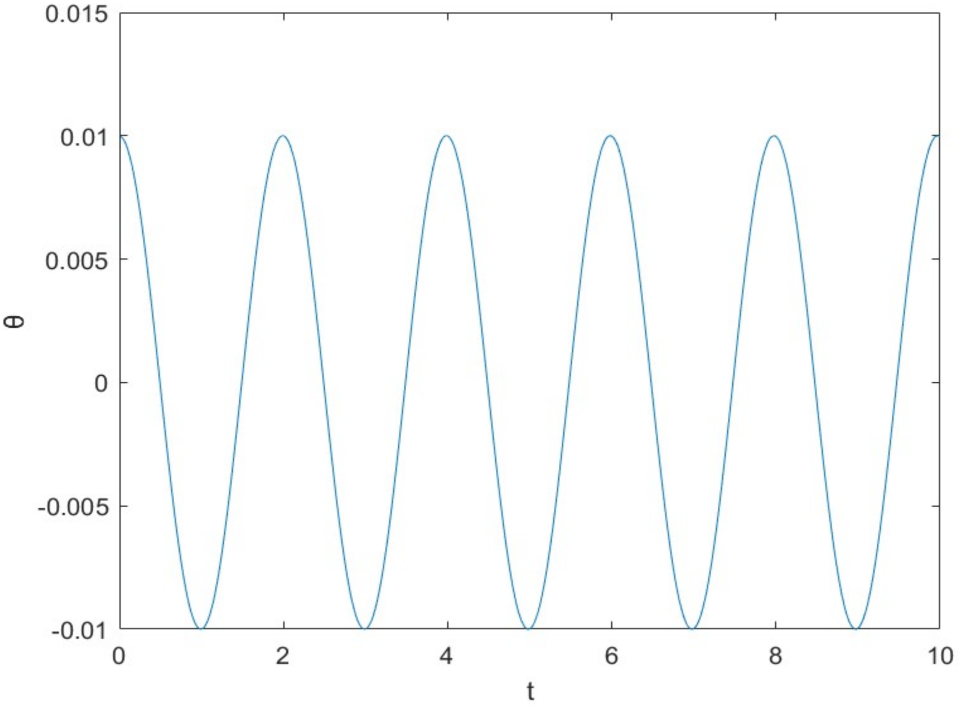

Figure 6.2: θ function up to time $t = 10$.

From the figure 6.2, we can read that the period is around 2. From the numerical data we find that the period is 1.98-1.99 closer to 1.99. At the same time, we can use the above analysis to get $\alpha = \sqrt{10}$ under these initial conditions. Thus, from the analysis, we can predict that the period is about 1.987. These two values for the period match each other quite well. In the following, we use the code to test the rest of conditions.

6.3 Flat plate analysis

6.3.1 Trailing edge analysis

In the previous section, we demonstrated the accuracy of our method. In this chapter, we will examine computationally the variation of the particle's trajectory under different initial conditions. First of all, we continue with the no thickness case. We use zero thickness, center mass position at 0.5, mass equal to 2, inertia equal to 0.01, $p_0 = 1, p_3 = 0, dx = 0.001, dt = 0.01$, total time equal to 1, initial angle equal to -0.5, initial angular acceleration equal to -0.5, initial height equal to 0.5, initial velocity equal to -0.5 as the initial conditions.

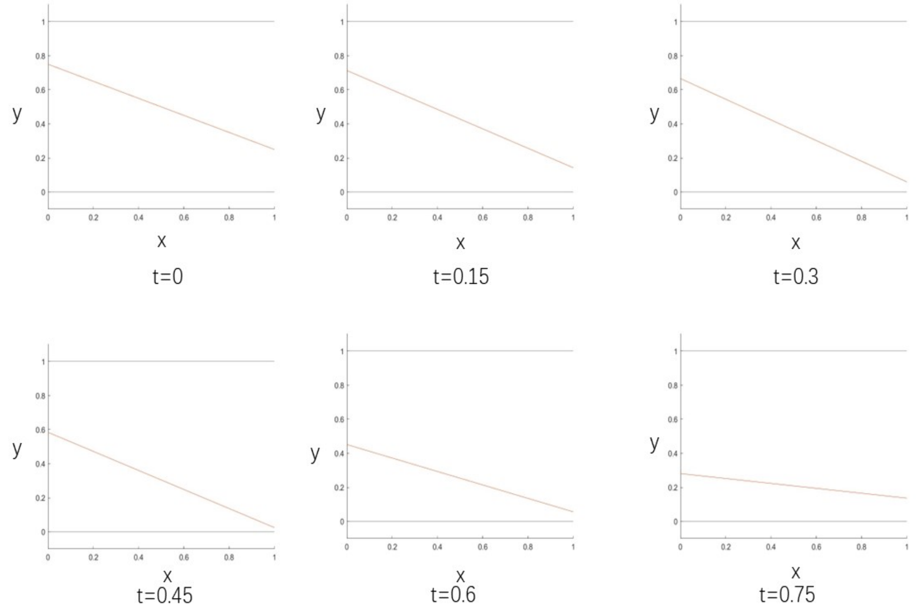

t=0 t=0.15 t=0.3

t=0.45 t=0.6 t=0.75

Figure 6.3: Test 1: Whole motion for zero-thickness case with $[\theta,\theta',h,h']$=[-0.5,-0.5,0.5,-0.5].

We show figure 6.3 first. It is not difficult to see from the figure that the progression of the particle is to first move downward, and rotate counterclockwise when the tail end approaches the bottom wall, but it does not quite collide with the bottom wall. Later, the front end of the particle eventually collides with the bottom wall. As far as the particle's trajectory is concerned, there arises the question of whether the trailing edge of our particle can ever collide with the lower wall,

We next modify the initial conditions so that the particle ends move closer to the lower wall without colliding with it. Thus, we use initial velocity equal to -0.6 as our new initial condition, and keep all the other conditions the same as in the last case. We obtain the results shown in figure 6.4.

It is notable that the interesting range of movements of the particle here and in other cases studied in the present section is largely due to the pressure forces acting on the particle. The gap pressures will be considered in detail in subsequent sections of this chapter. For the present case, it is not difficult to see from figure 6.4 that at around t=0.43, the distance between the end of the particle and the lower

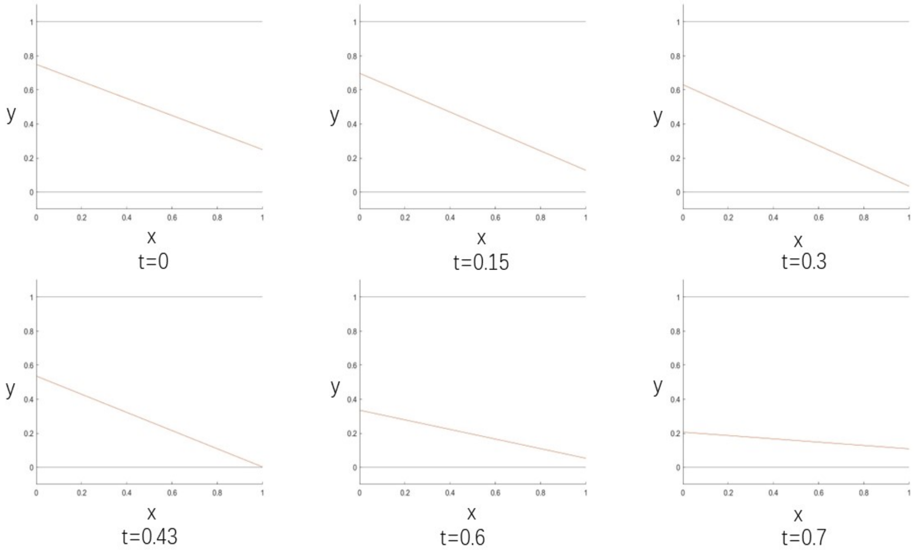

t=0

t=0.15

t=0.3

t=0.43

t=0.6

t=0.7

Figure 6.4: Test 2: Whole motion for zero-thickness case with $[\theta, \theta', h, h']$=[-0.5,-0.5,0.5,-0.6].

wall is very small, and there is almost a collision. The following table shows the numerical data of our particle trailing end between time t=0.39 and time t=0.49. It is observed from the table that t=0.43 is the position where the particle end is closest to the wall, but the distance between them is still greater than zero. Therefore, again our particle is not quite colliding with the lower wall.

From the results of the previous two tests, we found that when the initial velocity of the particle was increased, the distance between the trailing end of the particle and the lower wall became smaller and smaller, but the test results of these two tests indicated that the end of the particle would not collide with the wall. We want to know if the end of the particle can ever actually collide with the lower wall, so we continue to increase the initial downward velocity of the particle from -0.6 to -1. The results are shown in figure 6.6.

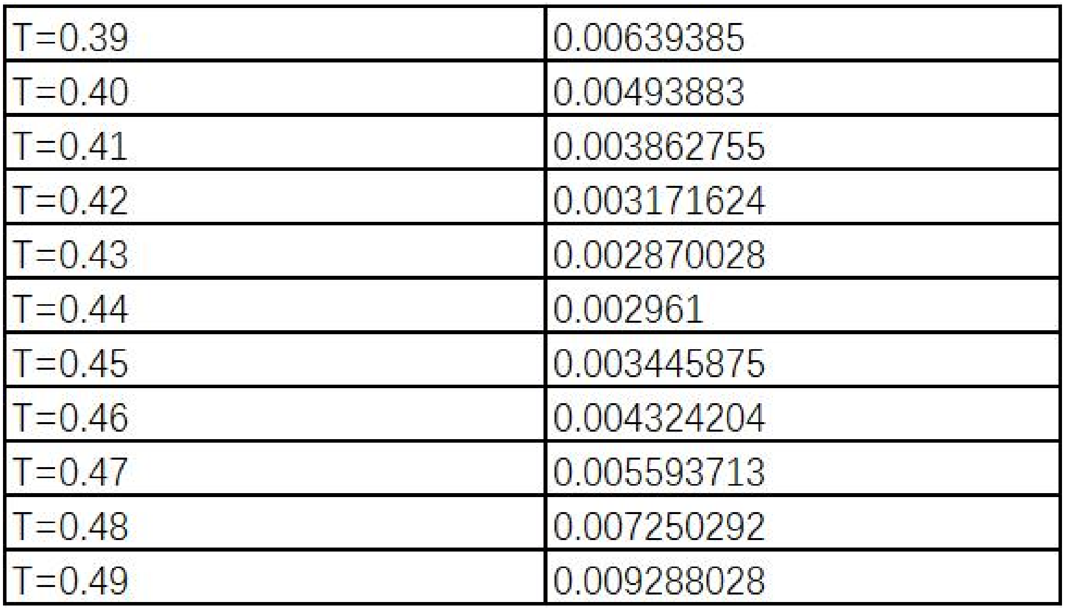

T=0.39	0.00639385
T=0.40	0.00493883
T=0.41	0.003862755
T=0.42	0.003171624
T=0.43	0.002870028
T=0.44	0.002961
T=0.45	0.003445875
T=0.46	0.004324204
T=0.47	0.005593713
T=0.48	0.007250292
T=0.49	0.009288028

Figure 6.5: Trailing edge height (distance from the lower wall) at time t=0.39 to t=0.49 for the case shown in 6.4.

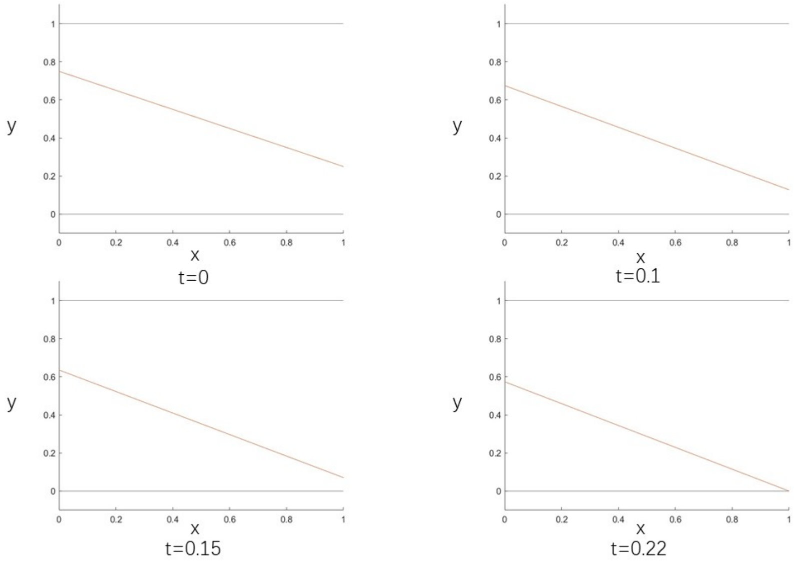

Figure 6.6: Test 3: Whole motion for zero-thickness case with $[\theta, \theta', h, h']$=[-0.5,-0.5,0.5,-1].

From figure 6.6, we see that when we increase the initial downward velocity of the particle to -1, the particle collides with the lower wall at t=0.22. This test tends to indicate that if the initial velocity of the particle is large enough in the downward direction, the trailing end of the particle can indeed collide with the lower wall.

6.3.2 Leading edge analysis

In the previous analysis, we obtained some results about the trajectory of the particle's rear end motion. In this section, we look at the trajectory of the particle's front end. For this examination we still use zero thickness, center mass position at 0.5, mass equals to 2, inertia equal to 0.4, $p_0 = 1, p_3 = 0, dx = 0.001, dt = 0.01$, total time equal to 3, initial angle equal to -0.3, initial angular acceleration equal to 0.2, initial height equal to 0.5, initial velocity equal to -0.2 as the initial conditions. The reason why we increase the inertia is because we want to examine whether the whole process can last longer. Results are shown in the figure 6.7.

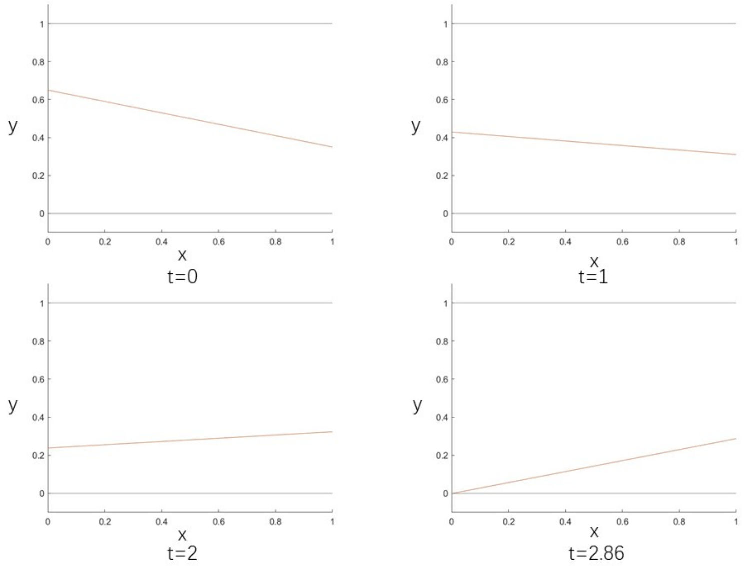

Figure 6.7: Test 4: Whole motion for zero-thickness case with $[\theta, \theta', h, h']$=[-0.3,0.2,0.5,-0.2].

In figure 6.7, we see that according to the initial conditions we mentioned earlier, the front end of the particle can collide with the lower wall. However, unlike in the previous tail-end collision, with a larger inertia and other initial conditions the front-end collision takes much longer, almost 13 times longer. In addition, we are also interested in whether the particle can collide with the upper wall, and how long that may take. Therefore, we set new initial conditions in which the initial angular acceleration equals -0.3 and the other conditions keep the same values as previously. The results are shown in figure 6.8.

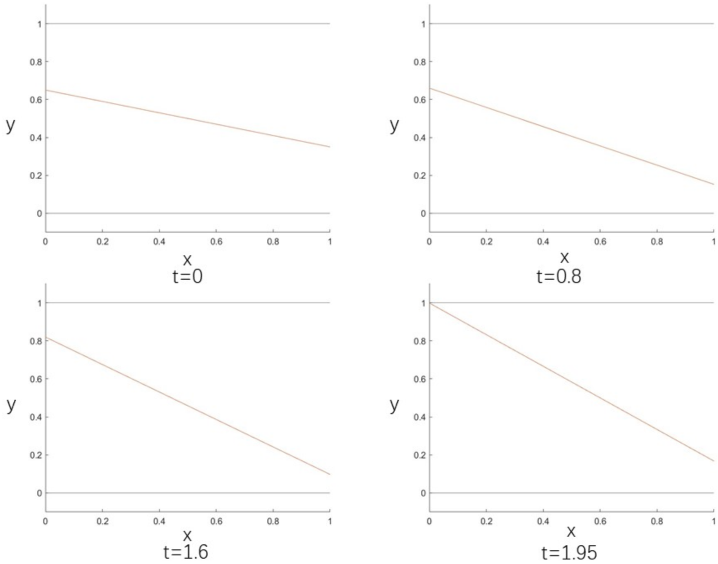

Figure 6.8: Test 5: Whole motion for zero-thickness case with $[\theta,\theta',h,h']$=[-0.3,-0.3,0.5,-0.2].

From figure 6.8, we can conclude that the collision time between the front end of the particle and the upper wall is shorter than that between the front end of the particle and the lower wall. One possible explanation is due to the fact that under the initial conditions we set, the acceleration of the particle moving clockwise is greater than in the previous counterclockwise case. Thus, the resulting particle collides with the upper wall more quickly. To test this conjecture, we modify the initial conditions with an initial angular acceleration equal to -0.2 and give it a smaller initial angle $\theta(0) = -0.2$, giving the result shown in figure 6.9.

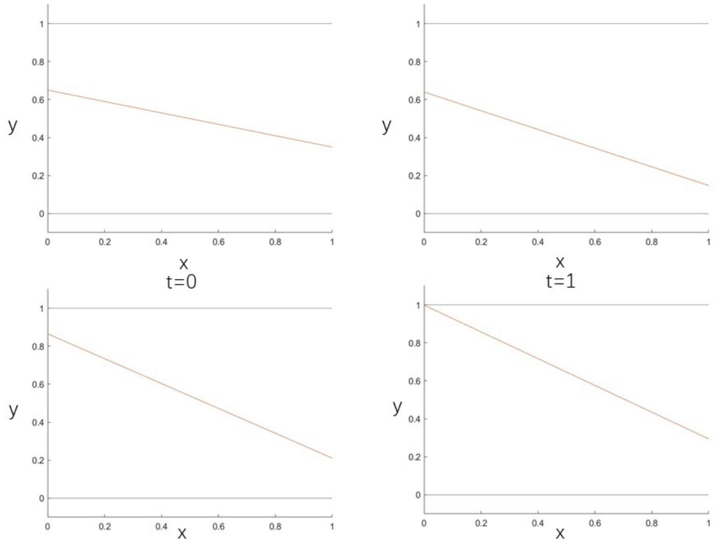

t=0 t=1

t=2 t=2.31

Figure 6.9: Test 6: Whole motion for zero-thickness case with $[\theta, \theta', h, h']$=[-0.2,-0.3,0.5,-0.2].

It can be seen from the diagram 6.9 that the collision time between the front end of the particle and the upper side wall is still shorter than before. This seems due to the influence of the initial angle of the particle.

In the next test, we choose a larger p_0 value. In Poiseuille flows [79, 80, 81, 82, 83, 84, 85, 86, 87, 88, 89, 90, 91], the value of u_x increases when we increase p_0. As u_x increases, particle trajectories become more pronounced. Therefore, in the next test, we use a larger p_0 to more clearly observe the changes in the particle trajectory. The following figure 6.10 shows the same tests as in figure 6.9 except for the p_0 increase from 1 to 10.

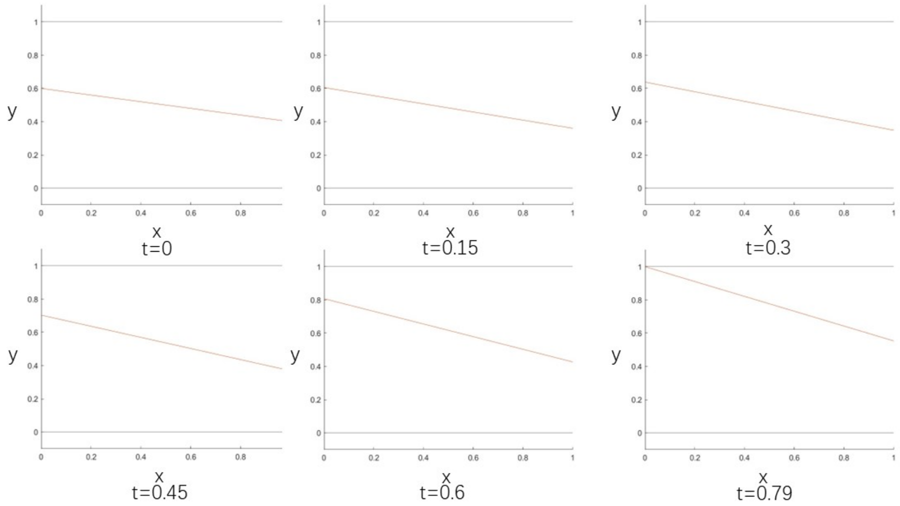

Figure 6.10: Test 7: Particle motion for zero-thickness case with $[\theta, \theta', h, h']$=[-0.2,-0.3,0.5,-0.2].

In figure 6.10, we see that the collision time of the particle is much shorter. This also means that in the same amount of time, the particle's trajectory is more pronounced of course. Since zero-thickness particles are almost impossible to exist in real life, we turn next to nonzero thickness cases.

6.4 Particle motion with thickness

In the previous section, we studied the motion trajectory of a zero-thickness particle and obtained the different motion responses of the particle under different initial conditions. Also at the end of the last section, we chose a larger p_0 value in order to make the trajectory of the particle clearer. In this section, we add thickness to the particle in order to better simulate the possible trajectory of particles in reality.

Based on the above ideas, we set the initial condition as $a = 0.3, b = 2, C = 0.1, M = 2, I = 0.4, p_0 = 10, p_3 = 0, dx = 0.001, dt = 0.01, t_{max} = 6, \theta(0) = 0.1, \theta'(0) = 0.3, h(0) = 0, h'(0) = 0.5$. This time we use $f^+ = a + x^{\frac{1}{2}}(1-x)^{\frac{1}{2}} * b$ as the upper body shape and $f^- = a$ as the lower body shape. Then we perform the computation and we find the following results.

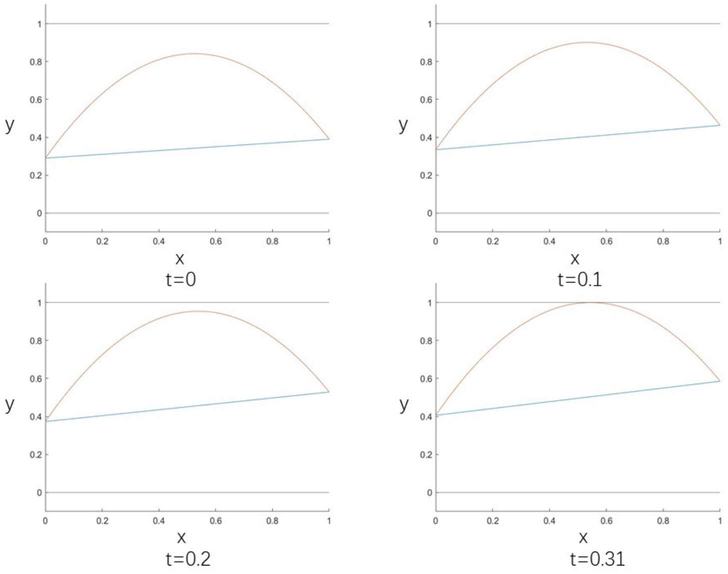

Figure 6.11: Test 8: Particle motion for particle with thickness case with $[\theta, \theta', h, h']$=[0.1,0.3,0.3,0.5].

Figure 6.11 indicates the shape of the particle with the upper half being a parabola and the lower side being flat. The initial conditions that we set lead to the particle moving upwards. Previously, in the motion of the particle without thickness, only the front and back ends of the particle collide with the upper (or lower) channel walls, whereas in this case the middle-curved part of the particle is found to collide with the upper wall.

Figure 6.12 shows the height variation of the front and back ends of the particle.

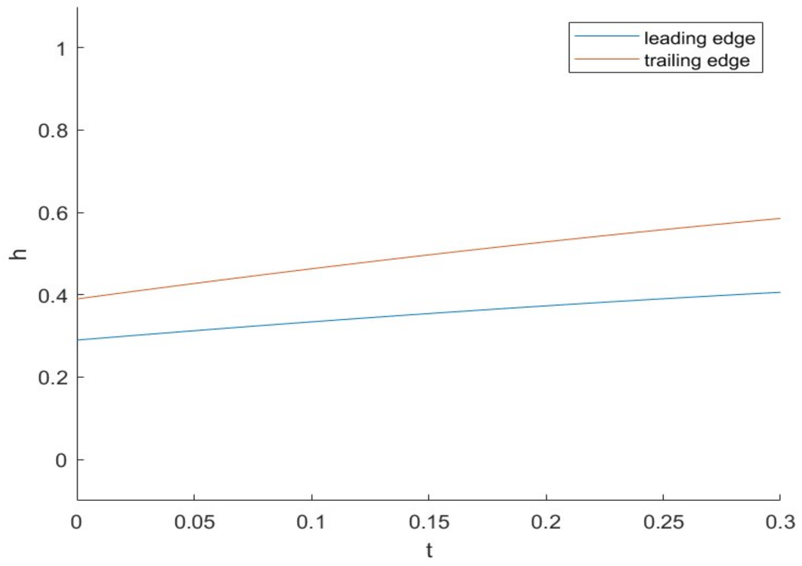

Figure 6.12: Leading edge and trailing edge height for test 8.

The red curve in figure 6.12 represents the trajectory of the trailing edge of the particle, and the blue curve represents the trajectory of the leading edge of the particle. According to these two curves and the motion process of the particle shown in figure 6.11, we can deduce that the particle only moves upward in one direction, and the top edge collides with the upper channel wall.

Besides these, the figure 6.13 shows the pressures at different times, i.e. the upper and lower pressures acting on the particle. 'LP' stands for lower pressure and 'UP' stands for upper pressure. The number in the logo represents its corresponding time step. For example, 'LP0' represents the lower pressure at time t=0, 'UP0' represents the upper pressure at time t=0, 'LP0.31' means the lower pressure at time t=0.31, etc.

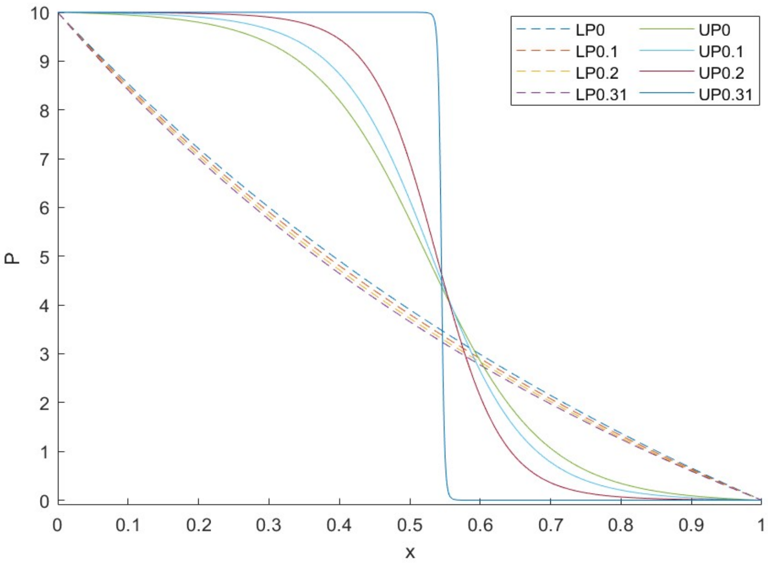

Figure 6.13: Upper and lower pressure for test 8.

From figure 6.13, we can see that the pressure on the lower side of the particle does not change significantly, but the pressure on the upper side of the particle changes much more significantly. This is because the distance between the particle and the upper wall at the collision point becomes very small, which leads to a decrease in the amount of fluid flow, but also causes the pressure on the upper side of the particle to plummet after passing through the neighbourhood of the imminent collision point.

At the same time, in the related paper ”Free motion of a slender particle in lubricating channel flow”, by Liu, Jepson and Smith (2024), several other situations are shown, for example, where the front end or the back end of the particle collides with the lower channel wall.

In addition to the half-parabolic and zero-thickness particle models described above, we have run other simulations, such as an elliptic particle simulation. This time we still use $f^{+} = a + x^{\frac{1}{2}}(1-x)^{\frac{1}{2}} * b$ as the upper body shape function and $f^{-} = a - x^{\frac{1}{2}}(1-x)^{\frac{1}{2}} * b$ as the lower body shape function. This is presented in figure 6.14.We use $a = 0, b = 0.3, C = 0.5, M = 2, I = 0.4, p_0 = 10, p_3 = 0, dx = 0.001, dt = 0.01, t_{max} = 1, \theta(0) = -0.5, \theta'(0) = 0.4, h(0) = 0.5, h'(0) = -0.4$ as the initial conditions.

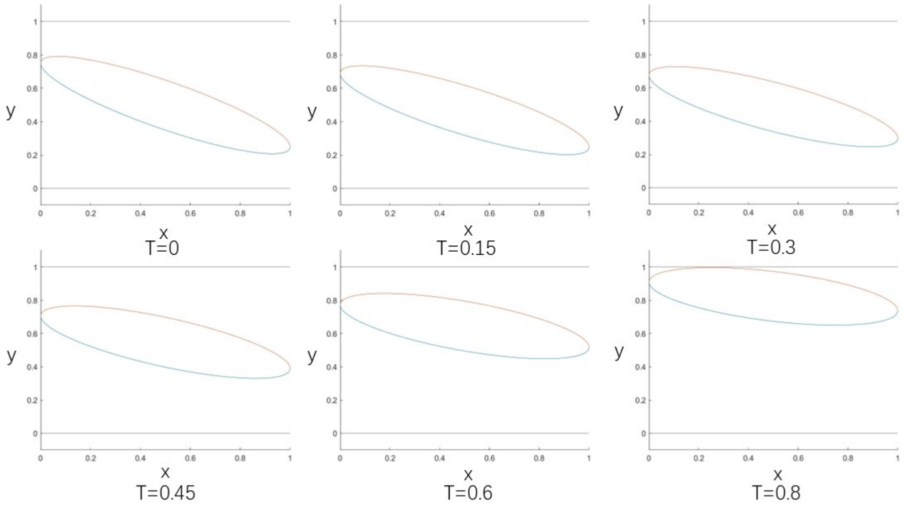

Figure 6.14: Test 9: middle curve of the elliptical particle collides with the top wall.

The figure 6.14 represents the trajectory of the elliptical particle under the above initial conditions. The particle initially moves down, but does not collide with the underlying wall. The particle then moves up, and eventually the curved upper edge of the particle collides with the upper wall. This is different from the previous case with the individual upward motion, and the following figure shows the height of the leading and trailing edges of the particle. Different from the previous case, the height variation curve of the leading and trailing edges of the particles is more obvious in this figure. This is also in line with the conclusion that we obtained from figure 6.14 that the particle first moves down and then moves up.

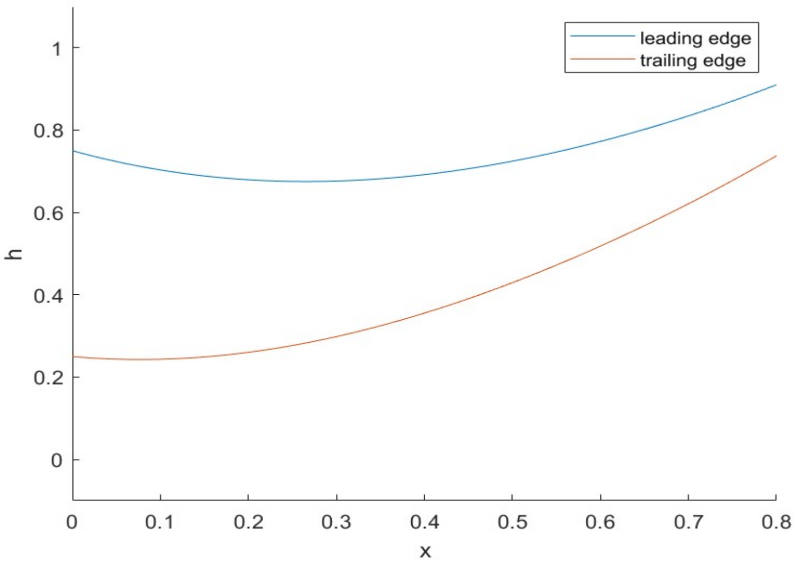

Figure 6.15: Leading edge and trailing edge height for test 9.

Same as in the previous figures, the figure 6.16 also shows the change of the upper and lower pressures of the particle at different times.

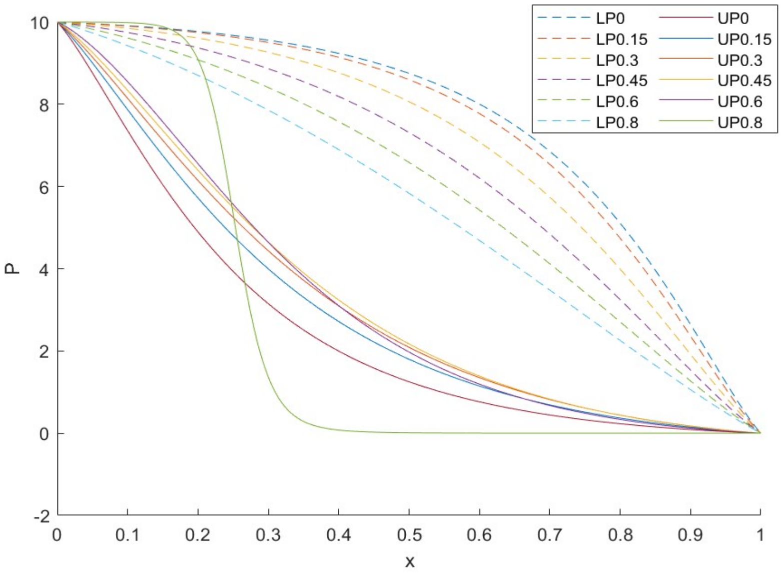

Figure 6.16: Upper and lower pressure for test 9.

Unlike before, this time the particle's top edge collision point is near $x = 0.3$. So we can see in figure 6.16 that the particle's upper pressure first suddenly drops around $x = 0.3$.

So far, the present tests have all ended with particles hitting the upper wall. We are curious about how the particle can collide with the bottom wall. Thus, we modify the initial condition with $b = 0.3, C = 0.5, M = 2, I = 0.4, p_0 = 10, p_3 = 0, dx = 0.001, dt = 0.01, t_{max} = 3, \theta(0) = -0.5, \theta'(0) = 0.7, h(0) = 0.5, h'(0) = -1.3$ and the results are shown in figure 6.17.

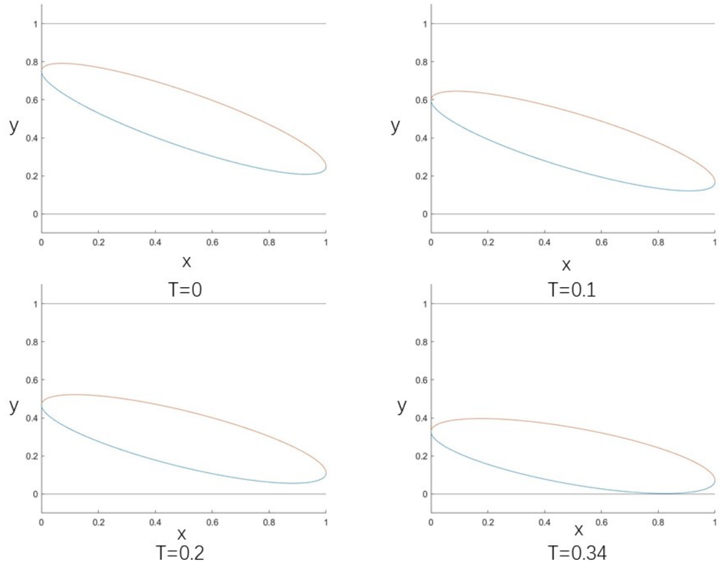

Figure 6.17: Test 10: middle curve of the elliptical particle collides with the bottom wall.

It is easy to see from the figure that in this test, the curved part of the lower edge of the particle collides with the lower wall successfully. In this test, we set a relatively large downward initial speed. Because at the small initial velocity previously set, the particle will approach the lower wall but eventually collide with the upper wall. This also means that if we set the initial velocity to a certain ”right” value, our particle will ’touch’ the lower wall but not collide.

Also, in figure 6.18 we show the height variation of leading and trailing edges.

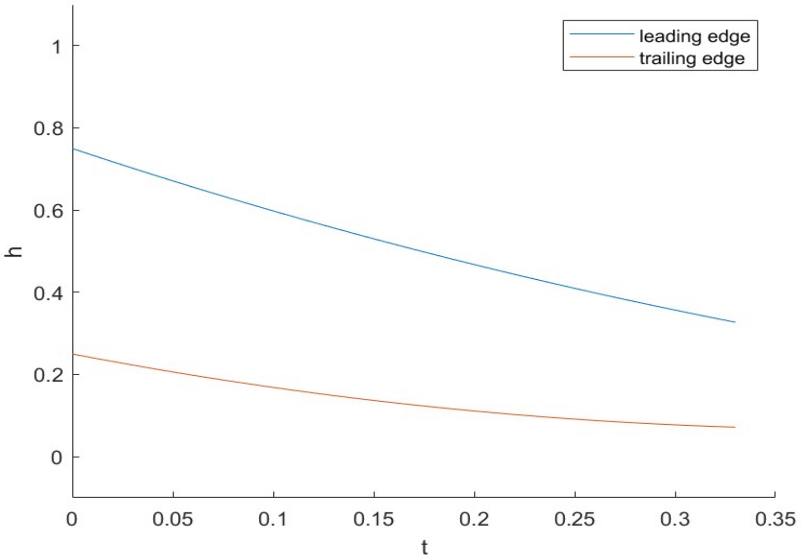

Figure 6.18: Leading edge and trailing edge height for test 10.

From figure 6.18, we can conclude that with such a large initial downward velocity, the particle will collide with the lower wall before it has time to move upward. However, the particle has a tendency to move upward during the whole process of motion. This conclusion can be drawn from the slope change of the curve in figure 6.18, and the falling speed of the particle is reduced.

The following figure 6.19 shows the pressure changes.Different from the previous results, the collision occurs on the lower edge of the particle, and the position is near the middle and back of the lower edge of the particle, around the position of 0.8.

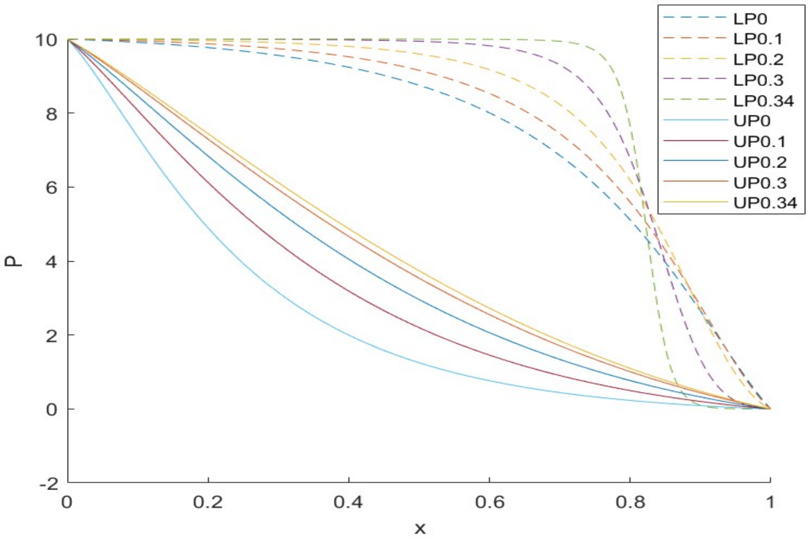

Figure 6.19: Upper and lower pressure for test 10.

Besides these, we also find a possible test result for the close but non-colliding model mentioned earlier. The initial conditions are as follows $b = 0.3, C = 0.5, M = 2, I = 0.4, p_0 = 10, p_3 = 0, dx = 0.001, dt = 0.01, t_{max} = 3, \theta(0) = -0.5, \theta'(0) = 0.5, h(0) = 0.5, h'(0) = -1.2$. See figure 6.20.

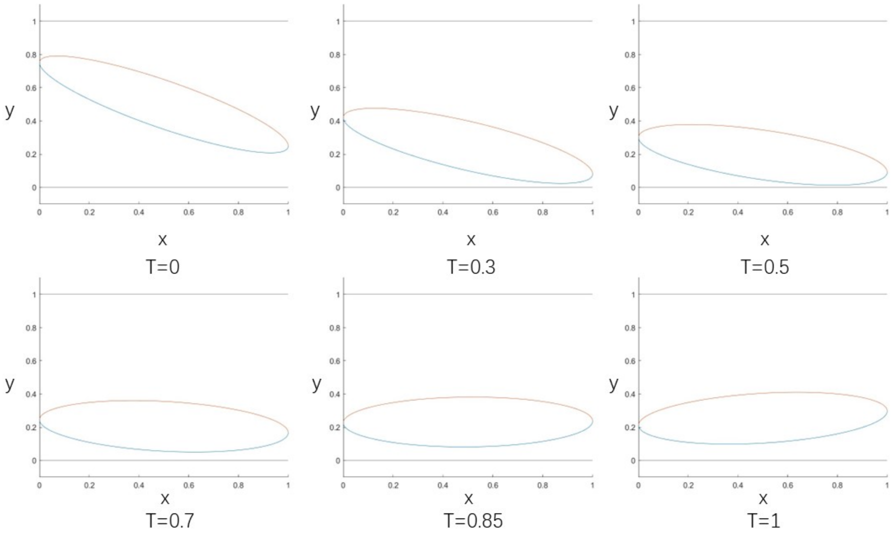

Figure 6.20: Test 11: middle curve of the elliptical particle collides with the bottom wall.

The figure 6.20 shows a situation where the particle is very close to the wall below, but does not collide with it. The smallest distance between the lower body shape and bottom wall is about 0.009 and this happens around time t=0.5. If we keep modifying the initial conditions, we can obtain a case where the particle is infinitely close to the wall below but does not collide with it. This is not the same as a bouncing model. Although the motion trajectories are similar or identical, there are no collisions under this model, just infinitely close. In the bouncing model, if there is an elastic collision, the particles will have an inverted initial velocity after the collision.

In this section, we have added thickness to our particles. Half-parabola and elliptical shaped particles and their trajectories are also tested. From the numerical test results, we conclude that particle can collide not only at the front and back ends, but also at the curved parts of the particles. In addition to collision, being infinitely close to the wall without collision is also a possible motion trajectory. In addition to moving infinitely close to the wall without colliding, we can consider other ways to increase the time that particles spend in the channel. Oscillation of the particle is one possible solution. In the next section, we will carry out further analysis on the oscillation of particle.

6.5 Particle oscillation

In the previous section, we discussed the motion states of a particle with different shapes. It is also verified that almost all parts of the particle can collide with the channel under the present low Reynolds number model. In this section, we focus more on the effect of the particle's center of mass on the particle's motion. In the second section above, we analyzed the influence of the center of mass on the particle motion. See also equation (6.47). Thus in this section, we start with C=0.1 for testing the trajectory of our particle. We use $b = 0.1, C = 0.1, M = 2, I = 0.4, p_0 = 10, p_3 = 0, dx = 0.001, dt = 0.01, t_{max} = 50, \theta(0) = 0.1, \theta'(0) = 0, h(0) = 0.5, h'(0) = 0$ as the initial conditions and we find the results as in figure below.

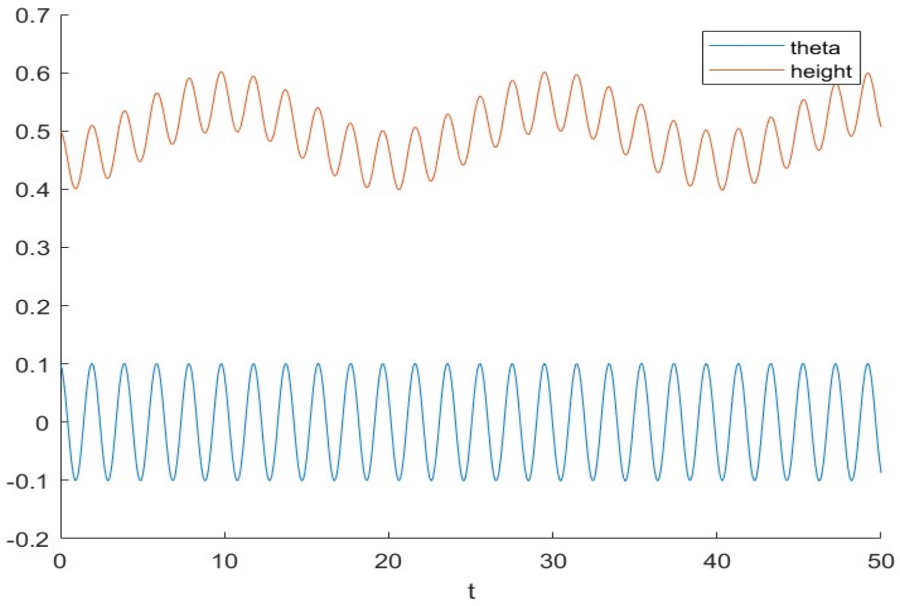

Figure 6.21: Test 12:Oscillation with COM $C = 0.1$.

The difference between this test and the previous tests is that we are able to increase the maximum movement time of the particle to at least 50. The figure shows that the particle has a regular motion trajectory, and the height of the particle is maintained at a relatively stable height. This is consistent with the results of our previous analysis. To verify our analysis, we further modify the initial condition by changing the center of mass from 0.1 to 0.3, and the results are shown below in figure 6.22.

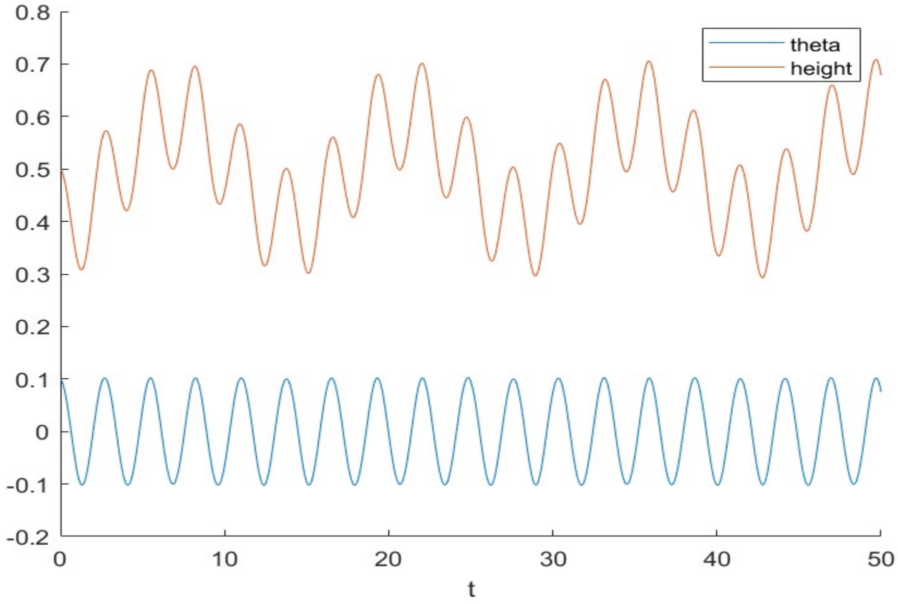

Figure 6.22: Test 12:Oscillation with COM $C = 0.3$.

There is no significant difference in the vibration amplitude of the particle in figure 6.22 compared to the previous tests in figure 6.21. However, the particle does oscillate a little bit less. In addition to this, the amplitude of the particle motion becomes more unstable compared to the previous test, but the particle still does not collide with the channel. According to these two tests, we judge that the 'stability' of the particle motion is related to the center of mass of the particle, and when the center of mass of the particle is closer to 0.5, the particle motion amplitude will be more 'unstable'. In order to test this conjecture, we move the center of mass of the particle closer to 0.5. We use $b = 0.1, C = 0.4, M = 2, I = 0.4, p_0 = 10, p_3 = 0, dx = 0.001, dt = 0.01, t_{max} = 50, \theta(0) = 0.1, \theta'(0) = 0, h(0) = 0.5, h'(0) = 0$ as the initial conditions, and figure below shows the results.

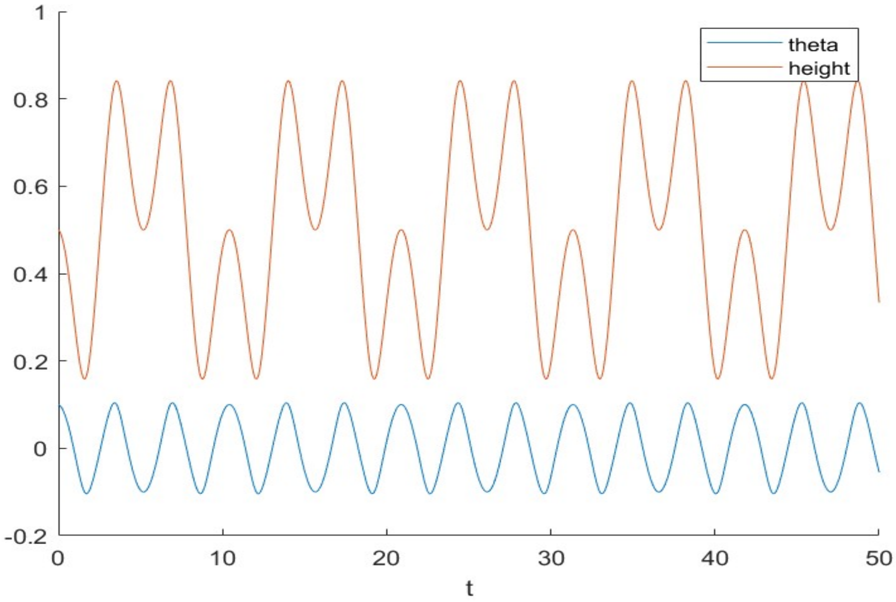

Figure 6.23: Test 12:Oscillation with COM $C = 0.4$.

It can be seen from figure 6.23 that the motion amplitude of the particle increases more, and the particle still maintains a regular motion trajectory; the oscillations here are interesting in being more clearly nonlinear. At the same time, the particle still does not collide with the channel walls. This is in line with our conjecture.

In the analysis of section 6.2, we also infer that the vibration of the particle will disappear when the center of mass of the particle exceeds 0.5. See equation (6.47) again. To test this, we move the center of mass of the particle to 0.6 and show the results in figures 6.24, 6.25.

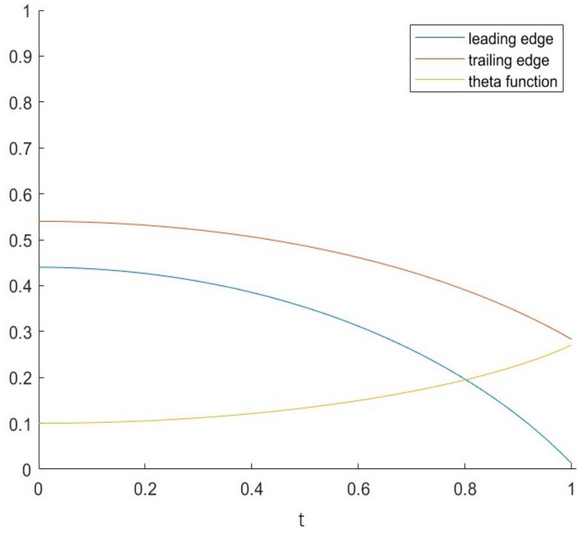

Figure 6.24: Test 13:Elliptical particle's leading edge, trailing edge and angular function with COM $C = 0.6$.

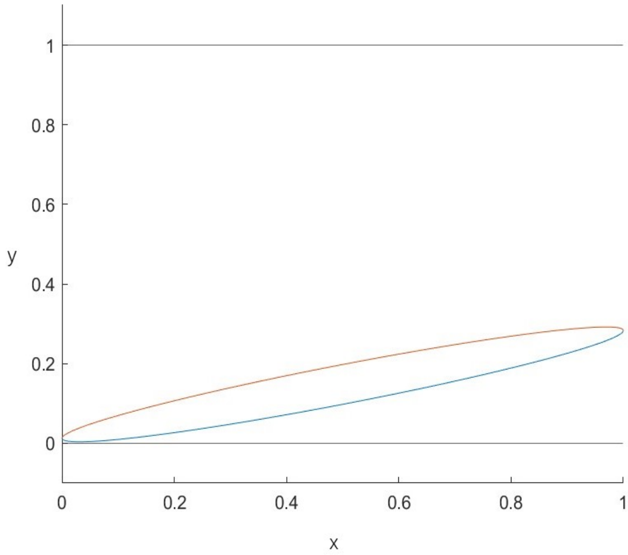

Figure 6.25: Test 13:Collision time for COM $C = 0.6$.

It can be seen from figure 6.24 that the vibration of the particle does disappear, and the particle does collide with the lower channel wall in the process of motion. In addition, we believe that as we continue to move the particle's center of mass further back, the collision time will be shorter. To this end, we set the center of mass of the particle to 0.9.

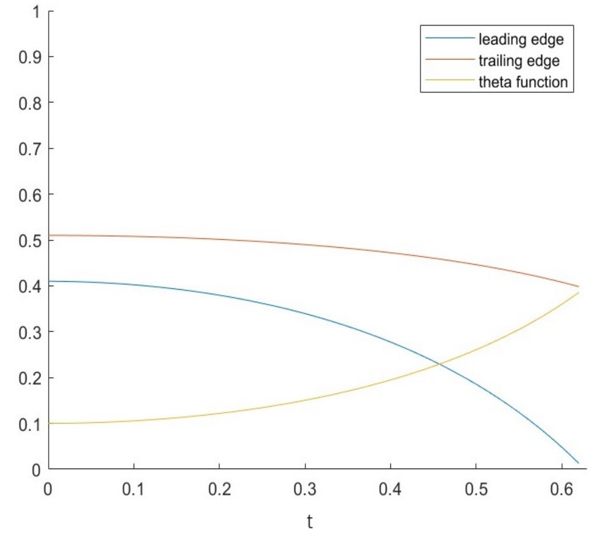

Figure 6.26: Test 14:Elliptical particle's leading edge, trailing edge and angular function with COM $C = 0.9$.

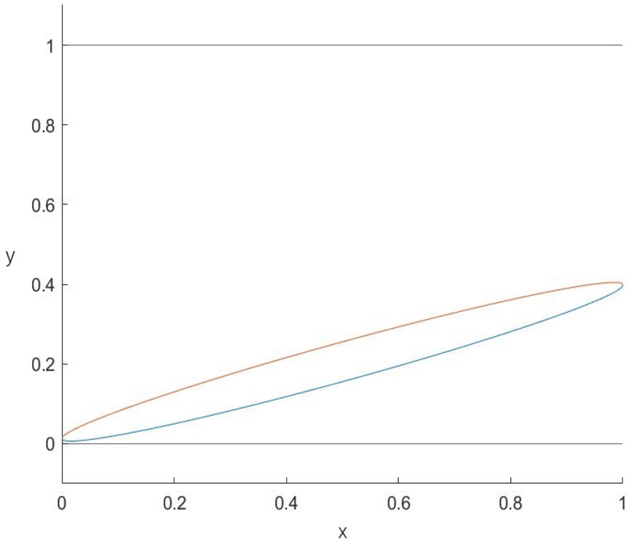

Figure 6.27: Test 13:Collision time for COM $C = 0.9$.

See figures 6.26, 6.27. As expected, the particle collides faster than before.

Also there are no oscillations.

In this section, in order to verify the previous analysis, we have considered numerically the influence of different center of mass positions on the particle motion trajectory. It is concluded that when the location of the center of mass of the particle is less than 0.5 (thus the particle is then front-heavy), the particle will vibrate, and the particle will not collide readily with the channel walls. At the same time, while the center of mass of the particle is less than 0.5, the closer the center of mass is to 0.5, the larger the movement range of the particle is. In addition, when the center of mass of the particle exceeds 0.5, the vibration of the particle disappears and it collides readily (directly) with the channel walls. At this point, if we continue to move the particle's center of mass back towards the trailing edge, the particle collision with the channel walls happens faster.

6.6 Conclusion

In this chapter, we first derived in a fairly classical manner the mass conservation equation and momentum conservation equation as part of the original Navier-Stokes equations. Next we derived the 2D Navier-Stokes equation based on the Cauchy momentum equation, and then we obtained the 2D lubrication theory equation that we needed in the current chapter based on the two-dimensional Navier-Stokes equation. With these inferences in place, we built our zero-thickness particle model and examined the accuracy and properties of the results. We obtained our model data with only a small percentage error approximately from the theoretical asymptotic derivation in terms of period. Then we started to calculate the trajectories of the particle in the zero-thickness model. In order to facilitate more obvious changes in the movements of the particle, we changed the end-pressure difference from 1 to 10 and we kept this in the rest of the study.

After this we added thickness to the particle and tested the trajectories of two different shapes of particle. Finally, we concluded that both the front end and the back end of the particle can collide with the upper and lower walls in this case. In addition to this, the middle-curved part of the particle can also collide with the upper or lower channel walls. Finally, we tested that vibration of the particle obtained in the previous analysis only occurs when the COM (centre of mass location) is less than 0.5, i.e. the COM is moved to be nearer the leading edge than the trailing edge of the particle. Here it is found that when the COM of the particle is between 0 and 0.5, the closer the COM is to 0.5, the larger the vibration range of the particle is. When the COM of the particle is between 0.5 and 1, the closer the COM is to 1, the faster the particle's front end will fall. The result is that the particle cannot move for a long time without colliding with one of the channel walls.

In this chapter, we only studied (computationally to a large extent) the collision model of a single particle. In future research, we suggest consideration of other more complex cases. For example, the rebound model after a particle collision, the multi-particles collision model, the particle stacking model (the particle viscosity is very high, so that the particle will adhere to the wall after collision with the wall, and then other particles will adhere to it, etc.), the cracking model (after particle stacking together, it separates into multi small pieces), and the single-particle melting into several particles.

At the end of this chapter, there are a few points we would like to mention. First of all, the orders of magnitude show that in the model studied in this chapter the density of the particle must be much greater than that of the fluid. Secondly, one potential application of the current type of fluid-body interaction is to ice particles travelling through air rather than water. Thirdly, the effects of moving channel walls could be interesting. Next, the case $\alpha^2 = 0$ (when C = 0.5) remains to be followed through. Finally, note that in the stability analysis we should include 'Real Part', strictly.

Chapter 7

General Conclusions

As far as the work in this thesis is concerned, the question raised of when and how a particle collides with a channel wall is answered by the different models from all chapters. In this research, we started from a model of a single particle crossing a parallel-walled channel. In the beginning of this research, we followed previous researchers' result ([19]) and we set the particle's density as uniformly distributed. With the above assumptions, and others, when we test the particle motion, the particle will always collide with the top or the bottom wall. After some analysis in chapter 2, we found that when the particle's centre of mass location $COM < 1/3$ (which corresponds to a non-uniform distribution of density), oscillations will happen to our particle. When the oscillation happens, we can observe from the figures of our results that the particle will collide much later than for the previous uniformly distributed particle or even does not collide anymore if the initial conditions are carefully chosen. From the end of chapter 2, we provide some more cases about a shape changing model. In addition to these, we started a new chapter about a multi-particles problem. Building on the motion equations of a single particle, we derive the governing equations of the multi-particle motion problem. In this chapter, we assume the presence of overlapping particles. Our aim here is again to avoid collision happening; thus our research stops when the particle(s) collides with the channel wall, or when the particles collide with each other. In all the previous cases, we only considered particles moving in a fixed shape channel. Inspired by the channel shape changing in chapter 3 and [50], we set up the channel shape partly changing with the pressure in chapter 5. Based on the different initial conditions, we obtained a series of collision scenarios.

The tests described above were all carried out at high Reynolds numbers. By contrast, we modelled the fluid-particle interaction involving fluid motion at low Reynolds numbers in chapter 6. In chapter 6, we simulated different particle trajectories. We started from the zero-thickness test. Then we added nonzero thickness to the particle shape and varied the particle shape for comparison. Inspired by the earlier chapter 2, we also wanted to test the oscillation properties of the particle. We found, unlike before, that the oscillation happens when the particle's centre of mass $COM < 1/2$. Moreover, when the oscillations occur for the particle, the particle can move freely in the channel much longer (in time) than in the case of the particle moving without oscillation.

The above points provide a summary of the present thesis. Further overall points are given in the conclusions of the cited papers by the author and collaborators. In addition, the author believes that the study of the contained particle motion can be further advanced in terms of the several other significant aspects. For example, in most of the tests presented in this thesis, the particle trajectories stop at the time of a collision. In reality however, after such collisions, the particle continues to move. Alternatively in the icing context the particle may adhere to the wall. The particle can even split into two or more particles. At the same time, multiple particles may also collide with each other, affecting each other's motion trajectories. Multi-particle motion is more complicated and may cause more serious damage to the channel wall. Therefore starting from the rebound model of regular particle(s) may be an interesting and useful study. Appendix A provides a very basic model of the rebound of a particle after collision. In the author's opinion, it is difficult to determine the collision point and rebound trajectory of a particle after adding in the thickness of the particle. In addition, in Chapter 5, we only set a part of the channel to be deformed under pressure. Therefore, in future studies, it would be interesting to set the deformation of the whole channel to be influenced by the pressure.

Appendix A

Single particle bouncing model

A.1 Model creation

With respect to particle(s) movement problem, there must be some collisions on the particles. Either the collisions between the particle(s) or the collisions between the particle(s) and the wall. Because we would like to study more details about this process. We may have to go back to the single particle movement problem first.

In the previous assumptions, we assume our particle is a long and thin ellipse. As a consequence, the thickness of the particle does not influence the inertia of the whole particle during the movement. Based on above assumptions, we create a more ‘egregious’ model at the collision point as below,

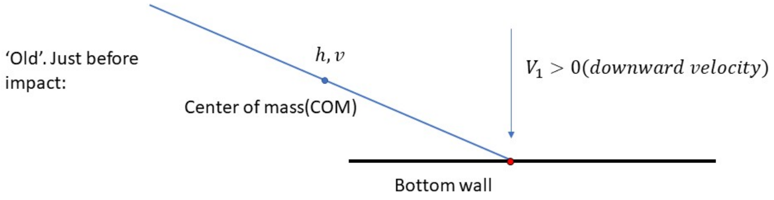

Figure A.1: The moment before the collision

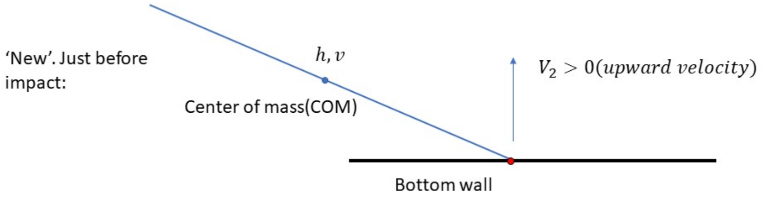

Figure A.2: The moment after the collision

Above two figures A.1, A.2 are the moments before and after the collision. In this model, we introduce several new variables. Here (h_{new},θ_{new})=(h_{old},θ_{old}), but we expect the velocities (h'_{new},θ'_{new})=(h'_{old},θ'_{old}). We also know $V_1 = -h'_{old} - b\theta'_{old}$, where b is the distance between the COM and the trailing edge. During the test, we still use the previous initial conditions to do the test such as $a = 0.3, b = 0, COM = 0.5, h(0) = 0, \frac{dh(0)}{dt} = 0, \theta(0) = -0.1, \frac{d\theta(0)}{dt} = 0, M = 2, I = 0.01$. The next key point is to solve the initial conditions after the collision. Recalling the previous core equations,

$$Mh_{tt} = \int_0^1 (p_1 - p_2)\,dx, \quad I\theta_{tt} = \int_0^1 (x - \frac{1}{2})(p_1 - p_2)\,dx. \tag{A.1}$$

We do the integral to both of the equations with respect to dt and we can have the equations as below,

$$\text{Upward momentum} : P = M(h'_{new} - h'_{old}). \tag{A.2a}$$

$$\text{Angular momentum} : Pc_1 = I(\theta'_{new} - \theta'_{old}). \tag{A.2b}$$

$$\text{Local relation} : V_2 = eV_1. \tag{A.2c}$$

$$\text{Definition for V}_2 : V_2 = h'_{new} + b\theta'_{new}. \tag{A.2d}$$

With above 4 equations, we can easily solve the 4 unknown variables P, h'_{new}, θ'_{new}, V_2. Because we assume the collision happens at the trailing edge, which means $x = 1$. Thus we should have $c_1 = 0.5$ during the calculation.

A.2 particle with zero-thickness bouncing model

In the previous research, we did a lot of research on single particle motion and we stopped when our particle collided with the wall of the channel. In this chapter, we would like to do more research on the single particle bouncing model.

Because we use the zero-thickness model to do the test. Thus, the collisions only happen at either the trailing edge or the leading edge. We start to think about the trailing edge collision case. We use $\beta = 0$, $c = 0.5$, $M = 2$, $I = 0.01$, $\theta(0) = -0.1$, $\theta'(0) = 0$, $h(0) = 0.3$, $h'(0) = 0$, $e = 0.3$ as the initial conditions and results are shown in figure A.3

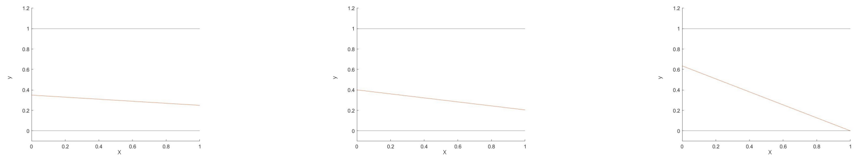

(a) Particle position at t=0 ($e = 0.3$)
(b) Particle position at t=0.23 ($e = 0.3$)
(c) Particle position at t=0.452 ($e = 0.3$)

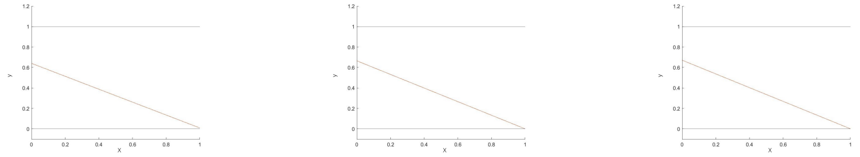

(d) Particle position at t=0.502 ($e = 0.3$)
(e) Particle position at t=0.542 ($e = 0.3$)
(f) Particle position at t=0.557 ($e = 0.3$)

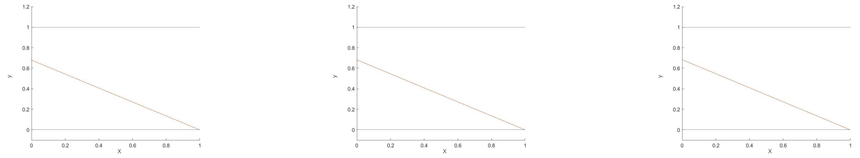

(g) Particle position at t=0.569 ($e = 0.3$)
(h) Particle position at t=0.575 ($e = 0.3$)
(i) Particle position at t=0.579 ($e = 0.3$)

Figure A.3: Particle motion with $e = 0.3$

Figure A.3 shows the bouncing motion of the particle movement. A.3a-A.3c shows the first collision between the particle and bottom wall. A.3d and A.3e shows the particle bouncing back after collision and collide again with the bottom wall. A.3f and A.3g shows the third bounce and collision. While A.3h and A.3i represents the forth bounce and collision. After the forth bounce and collision, the bouncing height of the particle is too small to calculate and all the tests stopped. The figure A.4 shows the zoom in case for figure A.3d which is the first bouncing.

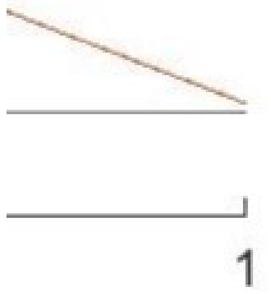

Figure A.4: Zoom in figure for figure A.3d

From the figure A.4, there is a very tiny gap between the particle's trailing edge and the bottom wall. But the bouncing height is not high enough to be observed easily. Thus, we keep all the initial conditions same and change the values of elastic coefficient e. Let the whole bouncing process slightly change the collision from inelastic to elastic. Since our initial conditions have not changed, the trajectory of the particle's first collision is the same as the A.3a to A.3c. The figures below show the particle motion after first collision with $e = 0.5$.

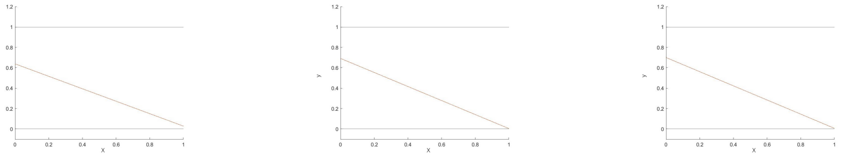

(a) Particle position at t=0.542 ($e = 0.5$) **(b)** Particle position at t=0.602 ($e = 0.5$) **(c)** Particle position at t=0.632 ($e = 0.5$)

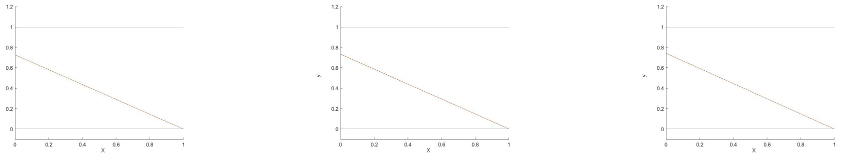

(d) Particle position at t=0.662 ($e = 0.5$) **(e)** Particle position at t=0.674 ($e = 0.5$) **(f)** Particle position at t=0.685 ($e = 0.5$)

Figure A.5: Particle motion with $e = 0.5$

The figure A.5 shows the particle motion after first collision. While the particle motion for the first collision is same as figure A.3a to A.3c. A.5a and A.5b represents the first bounce and second collision. A.5c and A.5d are for the second bounce and third collision respectively. A.5e and A.5f are for the third bounce and forth collision respectively. From the figures we notice that, because we use a larger elastic coefficient, the particle bounce higher than $e = 0.3$ case. With a higher bounce height, the particle can move for a longer time. This test stops at the bounce height is small enough which is the forth collision.

For next test, we increase the elastic coefficient to $e = 0.7$ and results are shown in figure A.6 Same as last test, we present the particle motion after first collision.

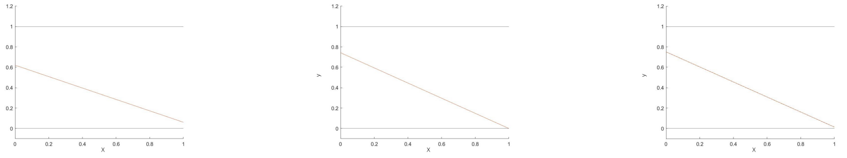

(a) Particle position at t=0.572 ($e = 0.7$) **(b)** Particle position at t=0.682 ($e = 0.7$) **(c)** Particle position at t=0.722 ($e = 0.7$)

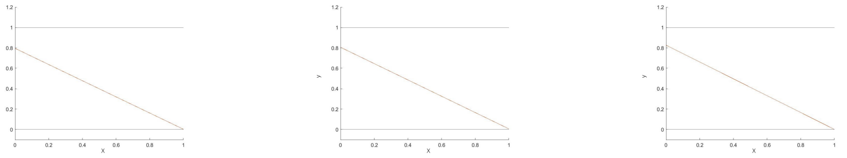

(d) Particle position at t=0.762 ($e = 0.7$) **(e)** Particle position at t=0.778 ($e = 0.7$) **(f)** Particle position at t=0.795 ($e = 0.7$)

Figure A.6: Particle motion with $e = 0.7$

A.6a and A.6b are for the first bounce and second collision.A.6c and A.6d show the second bounce and third collision. A.6e and A.6f represent the third bounce and forth collision. With the same reason, the bounce height is too small, we stop the test for $e = 0.7$ case.

For the next test, we keep increase the elastic coefficient to $e = 1$ which is the elastic collision. The results are shown below,

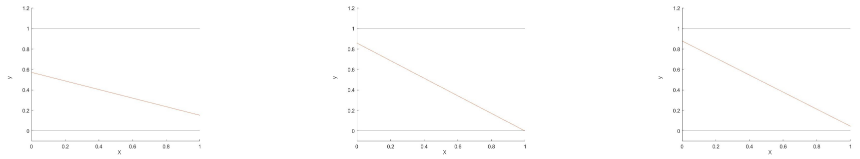

(a) Particle position at t=0.652 ($e = 1$) **(b)** Particle position at t=0.852 ($e = 1$) **(c)** Particle position at t=0.922 ($e = 1$)

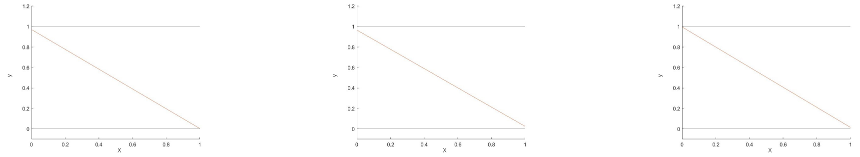

(d) Particle position at t=0.953 ($e = 1$) **(e)** Particle position at t=0.963 ($e = 1$) **(f)** Particle position at t=0.973 ($e = 1$)

Figure A.7: Particle motion with $e = 1$

Figure A.7 shows the particle motion after elastic collision. Same as before, all the elastic collision happens between the particle and the bottom wall. Figure A.7a and A.7b shows the particle motion after first collision. Figure A.7c and A.7d shows the particle motion after second collision. Figure A.7e and A.7f shows the particle motion after third collision. But different as previous cases, this test stops because the leading edge of the particle collide with the top wall.

This part of the research gives 4 cases about zero-thickness particle bouncing motion. We start with $e = 0.3$. Because when we use a smaller value of e. The bounce height is too small to be observed. Even with $e = 0.3$, the second and the third bounces are roughly been observed. Then we gradually increase the value of e. The particle bounce height are gradually increasing as well.At the same time, the particle motion ”till the forth collision” becomes longer. Also another interesting thing is when we increase the elastic parameter to $e = 1$ which means the whole motion of the particle bounces are elastic collisions. Instead of colliding with the bottom wall, the particle collide with the top wall. In the future, there could be more tests, for example, after collision with the top wall, the particle collide with the bottom wall again. Or we can add thickness to the particle. Because in this appendix, all the collision happens at the leading and trailing edge. If we add some thickness to the particle, the collision may happen at the upper edge or lower edge of the particle. Besides these two cases, make the particle becoming a front-loaded particle or back-loaded particle is also interesting.

Appendix B

Explanations for ignoring the effects of viscosity and gravity

This research works in non-dimensional scaled quantities, which are are used in the frame moving with the particle at speed U^*, such that

$$\begin{aligned}
&x^* = L^* \times x, u^* = U^* \times u;\\
&y^* = \varepsilon^* \times y, v^* = U^* \times \varepsilon v;\\
&t^* = \frac{L^* \times t}{U^*}, p^* = \rho^* \times (U^*)^2 p;\\
&{g_1}^* = g_x, {g_2}^* = g_y.
\end{aligned} \tag{B.1}$$

where $\varepsilon = \frac{d^*}{L^*}$, d^* represents the gap width and L^* represents the particle length and $L^* \gg d^*$. Recalling from the Navier-Stokes equations expressed in Cartesian coordinates in two spatial dimensions (x, y) and time t,

$$\rho(\frac{\partial u_x}{\partial t} + u_x \frac{\partial u_x}{\partial x} + u_y \frac{\partial u_x}{\partial y}) = -\frac{\partial p}{\partial x} + \mu(\frac{\partial^2 u_x}{\partial x^2} + \frac{\partial^2 u_x}{\partial y^2}) + \rho g_x, \tag{B.2}$$

$$\rho(\frac{\partial u_y}{\partial t} + u_x \frac{\partial u_y}{\partial x} + u_y \frac{\partial u_y}{\partial y}) = -\frac{\partial p}{\partial y} + \mu(\frac{\partial^2 u_y}{\partial x^2} + \frac{\partial^2 u_y}{\partial y^2}) + \rho g_y. \tag{B.3}$$

where ρ is the density, u is the flow velocity, p is the pressure, t is time, g represents body accelerations which can be treated as gravity, μ is dynamic viscosity.

Next, we substitute the above non-dimensional scaled quantities into above x-dimensional Navier-Stokes equation,

$$\rho^*(\frac{\partial u}{\partial t}+u\frac{\partial u}{\partial x}+v\frac{\partial u}{\partial y})\times\frac{U^{*2}}{L^*}=-\rho^*\frac{\partial p}{\partial x}\times\frac{U^{*2}}{L^*}+\mu(\frac{\partial^2 u}{\partial x^2}+\frac{\partial^2 u}{\partial y^2})\times\frac{U^*}{L^{*2}}+\rho {g_1}^*, \tag{B.4}$$

After simplifying the equation, we get

$$\frac{\partial u}{\partial t}+u\frac{\partial u}{\partial x}+v\frac{\partial u}{\partial y}=-\frac{\partial p}{\partial x}+\frac{\mu}{\rho^*U^*L^*}(\frac{\partial^2 u}{\partial x^2}+\frac{\partial^2 u}{\partial y^2})+\frac{{g_1}^*L^*}{U^{*2}}. \tag{B.5}$$

In the equation (B.5), $Re=\frac{\rho^*U^*L^*}{\mu}$ and $Fr^2=\frac{U^{*2}}{{g_1}^*L^*}$ which are estimated in a recent work [23] with $Re=10^2\sim 10^3$ and $Fr\sim 10^6$. In consequence, we can formally ignore the last two terms in equation (B.5), and equation (B.5) can be simplified into x-momentum equation as below,

$$\frac{\partial u}{\partial t}+u\frac{\partial u}{\partial x}+v\frac{\partial u}{\partial y}=-\frac{\partial p}{\partial x}. \tag{B.6}$$

Similarly, we substitute non-dimensional scaled quantities into the y-dimensional Navier-Stokes equations and use the same steps to simplify the equation to get,

$$\frac{\partial v}{\partial t}+u\frac{\partial v}{\partial x}+v\frac{\partial v}{\partial y}=-\frac{\partial p}{\partial y}. \tag{B.7}$$

In the model of this research, the assumptions require the relevant length scale along the walls is much greater than the height between the walls which causes ε to be a small constant. Thus, with the assumptions in the previous non-dimensional scaled quantities, we can find the velocity v can be neglected. We can use this condition in equation (B.7) to get,

$$0=-\frac{\partial p}{\partial y}. \tag{B.8}$$

From equation (B.8), we can deduce the pressure function only with respect to (x,t) which is the same as we got in equation (4.4c).

Appendix C

Deductions for oscillations

For small β (=$\varepsilon\beta$ say, the particle thickness is very small) and small disturbances or perturbations of order ε, where the constant ε is asymptotically small in strict terms, we can rescale the parameters and functions as below,

$$(h,\theta,p_n)=\varepsilon(h^E,\theta^E,{p_n}^E)+\dots, \tag{C.1a}$$

$$(f^-,f^+,H_1,H_2)=(\alpha,\alpha,\alpha,1-\alpha)+\varepsilon({f^-}^E,{f^+}^E,{H_1}^E,{H_2}^E)+\dots, \tag{C.1b}$$

$$(d_1,d_2)=(\alpha,1-\alpha)+\varepsilon({d_1}^E,{d_2}^E)+\dots, \tag{C.1c}$$

where these functions or parameters are similar to the functions or parameters introduced in chapter 4. In the functions, time t and the constants α and c are assumed to be of order unity. The unknowns with superscript 'E' are taken to be of O(1). Then we substituting these back into the system and can have the pressure difference as below,

$$ {p_1}^E-{p_2}^E=A_1*x^{\frac{1}{2}}(1-x)^{\frac{1}{2}}+A_2*(x-1)\theta^E, \tag{C.2}$$

where $A_1=-\beta^E*\frac{1-2\alpha}{\alpha(1-\alpha)}$, $A_2=\frac{1}{\alpha(1-\alpha)}$ are known constants. After substituting the pressure difference into the particle motion functions we have the relations as below,

$$M\frac{d^2h^E}{dt^2}=\int_0^1 A_1*x^{\frac{1}{2}}(1-x)^{\frac{1}{2}}+A_2*(x-1)\theta^E dx, \tag{C.3}$$

$$I\frac{d^2\theta^E}{dt^2}=\int_0^1 (x-c)(A_1*x^{\frac{1}{2}}(1-x)^{\frac{1}{2}}+A_2*(x-1)\theta^E)dx. \tag{C.4}$$

At the same time, we can rewrite the functions as below,

$$M\frac{d^2h^E}{dt^2} = B_1 + B_2\theta^E, \tag{C.5}$$

$$I\frac{d^2\theta^E}{dt^2} = C_1 + C_2\theta^E, \tag{C.6}$$

where B_1, B_2, C_1, C_2 are constants. We can use Beta function and the factorial of a fraction to solve these equations to find out the constant values as below,

$$B_1 = \frac{\pi}{8}A_1, B_2 = -\frac{1}{2}A_2, C_1 = (\frac{\pi}{16} - \frac{\pi}{8}c)A_1, C_2 = \frac{1}{2}(c - \frac{1}{3})A_2. \tag{C.7}$$

From the parameter B_2, we notice that the A_2 is positive for $0 < c < 1$. Therefore, if we choose $c < \frac{1}{3}$, C_2 will be a negative value. This will cause the solution of θ from equation C.6 shows that there will be an oscillation exist.

Bibliography

[1] Roger W Gent, Nicholas P Dart, and James T Cansdale. Aircraft icing. *Philosophical Transactions of the Royal Society of London. Series A: Mathematical, Physical and Engineering Sciences*, 358(1776):2873–2911, 2000.

[2] Richard Purvis and Frank T Smith. Improving aircraft safety in icing conditions. *UK success stories in industrial mathematics*, pages 145–151, 2016.

[3] Ellen Norde. *Eulerian method for ice crystal icing in turbofan engines*. PhD thesis, University of Twente, 2017.

[4] P Bartlett. Development of a new model of ice accretion on aircraft. In *Proceedings of 9th International Workshop on Atmospheric Icing on Structures, Chester, UK*, 2000.

[5] Peter D Hicks and Richard Purvis. Air cushioning and bubble entrapment in three-dimensional droplet impacts. *Journal of Fluid Mechanics*, 649:135–163, 2010.

[6] Peter D Hicks and Richard Purvis. Liquid–solid impacts with compressible gas cushioning. *Journal of fluid mechanics*, 735:120–149, 2013.

[7] R Purvis and FT Smith. Air-water interactions near droplet impact. *European Journal of Applied Mathematics*, 15(6):853–871, 2004.

[8] Timothy W Secomb, R Skalak, N Özkaya, and JF Gross. Flow of axisymmetric red blood cells in narrow capillaries. *Journal of Fluid Mechanics*, 163:405–423, 1986.

[9] Y Iguchi and K Kimura. A case of brain embolism during catheter embolisation of head arteriovenous malformation. what is the mechanism of stroke? *Journal of Neurology, Neurosurgery & Psychiatry*, 78(1):81–81, 2007.

[10] Maureen Andrew, Michelle David, Gabrielle deVeber, and Lu Ann Brooker. Arterial thromboembolic complications in paediatric patients. *Thrombosis and haemostasis*, 78(07):715–725, 1997.

[11] Frank T Smith and Andrew S Ellis. On interaction between falling bodies and the surrounding fluid. *Mathematika*, 56(1):140–168, 2010.

[12] James Feng, Howard H Hu, and Daniel D Joseph. Direct simulation of initial value problems for the motion of solid bodies in a newtonian fluid part 1. sedimentation. *Journal of Fluid Mechanics*, 261:95–134, 1994.

[13] Felipe A. González, Marcela A. Cruchaga, and Diego J. Celentano. Analysis of Flow Past Oscillatory Cylinders Using a Finite Element Fixed Mesh Formulation. *Journal of Fluids Engineering*, 139(8):081202, 05 2017.

[14] C. P. Jackson. A finite-element study of the onset of vortex shedding in flow past variously shaped bodies. *Journal of Fluid Mechanics*, 182:23–45, 1987.

[15] Ellen M Jolley, Ryan A Palmer, and Frank T Smith. Particle movement in a boundary layer. *Journal of Engineering Mathematics*, 128(1):6, 2021.

[16] Ellen M Jolley, Thuy Duong Dang, and Frank T Smith. Melting of wall-mounted ice in shear flow. *Proceedings of the Royal Society A*, 480(2286):20230688, 2024.

[17] Frank T Smith and Phillip L Wilson. Fluid-body interactions: clashing, skimming, bouncing. *Philosophical Transactions of the Royal Society A: Mathematical, Physical and Engineering Sciences*, 369(1947):3007–3024, 2011.

[18] Frank T Smith and Kevin Liu. Flooding and sinking of an originally skimming body. *Journal of Engineering Mathematics*, 107:37–60, 2017.

[19] Samire Balta and Frank T Smith. Fluid flow lifting a body from a solid surface. *Proceedings of the Royal Society A*, 474(2219):20180286, 2018.

[20] Frank T Smith and Edward R Johnson. Movement of a finite body in channel flow. *Proceedings of the Royal Society A: Mathematical, Physical and Engineering Sciences*, 472(2191):20160164, 2016.

[21] Frank T Smith. Free motion of a body in a boundary layer or channel flow. *Journal of Fluid Mechanics*, 813:279–300, 2017.

[22] Frank Smith and Ryan Palmer. A freely moving body in a boundary layer: nonlinear separated-flow effects. *Applied Ocean Research*, 85:107–118, 2019.

[23] Ryan A Palmer and Frank T Smith. A body in nonlinear near-wall shear flow: impacts, analysis and comparisons. *Journal of Fluid Mechanics*, 904:A32, 2020.

[24] FT Smith and MA Jones. One-to-few and one-to-many branching tube flows. *Journal of Fluid Mechanics*, 423:1–31, 2000.

[25] S Frecentese, LP Argani, AB Movchan, NV Movchan, G Carta, and ML Wall. Waves and fluid–solid interaction in stented blood vessels. *Proceedings of the Royal Society A: Mathematical, Physical and Engineering Sciences*, 474(2209):20170670, 2018.

[26] Johan Roenby and Hassan Aref. Chaos in body–vortex interactions. *Proceedings of the Royal Society A: Mathematical, Physical and Engineering Sciences*, 466(2119):1871–1891, 2010.

[27] Kevin Liu and Frank T Smith. Collisions, rebounds and skimming. *Philosophical Transactions of the Royal Society A: Mathematical, Physical and Engineering Sciences*, 372(2020):20130351, 2014.

[28] Frank Thomas Smith. Blade-wake interactions and rotary boundary layers. *Proceedings of the Royal Society of London. Series A: Mathematical, Physical and Engineering Sciences*, 452(1949):1301–1329, 1996.

[29] Nick Ovenden, Frank Smith, and Guo Xiong Wu. The effects of nonsymmetry in a branching flow network. *Journal of Engineering Mathematics*, 63:213–239, 2009.

[30] R Purvis and FT Smith. Planar flow past two or more blades in ground effect. *Quarterly Journal of Mechanics and Applied Mathematics*, 57(1):137–160, 2004.

[31] Médéric Argentina and L Mahadevan. Fluid-flow-induced flutter of a flag. *Proceedings of the National Academy of Sciences*, 102(6):1829–1834, 2005.

[32] Frank T Smith, Samire Balta, Kevin Liu, and Edward R Johnson. On dynamic interactions between body motion and fluid motion. *Mathematics Applied to Engineering, Modelling, and Social Issues*, pages 45–89, 2019.

[33] Eric Loth and Andrew J Dorgan. An equation of motion for particles of finite Reynolds number and size. *Environmental fluid mechanics*, 9:187–206, 2009.

[34] Nanda Kishore and Sai Gu. Wall effects on flow and drag phenomena of spheroid particles at moderate Reynolds numbers. *Industrial & engineering chemistry research*, 49(19):9486–9495, 2010.

[35] Vincent Loisel, Micheline Abbas, Olivier Masbernat, and Eric Climent. The effect of neutrally buoyant finite-size particles on channel flows in the laminar-turbulent transition regime. *Physics of Fluids*, 25(12), 2013.

[36] Minsoo Han, Chongyoup Kim, Minchul Kim, and Soonchil Lee. Particle migration in tube flow of suspensions. *Journal of rheology*, 43(5):1157–1174, 1999.

[37] Bastian Krause, Birk Liedmann, Jens Wiese, Siegmar Wirtz, and Viktor Scherer. Coupled three dimensional dem–cfd simulation of a lime shaft kiln—calcination, particle movement and gas phase flow field. *Chemical Engineering Science*, 134:834–849, 2015.

[38] Frank T Smith, Ellen M Jolley, and Ryan A Palmer. On modelling fluid/body interactions, impacts and lift-offs. *Acta Mechanica Sinica*, 39(5):323019, 2023.

[39] David M Davis. The hydrodynamics of the upper urinary tract (urodynamics). *Annals of surgery*, 140(6):839–849, 1954.

[40] CJ Cawthorn and NJ Balmforth. Contact in a viscous fluid. part 1. a falling wedge. *Journal of fluid mechanics*, 646:327–338, 2010.

[41] Andrew Wilkinson, Marc Pradas, and Michael Wilkinson. Lubrication dynamics of a settling plate. *Journal of Fluid Mechanics*, 977:A28, 2023.

[42] Dominic Vella, Ho-Young Kim, and L Mahadevan. The wall-induced motion of a floating flexible train. *Journal of Fluid Mechanics*, 502:89–98, 2004.

[43] LD Pruessner. *Waves on flexible surfaces*. PhD thesis, UCL (University College London), 2013.

[44] Kiran Singh, John R Lister, and Dominic Vella. A fluid-mechanical model of elastocapillary coalescence. *Journal of fluid mechanics*, 745:621–646, 2014.

[45] JSB Gajjar and P Sibanda. The hydrodynamic stability of channel flow with compliant boundaries. *Theoretical and computational fluid dynamics*, 8(2):105–129, 1996.

[46] Christopher Davies and Peter W Carpenter. Instabilities in a plane channel flow between compliant walls. *Journal of Fluid Mechanics*, 352:205–243, 1997.

[47] D Takagi and NJ Balmforth. Peristaltic pumping of rigid objects in an elastic tube. *Journal of fluid mechanics*, 672:219–244, 2011.

[48] Feng Xu, John Billingham, and Oliver E Jensen. Resonance-driven oscillations in a flexible-channel flow with fixed upstream flux and a long downstream rigid segment. *Journal of Fluid Mechanics*, 746:368–404, 2014.

[49] PW Carpenter and AD Garrad. The hydrodynamic stability of flow over kramer-type compliant surfaces. part 1. tollmien-schlichting instabilities. *Journal of Fluid Mechanics*, 155:465–510, 1985.

[50] Luisa Pruessner and Frank Smith. Enhanced effects from tiny flexible in-wall blips and shear flow. *Journal of Fluid Mechanics*, 772:16–41, 2015.

[51] BK Chi and LG Leal. A theoretical study of the motion of a viscous drop toward a fluid interface at low Reynolds number. *Journal of Fluid Mechanics*, 201:123–146, 1989.

[52] Michael Manga and HA Stone. Low Reynolds number motion of bubbles, drops and rigid spheres through fluid–fluid interfaces. *Journal of Fluid Mechanics*, 287:279–298, 1995.

[53] Francis P Bretherton. The motion of rigid particles in a shear flow at low Reynolds number. *Journal of Fluid Mechanics*, 14(2):284–304, 1962.

[54] RG Cox and SG Mason. Suspended particles in fluid flow through tubes. *Annual Review of Fluid Mechanics*, 3(1):291–316, 1971.

[55] Erik J Carboni, Brice H Bognet, Grant M Bouchillon, Andrea L Kadilak, Leslie M Shor, Michael D Ward, and Anson WK Ma. Direct tracking of particles and quantification of margination in blood flow. *Biophysical Journal*, 111(7):1487–1495, 2016.

[56] Rhonda Prisby, Jean Ross, Lynn Opdenaker, Mary Ann McLane, Seungyong Lee, Xiangle Sun, and Sophie Guderian. Discovery of a bone-like blood particle in the peripheral circulation of humans and rodents. *Microcirculation*, 26(8):e12579, 2019.

[57] Ryan Palmer, Ian Roberts, Richard Moser, Colin Hatch, and Frank Smith. Non-spherical particle trajectory modelling for ice crystal conditions. Technical report, SAE Technical Paper, 2019.

[58] IJ Hewitt, NJ Balmforth, and JN McElwaine. Continual skipping on water. *Journal of fluid mechanics*, 669:328, 2011.

[59] J-M Foucaut and M Stanislas. Experimental study of saltating particle trajectories. *Experiments in Fluids*, 22(4):321–326, 1997.

[60] P Rr Owen. Saltation of uniform grains in air. *Journal of Fluid Mechanics*, 20(2):225–242, 1964.

[61] Arshad Kudrolli, Geoffroy Lumay, Dmitri Volfson, and Lev S Tsimring. Swarming and swirling in self-propelled polar granular rods. *Physical review letters*, 100(5):058001, 2008.

[62] Panayiotis Diplas, Clint L Dancey, Ahmet O Celik, Manousos Valyrakis, Krista Greer, and Tanju Akar. The role of impulse on the initiation of particle movement under turbulent flow conditions. *Science*, 322(5902):717–720, 2008.

[63] Arshad Kudrolli, David Scheff, and Benjamin Allen. Critical shear rate and torque stability condition for a particle resting on a surface in a fluid flow. *Journal of Fluid Mechanics*, 808:397–409, 2016.

[64] M Sami Akoz and M Salih Kirkgoz. Numerical and experimental analyses of the flow around a horizontal wall-mounted circular cylinder. *Transactions of the Canadian Society for Mechanical Engineering*, 33(2):189–215, 2009.

[65] Mikko Virmavirta, Juha Kivekäs, and Paavo V Komi. Take-off aerodynamics in ski jumping. *Journal of Biomechanics*, 34(4):465–470, 2001.

[66] MC Miller, IN McCave, and P_D Komar. Threshold of sediment motion under unidirectional currents. *Sedimentology*, 24(4):507–527, 1977.

[67] Kevin Liu and Frank T Smith. A smoothly curved body skimming on shallow water. *Journal of Engineering Mathematics*, 128(1):1–15, 2021.

[68] Frank T Smith and Kevin Liu. Three-dimensional evolution of body and fluid motion near a wall. *Theoretical & Computational Fluid Dynamics*, 36:969—-992, 2022.

[69] FT Smith and P Servini. Channel flow past a near-wall body. *The Quarterly Journal of Mechanics and Applied Mathematics*, 72(3):359–385, 2019.

[70] Ellen M Jolley. PhD thesis, University College London, 2024.

[71] Ryan A Palmer and Frank T Smith. When a small thin two-dimensional body enters a viscous wall layer. *European Journal of Applied Mathematics*, 31(6):1002–1028, 2020.

[72] Samire Balta. *On fluid-body and fluid-network interactions*. PhD thesis, University College London, 2018.

[73] Ellen M Jolley and Frank T Smith. Dynamics of an ice particle submerged in water. *Submitted to Journal of Fluid Mechanics (Rapids)*, 2023.

[74] Qingsong Liu, S Yazar, and Frank T Smith. On interaction between freely moving bodies and fluid in a channel flow. *Theoretical and Applied Mechanics Letters*, 13(1):100413, 2022.

[75] Andrew Shaw Ellis. *Modelling chute delivery of grains in a food-sorting process*. University of London, University College London (United Kingdom), 2007.

[76] Hermann Schlichting and Klaus Gersten. *Boundary-layer theory*. Springer, 2016.

[77] Ellen M Jolley and Frank T Smith. A heavy body translating in a boundary layer:‘crash’,‘fly away’and ‘bouncing’responses. *Journal of Fluid Mechanics*, 936:A37, 2022.

[78] Peter S Stewart, Sarah L Waters, and Oliver E Jensen. Local and global instabilities of flow in a flexible-walled channel. *European Journal of Mechanics-B/Fluids*, 28(4):541–557, 2009.

[79] Jeffrey W Banks, T Aslam, and William J Rider. On sub-linear convergence for linearly degenerate waves in capturing schemes. *Journal of Computational Physics*, 227(14):6985–7002, 2008.

[80] Ryan B Bond, Curtis C Ober, Patrick M Knupp, and Steven W Bova. Manufactured solution for computational fluid dynamics boundary condition verification. *AIAA journal*, 45(9):2224–2236, 2007.

[81] C Yu Wen. Mechanics of fluidization. In *Fluid Particle Technology, Chem. Eng. Progress. Symposium Series*, volume 62, pages 100–111, 1966.

[82] Feng Chen, Eric C Drumm, and Georges Guiochon. Prediction/verification of particle motion in one dimension with the discrete-element method. *International journal of geomechanics*, 7(5):344–352, 2007.

[83] Aniruddha Choudhary, Christopher J Roy, Jean-François Dietiker, Mehrdad Shahnam, Rahul Garg, and Jordan Musser. Code verification for multiphase flows using the method of manufactured solutions. *International Journal of Multiphase Flow*, 80:150–163, 2016.

[84] Rahul Garg, Janine Galvin, Tingwen Li, and Sreekanth Pannala. Open-source mfix-dem software for gas–solids flows: Part i—verification studies. *Powder Technology*, 220:122–137, 2012.

[85] Aytekin Gel, Avinash Vaidheeswaran, Jordan Musser, and Charles H Tong. Toward the development of a verification, validation, and uncertainty quantification framework for granular and multiphase flows—part 1: screening study and sensitivity analysis. *Journal of Verification, Validation and Uncertainty Quantification*, 3(3):031001, 2018.

[86] Philip M Gresho and Stevens T Chan. On the theory of semi-implicit projection methods for viscous incompressible flow and its implementation via a finite element method that also introduces a nearly consistent mass matrix. part 2: Implementation. *International journal for numerical methods in fluids*, 11(5):621–659, 1990.

[87] Alberto Di Renzo and Francesco Paolo Di Maio. Comparison of contact-force models for the simulation of collisions in dem-based granular flow codes. *Chemical engineering science*, 59(3):525–541, 2004.

[88] Patrick J Roache and Stanly Steinberg. Symbolic manipulation and computational fluid dynamics. *AIAA journal*, 22(10):1390–1394, 1984.

[89] Christopher J Roy. Review of code and solution verification procedures for computational simulation. *Journal of Computational Physics*, 205(1):131–156, 2005.

[90] Avinash Vaidheeswaran, Jordan Musser, and Mary Ann Clarke. Verification and validation of mfix-pic. Technical report, National Energy Technology Laboratory (NETL), Pittsburgh, PA, Morgantown, WV . . . , 2020.

[91] Mark V Zagarola and Alexander J Smits. Mean-flow scaling of turbulent pipe flow. *Journal of Fluid Mechanics*, 373:33–79, 1998.